Influence of Diabatic Effects and Tropopause Structure on Baroclinic Development

Kristine Flacké Haualand

UNIVERSITY OF BERGEN

Influence of Diabatic Effects and Tropopause Structure on Baroclinic Development

Kristine Flacké Haualand

Thesis for the degree of Philosophiae Doctor (PhD)
at the University of Bergen

Date of defense: 10.06.2021

Scientific environment

This work was carried out at the Geophysical Institute at the University of Bergen and the Bjerknes Centre for Climate Research in Norway. My PhD position was funded by the University of Bergen and was associated with the UNPACC (Unifying Perspectives on Atmosphere-Ocean Interactions during Cyclone Development) and NORPAN (Partnership between Norway and Japan for excellent Education and Research in Weather and Climate Dynamics) projects. I have been enrolled in the Norwegian Research School on Changing Climates in the coupled Earth System (CHESS).

Acknowledgements

Doing a PhD is a challenging yet rewarding experience. Luckily, I have not been walking alone. With an inspiring attitude and a lot of patience, my supervisor, Thomas Spengler, has been available for questions, feedback, guidance, and scientific discussions. I have appreciated the opportunities and challenges he gave me through conferences, research visits, networking, and teaching. I further want to thank my co-advisor Michael Reeder for valuable feedback, fruitful conversations, and expert advice from the other side of the world, but also during his research visits in Bergen and at conferences. In addition, I want to acknowledge my collaboration with Vicky Meulenberg, whom I co-advised during her internship in Bergen. Vicky's work inspired me to explore the topic for the third paper of my thesis.

In 2018, I was lucky to be part of the ISOBAR field campaign in Hailuoto in Finland led by Stephan Kral and Jochen Reuder. Although not directly relevant for my thesis, this campaign gave me valuable experience in field work, made me involved in publishing an additional paper as a co-author, and motivated me as a researcher.

An important contribution for my motivation during my PhD was the scientific and social environment at the Geophysical Institute, at the Bjerknes Centre for Climate Research, at the research school CHESS, and in the writing group SciSnack. A special thank goes to the dynmet group for regular discussions and company at conferences. I also acknowledge the opportunity to laugh and sweat around a volleyball or a football together with colleagues.

Last, but definitely not least, I want to thank family and friends for bringing so much joy and value to my life. The final tribute goes to my two favourite persons in life: my son, Aslak, for adding a new dimension to life, and my husband, Åsbjørn, for all your support, motivation, and faith in me and for reminding me of what really matters in the end.

<div align="right">

Kristine Flacké Haualand
Bergen, March 2021

</div>

Abstract

Midlatitude cyclones play an important role in midlatitude weather and global climate. While baroclinic instability is the dominant mechanism for their intensification, midlatitude cyclone development is also influenced significantly by diabatic processes and tropopause structure. Of special importance is the relatively well-established role of latent heating associated with cloud condensation, which has been shown to enhance the intensification and reduce the horizontal scale of midlatitude cyclones. Less clear, however, is the role of other diabatic processes, such as latent cooling associated with evaporation of rain and sublimation or melting of snow as well as surface sensible and latent heat fluxes transferring heat and moisture between the ocean and the overlying cyclone. On top of these diabatic effects, baroclinic development depends on the structure of wind shear and stratification around the tropopause, which is essential for the coupling of the surface cyclone with the upper levels. However, the sensitivity of the development to various modifications of tropopause structure relative to diabatic processes remains unclear.

In this thesis, consisting of three papers, we examine the contribution of these less studied diabatic processes as well as the influence of tropopause structure on baroclinic development in a numerical extension of the linear quasi-geostrophic Eady model including effects of latent heating, latent cooling, surface sensible heat fluxes, and vertical modifications of wind shear and stratification across the tropopause. The linear approach focuses on effects of first order importance and restricts the study to the incipient stage of cyclone development, which is typically nearly linear.

In the first paper, we include a layer of latent cooling below a mid-tropospheric layer of latent heating in the ascent region of the cyclone. We find that low-level cooling weakens the vertical circulation and hence latent heating. With the intensifying effect of latent heating being reduced, latent cooling weakens baroclinic growth.

In the second paper, we find that baroclinic growth in the presence of latent heating also decreases when including surface sensible heat fluxes that are downward in the warm sector and upward in the cold sector, which is in line with reduced local horizontal temperature gradients and hence less low-level baroclinicity. Our findings remain similar when parametrising the surface sensible heat fluxes with respect to meridional temperature advection or vertical motion instead of temperature. In contrast, our findings are sensitive to the horizontal shift of surface sensible heat fluxes. Furthermore, estimates of increased latent heating related to moisture supply from surface latent heat fluxes indicate that the role of latent heat fluxes overcompensates for the detrimental effects from sensible heat fluxes, leaving the net effect of surface heat fluxes beneficial for cyclone intensification.

In the third paper, cyclone intensification is investigated further by modifying the

wind shear and stratification around the tropopause in experiments with and without mid-tropospheric latent heating. We find that baroclinic growth is not very sensitive to the sharpness and the altitude of the tropopause, but rather sensitive to modifications of the low-stratospheric wind shear and stratification. However, for reasonable modifications of wind shear, stratification, and latent heating intensity, we show that baroclinic growth is more sensitive to mid-tropospheric latent heating than to tropopause structure.

List of publications

1. Haualand, K. F. & T. Spengler (2019) *How Does Latent Cooling Affect Baroclinic Development in an Idealized Framework?*, Journal of Atmospheric Sciences **76(9)**, 2701-2714.

2. Haualand, K. F. & T. Spengler (2020) *Direct and Indirect Effects of Surface Fluxes on Moist Baroclinic Development in an Idealized Framework*, Journal of Atmospheric Sciences **77(9)**, 3211-3225.

3. Haualand, K. F. & T. Spengler *Relative importance of tropopause structure and diabatic heating for baroclinic instability*, Weather Clim. Dynam. Discuss. [preprint], in review, 2021.

Contents

Chapter 1

Background

1.1 Relevance of midlatitude cyclones for weather and climate

Midlatitude weather is dominated by cyclones and anticyclones typically forming near the western boundary currents before moving eastward along the storm tracks (see review by *Chang et al.*, 2002, and references therein) and potentially hitting land (Figure 1.1). While anticyclones are associated with calm and dry weather, cyclones are often accompanied by precipitation and strong winds. As a consequence, intense cyclones, or storms, may greatly influence infrastructure through damage of constructions, flooding, landslides, and avalanches.
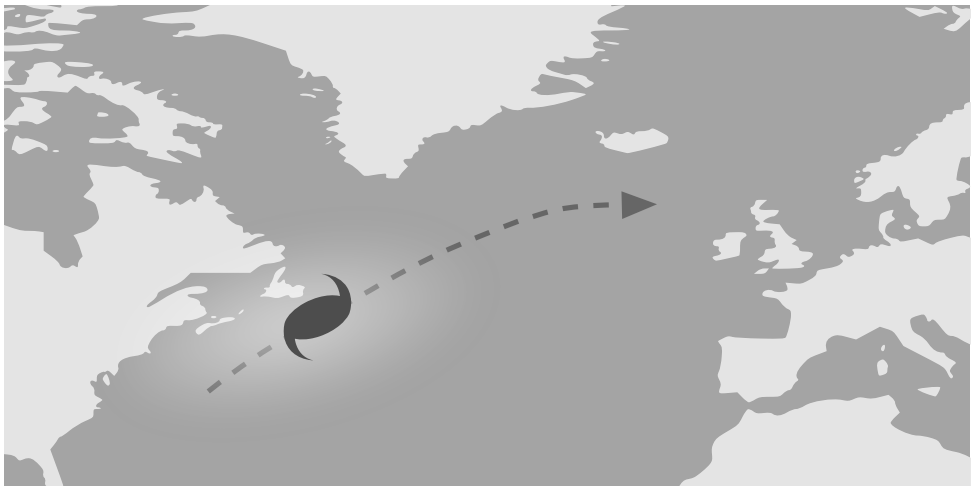
Figure 1.1: Illustration of midlatitude cyclone propagating northeastward along the North Atlantic storm track.

In addition to their high impact on the weather, cyclones and anticyclones are important components in the global climate system by transporting heat, energy, and momentum poleward (*Hartmann*, 1994). Moving warm air up and poleward and cold air down and equatorward, the heat transport by cyclones acts to weaken the merid-

ional temperature gradient that is constantly built up by the uneven radiative heating on Earth. The contribution to weaken the meridional temperature gradient ensures a somewhat balanced thermal state between tropical and polar regions, but is also an important source of energy for the cyclones because available potential energy from the atmosphere is converted to eddy available potential energy and later eddy kinetic energy (*Lorenz*, 1955). This process is called baroclinic energy conversion and intensifies midlatitude cyclones, which develop as growing baroclinic waves by consuming baroclinicity associated with the meridional temperature gradients.

1.2   Theoretical advances in midlatitude cyclone development

One of the first conceptual models of midlatitude cyclones, including its associated meridional heat transport, was the Norwegian cyclone model (*Bjerknes*, 1919; *Bjerknes and Solberg*, 1922), which describes how a cyclonic disturbance along the polar front propagates eastward while transporting warm air poleward to the east of the cyclone's centre and cold air equatorward to the west of the cyclone's centre, leading to the formation of a warm and cold front, respectively (Figure 1.2). Despite some weaknesses of this model, especially at later stages of development (*Schultz et al.*, 2019), which led to more advanced versions like the Shapiro-Keyser cyclone model (*Shapiro and Keyser*, 1990), the Norwegian cyclone model captures many of the key elements in the horizontal structure and evolution of midlatitude cyclones, such as the local temperature contrasts between the warm and the cold sector.
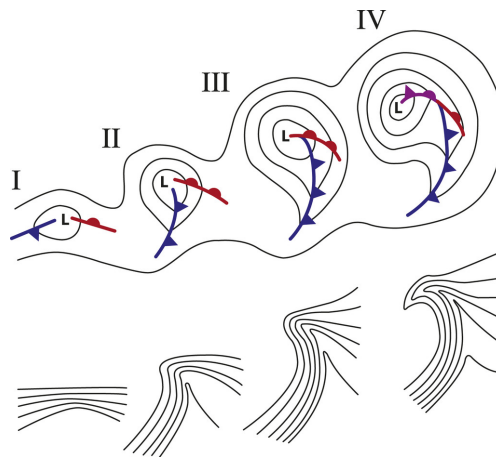
Figure 1.2: Conceptual Norwegian cyclone model showing (top) lower-tropospheric (e.g., 850 hPa) geopotential height and fronts, and (bottom) lower-tropospheric potential temperature. The stages in the cyclone's evolution are separated by approximately 6–24 h and the frontal symbols are conventional. The characteristic scale of the cyclone based on the distance from the geopotential height minimum, denoted by L, to the outermost geopotential height contour in stage IV is 1000 km. [Caption and figure from Fig. 2 in Schultz and Vaughan (2011). © American Meteorological Society. Used with permission.]

Further advancing the concept of midlatitude cyclone development, *Charney* (1947) and *Eady* (1949) described how midlatitude cyclones intensify through baroclinic energy conversion, where intensifying baroclinic waves were found to be energetically consistent with warm air rising poleward and cold air sinking equatorward (Figure 1.3). They found remarkable agreement between their estimated growth rates and length scales of the most unstable baroclinic wave and those of midlatitude cyclones at the early stage of development. Even the westward tilting pressure field with height that characterises baroclinic waves (Figure 1.3) shares similarities with the vertical structure of observed midlatitude cyclones.
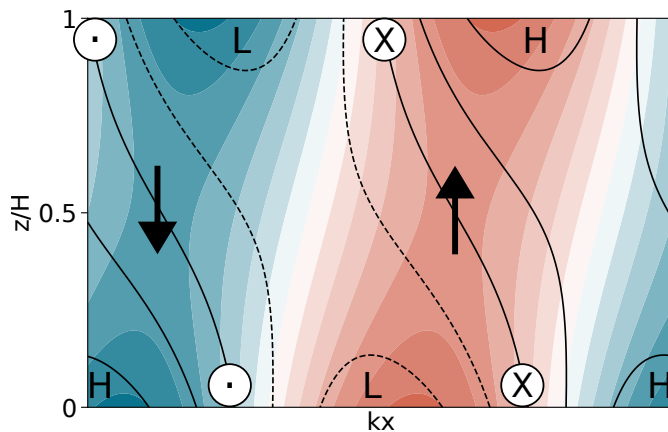

Figure 1.3: Structure of the quasi-geostrophic streamfunction (contours) and temperature (shading) of the most unstable Eady mode, shown for one wavelength and for height scaled with respect to tropopause altitude. Upward (downward) arrow indicates upward (downward) motion, cross (dot) symbols indicate meridional flow into (out of) the figure, red (blue) shading indicates anomalous warm (cold) air, and L (H) letters indicate correspondence to minimum (maximum) pressure anomalies.

A more thorough understanding of these baroclinic waves was later established through the concept of potential vorticity (PV) thinking (*Hoskins et al.*, 1985), where positive (negative) PV anomalies are associated with cyclonic (anticyclonic) circulation and are a powerful tool to diagnose the dynamics of atmospheric features like midlatitude cyclone development. When two PV anomalies of same sign tilt upshear with height in a baroclinic atmosphere with a reversal of the basic-state horizontal PV gradient at their respective locations, they mutually interact by advecting PV from the environment to the location of the other anomaly (Figure 1.4). This is of relevance for the baroclinic waves found by *Eady* (1949), because his vertical boundary conditions represent such a reversal in the basic-state meridional PV gradient as well as temperature edge waves (*Davies and Bishop*, 1994) that can be interpreted as PV anomalies (*Bretherton*, 1966; *de Vries et al.*, 2010). When these edge waves tilt upshear with height and interact such that they propagate with the same speed, they phase lock and travel together as one growing baroclinic wave.
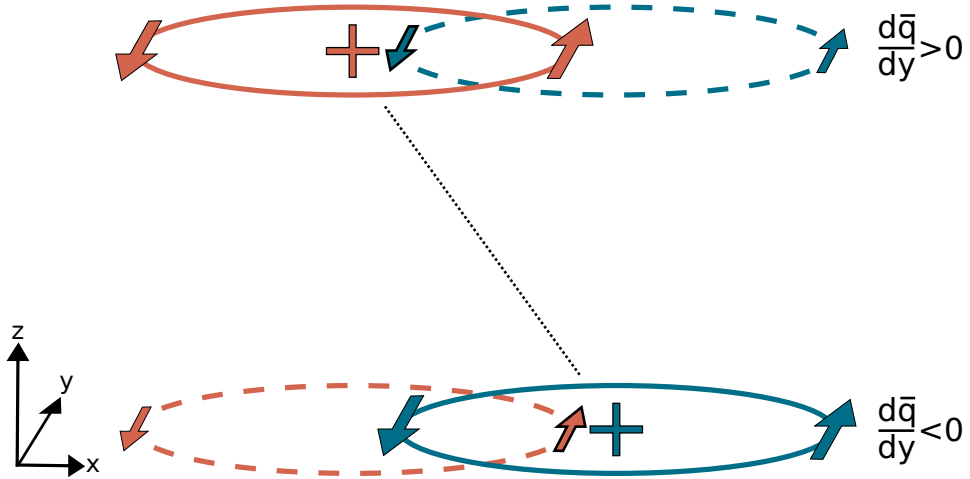
Figure 1.4: Schematic of how a low-level PV anomaly (blue plus symbol) mutually interacts with an upper-level PV anomaly (red plus symbol) by advecting high PV from the basic-state toward the location of the other PV anomaly, with the sign of the basic-state PV gradient reversing at the respective vertical levels. The induced circulation associated with each PV anomaly is indicated by arrows around circles with the same respective colours as the PV anomalies, with the vertically induced circulation at the level of the other PV anomaly being indicated by dashed lines and small arrows, and the wind relevant for mutual intensification being highlighted by bold stroke. The westward tilt with height between the PV anomalies necessary for intensification is denoted by the black dotted line.

1.3   Role of diabatic processes in midlatitude cyclone development

Of further relevance for cyclone development are diabatic processes because they generate diabatic PV anomalies and modify the energetics by generating eddy available potential energy (*Lin and Smith*, 1979; *Smith*, 1980; *Vincent et al.*, 1977) and in some cases enhancing the conversion to eddy kinetic energy by strengthening the secondary circulation (*Robertson and Smith*, 1983). Misrepresentations of these processes may therefore result in large forecast errors of midlatitude cyclones (e.g., *Beare et al.*, 2003; *Martínez-Alvarado et al.*, 2016).

The most important diabatic process for midlatitude cyclone development is latent heating, which occurs, for example when water condenses and clouds form. The effect of latent heating on cyclone development is relatively well known and has been shown to increase cyclone growth and decrease the horizontal scale of cyclones (e.g., *Balasubramanian and Yau*, 1996; *Craig and Cho*, 1988; *Emanuel et al.*, 1987; *Manabe*, 1956; *Moore and Montgomery*, 2004; *Snyder and Lindzen*, 1991). Its impact on cyclone growth and structure is related to the diabatic generation of positive (negative) PV anomalies at lower (upper) levels (*Ahmadi-Givi et al.*, 2004; *Davis and Emanuel*, 1991; *Davis et al.*, 1993; *de Vries et al.*, 2010; *Stoelinga*, 1996), with the PV tendency being proportional to the vertical gradient of diabatic heating (Figure 1.5):

$$\frac{\partial}{\partial t}(\text{PV}) \sim \frac{\partial Q}{\partial z}. \tag{1.1}$$
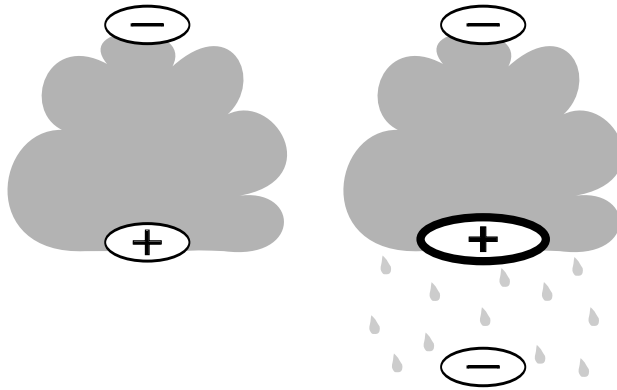

Figure 1.5: Schematic of positive (plus symbols) and negative (minus symbols) PV anomalies induced by latent heating exemplified by cloud condensation and latent cooling exemplified by evaporation of rain.

While the effect of latent heating is typically crucial for cyclone development, less is known about the effect of latent cooling associated with, e.g., evaporation of rain or sublimation of snow. As expected from the relation between the PV tendency and the vertical gradient of diabatic heating (Equation 1.1), latent cooling is associated with a positive (negative) PV anomaly above (below) the cooling layer (Figure 1.5) (*Crezee et al.*, 2017; *Joos and Wernli*, 2012). Thus, if a layer of evaporative cooling exists below a layer of condensational heating, leading to enhanced vertical gradients of diabatic heating at the interface between these layers, the low-level positive PV anomaly associated with latent heating is enhanced by the effects of latent cooling, which is anticipated to have implications for cyclone development.

As midlatitude cyclones typically form and grow over open ocean, surface sensible and latent heat fluxes are also often important for their development (e.g., *Bui and Spengler*, 2021). While sensible heat fluxes transfer heat, latent heat fluxes transfer moisture that can later condense and release latent heating. When cyclones move over the ocean, surface sensible heat fluxes from the ocean typically heat the cold air in the cyclone more than the warm air. As a response to this, the temperature contrast between the warm and the cold sectors weakens, such that there is less local baroclinicity at lower levels within the cyclone (*Branscome et al.*, 1989; *Zhang and Stone*, 2011).

Concurrently, surface latent heat fluxes transfer moisture from the ocean to the cyclone, leading to enhanced condensation and latent heating and thereby enhanced cyclone growth (*Pfahl et al.*, 2014). While most of the condensation occurs in the warm and moist sector of the cyclone, i.e., in the warm conveyor belt (*Browning*, 1990), surface latent heat fluxes are usually strongest in the cold and dry sector (e.g., *Carrera et al.*, 1999; *Zhang et al.*, 1999). Therefore, the greatest source of moisture for condensation is not necessarily within the cyclone consuming it, but may be related to peripheral origins like the leftovers of moisture from surface latent heat fluxes in the cold sector of preceding cyclones (Figure 1.6) (*Boutle et al.*, 2010; *Dacre et al.*, 2019).
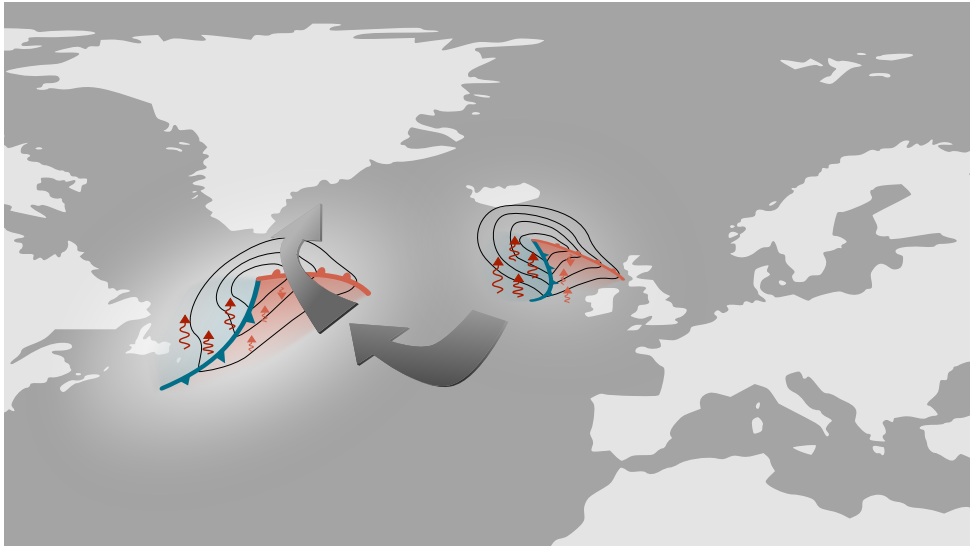
Figure 1.6: Schematic of how moist air from the cold sector of a preceding cyclone flows cyclone-relatively into the warm conveyor belt of a subsequent cyclone. Big grey arrows represent cyclone-relative flow between the cyclones and within the warm conveyor belt of the westernmost cyclone. Blue/red lines (shading) indicate cold/warm fronts (sectors), respectively. Wiggly arrows represent surface heat fluxes, with dark colour indicating strong intensity.

1.4   Role of tropopause and low-stratospheric structure in midlatitude cyclone development

Of further importance for midlatitude cyclone development is the tropopause, because it is associated with strong horizontal PV gradients that are important for the inter-action between upper-level waves and surface waves as demonstrated by baroclinic development in the Eady model. Such meridional PV gradients are directly related to tropopause structures through their proportionality to the vertical derivative of wind shear over stratification, which both change abruptly across the tropopause (*Birner et al.*, 2006; *Schäfler et al.*, 2020), making it difficult to accurately represent them in weather and climate models. In addition to the abrupt vertical changes around the tropopause, structures of wind shear and stratification near the tropopause may change in time, for example during downward fluctuations of the tropopause (*Hakim*, 2005) or during a weakening of the polar vortex that extends down toward the lower stratosphere after a sudden stratospheric warming event (*Baldwin and Dunkerton*, 2001). Thus, with the complex structures and features in the narrow region around the tropopause, where the observational network is sparse, it remains challenging to represent tropopause structure. This has resulted in relatively large forecast errors of PV gradients and Rossby waves and therefore probably also forecast challenges of midlatitude cyclones (*Gray et al.*, 2014; *Schäfler et al.*, 2018).

Chapter 2

Motivation

The relevance of midlatitude cyclones for midlatitude weather and global climate described in Chapter 1 demands a thorough understanding of their development in the current climate as well as in a future climate. The aim of this thesis is to improve the knowledge of how the effect of latent cooling, surface sensible and latent heat fluxes, and the structure of wind shear and stratification near the tropopause and in the lower stratosphere influence cyclone development in the presence of latent heating. This includes the following research questions:

RQ-1: How does latent cooling influence baroclinic development?

Previous studies found that latent cooling associated with evaporation, melting, and sublimation of hydrometeors such as rain and snow affects mesoscale systems like fronts and sting jets (e.g., *Barth and Parsons*, 1996; *Clough and Franks*, 1991; *Huang and Emanuel*, 1991; *Martínez-Alvarado et al.*, 2010; *Parker and Thorpe*, 1995) and enhances the low-level PV anomaly below the layer of latent heating in midlatitude cyclones (*Crezee et al.*, 2017; *Joos and Wernli*, 2012). However, no studies have investigated the further implications for baroclinic development.

In paper I, we aim to fill this gap by investigating how latent cooling and its impact on the diabatically induced PV anomalies influence the energetics and the development of baroclinic waves.

RQ-2: How do surface sensible and latent heat fluxes in conjunction with latent heating influence baroclinic development?

Previous studies showed that the role of surface sensible and latent heat fluxes on cyclone development is convoluted and varies with environmental conditions associated with, e.g., preceding cyclones, changes in sea surface temperature, and intrusion of polar air masses from cold air outbreaks or moist air masses from the subtropics (e.g., *Gyakum and Danielson*, 2000; *Kuo and Reed*, 1988; *Kuo et al.*, 1991a; *Langland et al.*, 1995; *Mullen and Baumhefner*, 1988). Consequently, surface heat fluxes can both enhance and weaken cyclone intensification (*Nuss and Anthes*, 1987). An important contribution from surface latent heat fluxes is related to the supply of moisture into the warm conveyor belt of the cyclone, leading to enhanced latent heat release (*Carrera et al.*, 1999; *Hirata et al.*, 2019; *Nuss and Anthes*, 1987; *Uccellini et al.*, 1987). Hence,

as latent heating is one of the most important diabatic contributions to cyclone intensification (e.g., *Balasubramanian and Yau*, 1996; *Craig and Cho*, 1988; *Kuo et al.*, 1991b), its effect should be included when investigating the role of surface sensible and latent heat fluxes on cyclone development. This was partly done by *Jiang and Gutowski* (2000), although their focus was on the effect of convective heating in the cold sector in the presence of surface sensible and latent heat fluxes. With latent heating being most dominant in the warm conveyor belt of the cyclone (*Browning*, 1990), idealised studies should rather implement latent heating in the warm and ascending part of the cyclone when studying the impact of surface heat fluxes on baroclinic development.

In paper II, we explore the role of surface sensible heat fluxes on baroclinic development in conjunction with latent heating associated with ascending air, with a focus on understanding how the formulation of the heat fluxes as well as the location relative to the warm sector and the region of latent heating matter for the development. The role of surface sensible heat fluxes on baroclinic growth is then compared to estimates of the changes in baroclinic growth resulting from an increase in latent heating related to typical moisture sources from remote surface latent heat fluxes.

RQ-3: How sensitive is baroclinic development to tropopause structure? How important is this sensitivity relative to that of latent heating?

Previous studies showed that the tropopause is characterised by abrupt transitions in wind shear and stratification (e.g., *Birner et al.*, 2006; *Schäfler et al.*, 2020) that are poorly represented in weather and climate models (*Hakim*, 2005; *Hamill et al.*, 2003) and lead to forecast errors of horizontal PV gradients around the tropopause (e.g., *Dirren et al.*, 2003; *Gray et al.*, 2014; *Hakim*, 2005; *Saffin et al.*, 2017). With the high relevance of these PV gradients for baroclinic waves, there is a common notion that baroclinic development is sensitive to the representation of wind shear and stratification around the tropopause. However, few studies have investigated the effect of tropopause sharpness on baroclinic instability, and no studies have quantified its impact by comparing it to other important effects on baroclinic development, such as the crucial role of latent heating.

In paper III, we systematically investigate the role of tropopause structure on baroclinic development by modifying the wind shear and stratification across the tropopause for various degrees of smoothing. Unlike previous studies, we contrast these effects to those related to alterations in tropopause height as well as to modifications in wind shear and stratification in the lower stratosphere that change the vertical integral of the horizontal PV gradients across the tropopause. Lastly, the sensitivity of baroclinic development to these tropopause structures is contrasted with the sensitivity to latent heating intensity.

Chapter 3

Methods

3.1 Classical Eady model

The cornerstone for the analysis in this thesis is an extended version of the *Eady* (1949) model, which is a simple yet powerful model describing baroclinic instability. The Eady model is formulated by the linear quasi-geostrophic (QG) PV equation in the zonal and vertical directions

$$\left(\frac{\partial}{\partial t} + \bar{u} \frac{\partial}{\partial x} \right) q' = 0 \,, \tag{3.1}$$

where q' is the QG potential vorticity perturbation and other variables having their usual meanings. It assumes adiabatic frictionless flow with constant basic-state density, Coriolis parameter, stratification, and vertical wind shear. Despite the absence of a y-coordinate, the vertical wind shear is associated with meridional temperature gradients through the thermal wind relation, which represents baroclinicity and is the source of energy for the wave to become unstable.

The boundary conditions in the Eady model prescribe vanishing vertical motion and introduce temperature anomalies at the top and the bottom of the domain that can be interpreted as edge waves (*Davies and Bishop*, 1994). If these edge waves are long and not too far apart, they "phase lock" and travel together with the same propagation speed. While travelling together, these waves mutually interact, in accordance with the concept of interacting PV anomalies. If the upper wave is upshear from the lower one, they intensify each other such that there is one wave structure in the entire domain that intensifies over time. In line with baroclinic energy conversion, the structure of the wave aligns such that warm air rises poleward and cold air sinks equatorward, which converts environmental available potential energy (APE) to eddy APE and eddy kinetic energy.

To find the structure and the growth rate of such unstable waves, the Eady problem was originally solved analytically by solving an eigenvalue problem yielding the growth rate as the eigenvalue and the vertical structure of the QG streamfunction ψ as the eigenvector. The problem is therefore a so-called normal mode problem, where one can find the most unstable solution and use the corresponding growth rate and streamfunction structure to investigate the most unstable mode. The structure of the wave then grows exponentially with time, with its growth determined by the growth rate. Such

modal solutions have been found to represent the main features of cyclone development in the atmosphere at the incipient stage rather well.

3.2   Eady model with diabatic effects

While the original Eady problem considered the PV equation with ψ as the model variable, the problem can be extended to include also the ω equation, with vertical motion ω as another model variable. This is useful because it opens up the possibility to include diabatic heating parametrised with respect to vertical motion. Following *Mak* (1994), we include latent heating Q_1 *divided by pressure* (which is the "heating" that appears in the diabatic forcing term of the PV equation) as

$$\frac{Q_1}{p} = -\varepsilon_1 \frac{1}{2} h_1 \omega^*, \tag{3.2}$$

where ε_1 is a constant heating intensity parameter, h_1 is the vertical heating profile, and ω^* is vertical motion at a predefined level taken here to be at the bottom of the heating layer. With this parametrisation, diabatic heating is represented as a wave with heating in a layer with mainly upward motion and cooling in a layer with mainly downward motion. Although the cooling counterpart in such an unconditional heating parametrisation is not necessarily as realistic as the heating layer, numerical experiments have shown that it does not alter the qualitative findings at weak to moderate heating intensities in the early stage of development (personal communication with H. de Vries, 2019). It is unfortunately not possible to make the heating conditional on upward motion in this linear model.

The default heating profile h_1 is a step function (left panel in Figure 3.1) and equals one in the heating layer between 900 hPa and 400 hPa and zero elsewhere. Latent cooling is included below the latent heating layer by extending the heating profile to negative values below 900 hPa (left panel in Figure 3.1). The sensitivity to the simple step function form of the heating profile can be tested using smooth versions that are differentiable everywhere and mimic heating profiles from observations.

Following *Mak* (1998), we further include surface sensible heat fluxes Q_2 divided by pressure as

$$\frac{Q_2}{p} = \varepsilon_2 h_2 \frac{\partial \psi}{\partial p}, \tag{3.3}$$

where ε_2 is a constant heating intensity parameter, h_2 is the vertical heating profile for surface fluxes (middle panel in Figure 3.1), which is set to one below 900 hPa and zero elsewhere, and $\partial \psi / \partial p$ is referred to as negative temperature. The latter nomenclature is consistent with previous literature and represents the anomalous temperature difference between the air above the surface and the sea surface temperature, with the latter set to a constant value. Such a parametrisation represents upward sensible heat fluxes in the cold sector and downward sensible heat fluxes in the warm sector of the baroclinic wave. Motivated by the finding that surface fluxes also strongly depend on the meridional temperature advection (*Boutle et al.*, 2010), we also add a modified version of this parametrisation by substituting $\partial \psi / \partial p$ by $-v = -\partial \psi / \partial x$, such that surface

sensible heat fluxes are positive when the wind is equatorward and negative when the wind is poleward.

In addition to the two foregoing parametrisations of surface fluxes, we test a third parametrisation of surface fluxes similar to that of latent heating, where $\partial \psi / \partial p$ is substituted by ω^*, such that downward surface fluxes are always located below the latent heating layer. This parametrisation is not necessarily based on physical arguments, but has the advantage that surface fluxes can be directly phase shifted relative to latent heating, independent of modifications of the low-level wave structure. Also, the location of surface sensible heat fluxes does not change much from the previous parametrisations, as low-level ascent is located near warm air advection. The location of surface sensible heat fluxes can be further shifted by letting the heating intensity parameter become complex, where a purely imaginary heating intensity corresponds to a quarter of a wavelength phase shift compared to a real heating intensity.

As surface latent heat fluxes are dependent on specific humidity, which is absent in this idealised model, we will not attempt to represent these fluxes directly. Nevertheless, as latent heat fluxes provide important moisture supply available for condensation, we evaluate its impact on baroclinic development relative to that of surface sensible heat fluxes through the effect of increased latent heating by estimating the change in growth rate resulting from changes in latent heating intensity associated with typical moisture sources.
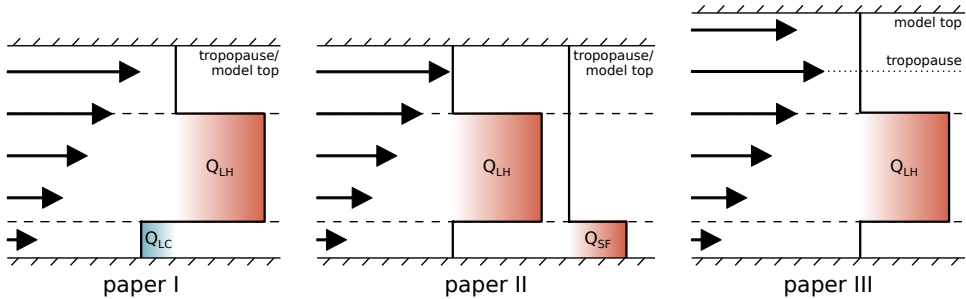

Figure 3.1: Overview of basic model setup for the three papers in this thesis illustrating the basic-state zonal wind (arrows) and the vertical profiles of diabatic heating (solid lines and red/blue shading for positive/negative values), where the subscripts LH, LC, and SF refer to latent heating, latent cooling, and surface fluxes, respectively. The heating/cooling boundaries, tropopause interface, and model boundaries are marked by dashed, dotted, and hatched horizontal lines, respectively. These interfaces represent the levels where PV anomalies can exist.

3.3 Eady model with tropopause

In addition to the diabatic effects, the Eady model can be extended to include an idealised tropopause where the wind shear and/or stratification change from a constant tropospheric value to another constant stratospheric value (illustrated by linearly increasing/decreasing zonal wind below/above the tropopause in the right panel in Figure 3.1). Such vertical changes in wind shear and/or stratification result in a nonzero PV gradient at the tropopause and hence PV anomalies at the tropopause that can inter-

act with other PV anomalies. To restrict the mutual interaction of PV anomalies to the troposphere, we remove temperature anomalies, which can be interpreted as PV anomalies, at the upper boundary by using an upper boundary condition of $\partial \psi / \partial p = 0$.

To further investigate the sensitivity of baroclinic development to the structure around the tropopause, we modify the vertical profiles of wind shear and/or stratification by smoothing their transitions around the tropopause, altering the altitude of the tropopause interface, and changing the value in the stratosphere. For the smoothing, we substitute the step function at the tropopause with a sine function in a vertical interval around the tropopause.

3.4   Numerical solution procedure

Many of the experiments in this thesis, such as those based on smooth vertical profiles of diabatic heating, wind shear, and/or stratification, would be hard to conduct in an analytical model. We therefore use a numerical extension, where the PV equation and the ω equation are formulated at N vertical levels and form a linear matrix problem

$$\mathbb{A}\boldsymbol{\xi} = \sigma \mathbb{B}\boldsymbol{\xi}, \tag{3.4}$$

with the growth rate σ being the eigenvalue, $\boldsymbol{\xi} = [\psi_1, \psi_2, \ldots, \psi_N, \omega_1, \omega_2, \ldots, \omega_N]$ being the eigenvector with the subscripts for ψ and ω referring to the vertical grid point, and $\mathbb{A}$ and $\mathbb{B}$ being matrices that represent all remaining constants. The problem can then be solved for a given wavenumber by standard matrix solution techniques.

An observant reader may notice that such a problem contains one degree of freedom related to one more model variable than number of equations. Thus, the problem can only be solved with an arbitrary scaling of variables, implying that we cannot quantitatively compare ψ and ω across different experiments and wavenumbers. We alleviate this issue by normalising solutions with respect to meaningful quantities such as energy and surface pressure and argue that it is then still meaningful to cautiously compare some of the solutions quantitatively.

3.5   Lorenz' energy cycle

The effects of diabatic processes and tropopause structure are investigated using the energy framework introduced by *Lorenz* (1955), where the tendency of domain-averaged eddy available potential energy (EAPE) is defined as

$$\frac{\partial}{\partial t}(\text{EAPE}) = C_a + C_e + G_e, \tag{3.5}$$

and $C_a = -\dfrac{\lambda}{S}\overline{\psi_x \psi_p}$ is the conversion of basic-state potential energy to eddy available potential energy, $C_e = \overline{\omega \psi_p}$ is the conversion from eddy available potential energy to eddy kinetic energy, and $G_e = -\dfrac{1}{S}\overline{Q\psi_p}$ is the diabatic generation of eddy available potential energy, with the bar denoting zonal and vertical averages. When including more than one diabatic effect, G_e can be split into the respective parts using the different contributions to diabatic forcing Q.

Chapter 4

Summary of the papers

Paper I: How Does Latent Cooling Affect Baroclinic Development in an Idealized Framework?

In line with previous studies and an increased vertical gradient of heating, we find in this paper that including latent cooling below a layer of latent heating increases the PV anomaly at the bottom of the latent heating layer. Concurrently, the PV anomaly at the top of the heating layer weakens in the presence of low-level latent cooling, which is related to reduced latent heating and hence a weaker vertical heating gradient at the top of the latent heating layer. We find that the reduced latent heating is associated with weaker vertical circulation due to low-level cooling. Hence, while low-level latent cooling enhances the PV anomaly between the latent heating and the latent cooling layers, it also weakens cyclone ascent and thereby latent heating. As latent heating intensifies baroclinic development, the reduction of latent heating associated with latent cooling leads to weaker baroclinic growth.

Paper II: Direct and Indirect Effects of Surface Fluxes on Moist Baroclinic Development in an Idealized Framework

As expected from the reduction of low-level baroclinicity when the cold sector of a baroclinic wave is heated and the warm sector is cooled, this paper shows that surface sensible heat fluxes in the presence of latent heating reduce baroclinic growth. The argument relating baroclinic growth to low-level baroclinicity is further supported by the finding that baroclinic growth enhances when the location of the surface sensible heat fluxes reverses relative to the warm and cold sectors. Such shifts in the location of surface fluxes relative to the warm and cold sectors may be motivated by cyclones moving over regions with strong sea surface temperature contrasts, such as over the Gulf Stream and the Kuroshio. Moreover, if surface sensible heat fluxes are shifted only halfway upstream or downstream toward the opposite sector, the growth rate remains more or less unaltered compared to when no surface fluxes are added. Despite this negligible impact on the growth rate, an upstream or downstream shift of the surface sensible heat fluxes results in relatively large differences in the energetics and the low-level structure of the wave, which may be of importance for nonlinear processes that are not investigated in this linear framework. While these findings indicate that baroclinic development is rather sensitive to the location of surface sensible heat fluxes, we find that the results are not very sensitive to the surface flux parametrisation.

Independent of the location, the impact from surface sensible heat fluxes on baroclinic growth is weak relative to the positive impact by latent heating alone. Furthermore, estimates of the increase in latent heating associated with typical input of moisture from remote surface latent heat fluxes indicate that the effect of surface latent heat fluxes can easily overcompensate for the detrimental effects by surface sensible heat fluxes. Hence, for typical environmental conditions, the net effect of surface sensible and latent heat fluxes is usually intensifying baroclinic growth.

Paper III: Relative importance of tropopause structure and diabatic heating for baroclinic instability

This paper shows that baroclinic instability related to interactions between an idealised tropopause and a surface is most unstable when there are weak or no changes in wind shear and large changes in stratification across the tropopause. This is arguably due to enhanced energy conversion from basic-state available potential energy to eddy available potential energy associated with an improved phase relation between temperature and meridional wind in the tropopause region. Smoothing these vertical profiles of wind shear and stratification around the tropopause results in a further enhancement of energy conversion and hence even stronger baroclinic growth. However, for more realistic configurations, with a reversal of wind shear across the tropopause resulting in a tropopause jet, the effect of smoothing on baroclinic growth is negligible. Similarly, modifying the altitude of the tropopause has weak impacts on the growth rate. Instead, this study finds that baroclinic instability is more sensitive to changes in wind shear and stratification in the lower stratosphere that modify the vertical integral of PV across the tropopause region. Nevertheless, including latent heating and varying its heating intensity has a much more pronounced effect on the growth rate than any of the effects related to the representation of wind shear and stratification at and above the tropopause. Hence, baroclinic development is more sensitive to diabatic heating than tropopause structure.

Chapter 5

Conclusions and Outlook

The main research questions for this thesis concern how low-level latent cooling, surface sensible and latent heat fluxes, and tropopause structure affect baroclinic development in the presence of mid-tropospheric latent heating. In this thesis, we have shown that all these processes influence midlatitude cyclone development in various ways by changing the growth rate, the propagation speed, the horizontal and vertical scale, and the intrinsic structure, including the energetics of the cyclone as well as the associated circulation. However, using the effect of latent heating on baroclinic development as a reference, this thesis demonstrates that midlatitude cyclone development is more sensitive to latent heating and to some extent remote surface latent heat fluxes and low-stratospheric structure than to latent cooling, surface sensible heat fluxes, and tropopause sharpness and altitude.

Many of the findings from this thesis may be of even higher relevance in a future climate, which is predicted to be associated with a warmer troposphere and sea surface as well as higher specific humidity (*Collins et al.*, 2013). Such environmental changes may imply fundamental adjustments in the governing diabatic processes related to midlatitude cyclones. For example, with more moisture available for condensation, the effect of latent heating on cyclone development is expected to increase (see review by *Catto et al.*, 2019, and references therein), contributing to stronger cyclone growth. This positive contribution from latent heating is opposed by a negative effect from weaker baroclinicity in the lower troposphere associated with stronger warming in the Arctic relative to lower latitudes, leaving the net change of cyclone intensity in a future climate uncertain (e.g., *Catto et al.*, 2011; *Geng and Sugi*, 2003).

The increase in humidity and cloud condensation is associated with increased precipitation in midlatitude regions exposed to high cyclone frequency (*Bengtsson et al.*, 2009; *Fläschner et al.*, 2016). With more precipitation, there is also a potential for more evaporation of rain and the related latent cooling, which was found in paper I to weaken cyclone intensification and may therefore – together with the effect of weaker baroclinicity – partly compensate for the enhancement related to the increase in condensation and latent heating. Hence, a potential intensification of midlatitude cyclones in a future climate may be less prominent if the effects related to latent cooling are accounted for, though we expect this effect is minor compared to those related to latent heating and baroclinicity.

The future warming of the sea surface and the overlying air modifies the surface sensible and latent heat fluxes in various ways. While upward surface sensible heat

fluxes are expected to dominate less in the future, a higher saturation humidity related to the warming of the upper ocean makes upward surface latent heat fluxes dominate more (*Bala et al.*, 2010; *Boer*, 1993; *Large and Yeager*, 2012). This suggests that the imbalance between the positive effect from surface latent heat fluxes and the negative effect from surface sensible heat fluxes on baroclinic growth discussed in paper II may increase in a future climate, such that the net influence of surface sensible and latent heat fluxes on midlatitude cyclones is an increase in cyclone growth.

Along with the warming of the troposphere, climate change is associated with a cooling of the stratosphere (*Held*, 1993). As a result, the meridional temperature gradient around the tropopause enhances, such that the upper-level zonal wind strengthens through the thermal wind relation (*Butler et al.*, 2010; *Räisänen*, 2003). With a strengthening of the zonal wind near the tropopause, the vertical difference in wind shear across the tropopause increases. This is of relevance for the findings from paper III, where we found that the relatively weak sensitivity of cyclone development to tropopause sharpness depends on the difference in zonal wind shear across the tropopause. Depending on the exact configuration of wind shear, such future projections on the upper-level wind field may either increase or decrease the importance of tropopause sharpness for baroclinic development. Nevertheless, as the amount of latent heating is predicted to increase in a future climate and therefore become more important for baroclinic instability, the large imbalance between the weak importance of tropopause sharpness and the high importance of latent heating for baroclinic instability found in paper III will probably increase in a future climate.

The findings in this thesis are investigated in a linear quasi-geostrophic two-dimensional model that is numerically extended from the classical Eady model including diabatic effects and/or a tropopause. Such an idealised approach facilitates the interpretation of the mechanisms in focus. Further mechanisms relevant for midlatitude cyclone development may be included in the future, such as the effect of friction, which modifies the low-level circulation and hence the location of latent heating and surface sensible and latent heat fluxes. Another relevant process is the beta effect, which takes into account variations in the Coriolis parameter and alters the gradient of potential vorticity. Furthermore, a natural extension to the study on tropopause structure in paper III would be to modify the basic-state zonal wind profile to account for a stratospheric jet representing the polar vortex as well as downward extensions of a weakening polar vortex resulting from sudden stratospheric warming events, which have been shown to influence baroclinic development (*Rupp and Birner*, 2021). However, it is important to keep in mind that adding new layers of complexity in such a basic linear model may result in misleading interpretations of the findings, as nonlinear processes that are not represented typically become more important when the complexity increases. Thus, it may be most appropriate to investigate only a few mechanisms at the same time.

While the idealised approach in this thesis is an advantage for the physical interpretation of the results, it suffers from its deficiency of representing several concurrent relevant processes and their nonlinear interactions. Nevertheless, with this thesis' improved basic understanding of how diabatic effects and tropopause structure influence midlatitude cyclone development, our findings point to what more advanced modelling and observational studies could focus on in the future.

One natural step would be to further clarify our findings in three-dimensional numerical weather prediction models including moisture and accounting for nonlinear

processes. Such models could for example investigate if cyclone growth is stronger when latent cooling is omitted from the simulations, as indicated by paper I, or whether the qualitative impact from surface fluxes on cyclone development found in paper II changes when including moisture sources from remote surface fluxes in preceding cyclones, as was partly done by *Bui and Spengler* (2021). Another aspect worth investigating further in more advanced models is the sensitivity of cyclone development to initial conditions of basic-state wind and temperature near the tropopause. Motivated by the importance of preserving the vertical integral of the PV gradient across the tropopause from paper III, one could for example evaluate how modifications near the tropopause influence the vertical integral of PV gradients and thereby cyclone development. Another idea for future research is to test how sensitive the effect of diabatic processes and tropopause structure on cyclone development is to increased background temperature and humidity associated with a future climate.

Our findings could also be further tested in case studies and composite analyses of midlatitude cyclones. For example, inspired by the negative impact from latent cooling on cyclone growth demonstrated in paper I, it could be valuable to evaluate if there is more evaporation of rain and sublimation of snow relative to cloud condensation in weakly intensifying cyclones compared to strongly intensifying cyclones. Furthermore, clarifying the indication from paper II that cyclone development is possibly more sensitive to the location of surface sensible heat fluxes than to the exact parametrisation, observational studies could investigate if there is a relation between cyclone intensification and the location of surface sensible heat fluxes relative to the warm conveyor belt. Moreover, examining the role of surface latent heat fluxes discussed in paper II and previous literature, such studies could investigate if strongly intensifying cyclones and strong warm conveyor belts are associated with increased peripheral moisture sources from for example preceding cyclones, cold air outbreaks, or moist air masses from the subtropics. A final idea for future research is to explore if cases with large changes in vertical wind shear across the tropopause, and hence strong upper-level horizontal PV gradients, are characterised by reduced cyclone intensification compared to cases with smaller changes in vertical wind shear, as shown in paper III.

Paper I

How Does Latent Cooling Affect Baroclinic Development in an Idealized Framework?

Haualand, K. F. and Spengler, T.

How Does Latent Cooling Affect Baroclinic Development in an Idealized Framework?

KRISTINE F. HAUALAND AND THOMAS SPENGLER

Geophysical Institute, University of Bergen, and Bjerknes Centre for Climate Research, Bergen, Norway

ABSTRACT

Latent cooling by evaporating or melting hydrometeors has recently been shown to contribute to the positive low-level potential vorticity (PV) anomaly below the layer of latent heating in midlatitude cyclones. While the low-level PV anomaly might be intensified by latent cooling, the influence on the overall baroclinic development remains unclear. Including both latent heating and cooling in the Eady model, this study finds that latent cooling reduces baroclinic growth. While the PV anomaly between the layers of latent cooling and heating increases for realistic heating intensities, the PV anomaly at the top of the heating layer decreases, as latent heating is weakened because of reduced vertical motion within the cyclone. Consequently, the relative contribution from diabatic heating to the generation of eddy available potential energy decreases when latent cooling is included. Thus, despite the recently emphasized role of evaporation for the low-level PV anomaly in developing cyclones, the overall effect of latent cooling is detrimental to baroclinic growth.

1. Introduction

Latent heating has been shown to increase the growth rate of midlatitude cyclones while their horizontal scale is reduced (e.g., Manabe 1956; Craig and Cho 1988; Snyder and Lindzen 1991; Moore and Montgomery 2004). Although latent heating is probably the most important diabatic effect on midlatitude cyclone development, Forbes and Clark (2003) and Dearden et al. (2016) reported significant latent cooling rates from sublimation, melting, and evaporation of hydrometeors in midlatitude cyclones. While many studies have investigated the effect of these cooling processes on mesoscale systems, such as fronts or sting jets (e.g., Huang and Emanuel 1991; Clough and Franks 1991; Parker and Thorpe 1995; Barth and Parsons 1996; Martínez-Alvarado et al. 2010), only a few have addressed the effect on synoptic-scale cyclones (e.g., Joos and Wernli 2012; Crezee et al. 2017). The latter studies found that latent cooling, in particular through evaporation of rain, contributes to the low-level potential vorticity (PV) anomaly within the cyclone. The influence of this PV modification on cyclone development, however, remains unclear and forms the basis of this study.

Baroclinic instability is characterized by PV anomalies lying stationary relative to each other on the upper and lower boundaries (Bretherton 1966; Hoskins et al. 1985). These PV anomalies can be described as two phase-locked counterpropagating Rossby waves (e.g., Hoskins et al. 1985; Heifetz et al. 2004). De Vries et al. (2010) extended this framework to include interactions with PV anomalies induced by latent heating and emphasized the importance of the PV anomaly at the top of the heating layer. While its importance was supported by Pomroy and Thorpe (2000), other studies stressed the significance of the diabatically induced low-level PV anomaly for cyclone intensification (e.g., Davis and Emanuel 1991; Stoelinga 1996; Ahmadi-Givi et al. 2004). As the low-level PV anomaly is enhanced through evaporation or melting below the heating layer, the role of latent cooling on the interacting PV anomalies and the overall baroclinic development demands further assessment.

The influence of latent cooling on midlatitude cyclone development can also be explored by investigating

TABLE 1. Dimensional and nondimensional values of model parameters with corresponding units.

Parameter	S	λ	f	p_t	p_b
Dimensional value	$0.04 \, \mathrm{m^2 \, s^{-2} \, hPa^{-2}}$	$35 \, \mathrm{m \, s^{-1} \, hPa^{-1}}$	$10 \, \mathrm{s^{-1}}$	$150 \, \mathrm{hPa}$	$1000 \, \mathrm{hPa}$
Nondimensional value	4	3.5	1	0.15	1

the energetics. While no studies have looked at the direct influence from latent cooling on the diabatic generation of eddy available potential energy (EAPE), several studies have found that latent heating is the most important positive contributor to the EAPE in midlatitude cyclones (e.g., Vincent et al. 1977; Lin and Smith 1979; Smith 1980). Furthermore, diabatic heating not only generates EAPE; it also enhances the conversion to kinetic energy by strengthening the secondary circulation within the cyclone (Robertson and Smith 1983). The complexity of this direct and indirect impact on the energetics motivates a more detailed analysis of the role of latent heating and cooling.

We investigate the influence of latent cooling on the energetics, PV distribution, and baroclinic growth using a diabatic extension of the quasigeostrophic (QG) Eady (1949) model. The original extension was developed by Mak (1994) and included only latent heating. We add latent cooling at lower levels, which can be interpreted as evaporation of rain, snowmelt, and sublimation. Similar to Mak (1994), we use a highly idealized vertical distribution of latent heating and cooling, though we also test the validity of our results by prescribing more realistic profiles and by changing the basic-state static stability to mimic the effect of mixing in the heating and cooling layers.

2. Model

a. Model equations

We focus on the incipient stage of baroclinic development and use the same QG linear model and two-dimensional (x, p) coordinate system as Mak (1994), where x and p define the horizontal and pressure coordinates, respectively, but we allow the diabatic effects to include both latent heating and cooling. Thus, the diabatic processes can represent condensation and evaporation of rain as well as other phase transitions such as freezing, deposition, snowmelt, and sublimation. We start with the nondimensionalized QG ω and PV equations

$$\frac{\partial^2 \omega}{\partial p^2} + S\frac{\partial^2 \omega}{\partial x^2} = -2\lambda \frac{\partial^3 \psi}{\partial x^3} - \frac{\partial^2}{\partial x^2}\left(\frac{Q}{p}\right) \qquad (1)$$

and

$$\left(\frac{\partial}{\partial t} + \overline{u}\frac{\partial}{\partial x}\right)q + \frac{\partial \psi}{\partial x}\frac{\partial}{\partial p}\left(\frac{\lambda}{S}\right) = -\frac{\partial}{\partial p}\left(\frac{Q}{Sp}\right), \qquad (2)$$

where

$$q = \frac{\partial^2 \psi}{\partial x^2} + \frac{\partial}{\partial p}\left(\frac{1}{S}\frac{\partial \psi}{\partial p}\right)$$

is the QG PV, ψ is the QG streamfunction, ω is the vertical motion in pressure coordinates, λ is the vertical wind shear, $\overline{u}$ is the basic-state zonal wind, Q is the diabatic heating rate, and S is the basic-state static stability. The dimensional form of S is defined as

$$S = -\frac{R}{p}\left(\frac{\partial T_0}{\partial p} - \frac{RT_0}{c_p p}\right),$$

where R is the gas constant, c_p is specific heat at constant pressure, and T_0 is the background temperature. For consistency, we choose the same parameter values as Mak (1994) (see Table 1), where the velocity and length scales are $U = 10 \, \mathrm{m \, s^{-1}}$ and $L = 10^6 \, \mathrm{m}$, respectively. For constant λ, $\overline{u}(p) = \lambda(p_b - p)$ increases linearly with height (Fig. 1).

Assuming $\omega = 0$ at the top ($p = p_t$) and bottom ($p = p_b$) of the model boundaries yields the vertical boundary condition for the thermodynamic equation:

$$\left(\frac{\partial}{\partial t} + \overline{u}\frac{\partial}{\partial x}\right)\frac{\partial \psi}{\partial p} + \lambda\frac{\partial \psi}{\partial x} = -\frac{Q}{p}, \quad \text{at} \quad p = p_t, p_b, \qquad (3)$$

where $-\partial\psi/\partial p$ is proportional to the negative density perturbation, but, consistent with previous literature, will hereafter be referred to as temperature.

Following Mak (1994), we further assume that ψ and ω have wavelike solutions in the x direction:

$$[\psi, \omega] = \mathrm{Re}\{[\hat{\psi}, \hat{\omega}] \exp[i(kx - \sigma t)]\}, \qquad (4)$$

where k is the zonal wavenumber, σ is the wave frequency, and the hat denotes Fourier transformed variables.

b. Parameterization of latent heating and cooling

We parameterize the diabatic forcing in the same way as Mak (1994):

$$\hat{Q} = -\frac{\varepsilon \tilde{h}(p)}{2}\hat{\omega}_{\mathrm{hb}}(k), \qquad (5)$$
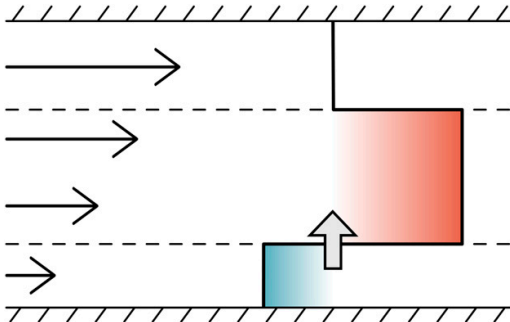
FIG. 1. Schematic of the heating and cooling layers, where red (blue) indicates heating (cooling). Black thin arrows illustrate the increase of wind with height. Gray thick arrow represents the vertical motion at the bottom of the heating layer, which is used in the heating parameterization. Dashed lines indicate boundaries where diabatic PV anomalies are induced.

where ε is the heating intensity parameter, $\tilde{h}$ is the vertical heating profile, and $\hat{\omega}_{hb}$ is the vertical motion at the bottom of the heating layer, as we assume heating is controlled by low-level convergence, similar to the idealized study by, for example, Craig and Cho (1988). The structure of the heating profile ensures a reasonable representation of the vertical distribution of diabatic heating in midlatitude cyclones and can be compared to case studies by, for example, Dearden et al. (2016).

The sign of $\tilde{h}$ and $\hat{\omega}_{hb}$ determines whether there is latent heating or cooling. A plausible physical reasoning for the diabatic cooling in the descent region is to assume a saturated atmosphere, where midlevel cooling represents longwave radiative cooling and evaporation of cloud droplets (e.g., De Vries et al. 2010). Furthermore, the low-level heating in the shallow layer below this cooling region could be associated with shallow convection in the cold sector.

For a conditional representation of heating, where condensational heating and evaporative cooling only occur in the ascent and not in the descent region, diabatic heating could be parameterized by an infinite spectral series. The unconditional heating in (5) would then represent the fundamental harmonic, while higher harmonics are neglected. H. de Vries (2019, personal communication) supports that such an unconditional representation of diabatic heating does not significantly alter the qualitative results at the incipient stage. We therefore argue that the heating parameterization in (5) is representative for the early development stage of extratropical cyclones.

Inserting (4) and (5) into (2) and (3) and letting $h = \tilde{h}/p$, hereafter referred to as the heating profile, yield

$$\frac{d^2\hat{\omega}}{dp^2} - Sk^2\hat{\omega} = i2\lambda k^3\hat{\psi} - \frac{\varepsilon k^2}{2}h\hat{\omega}_{hb} \qquad (6)$$

and

$$(\overline{u}k - \sigma)\left[\frac{d}{dp}\left(\frac{1}{S}\frac{d\hat{\psi}}{dp}\right) - k^2\hat{\psi}\right] + k\frac{d}{dp}\left(\frac{\lambda}{S}\right)\hat{\psi}$$
$$= -i\frac{\varepsilon}{2}\hat{\omega}_{hb}\frac{d}{dp}\left(\frac{h}{S}\right), \qquad (7)$$

with the corresponding boundary conditions $\hat{\omega} = 0$ and

$$(\overline{u}k - \sigma)\frac{d\hat{\psi}}{dp} + i\frac{\varepsilon h}{2}\hat{\omega}_{hb} + \lambda k\hat{\psi} = 0 \quad \text{at} \quad p = p_t, p_b. \qquad (8)$$

As (6) is linear, the vertical motion can be split into two components forced by each of the terms on the right-hand side. Mak (1994) argued that although interpreting these components as the dynamic and diabatic vertical motion can be meaningful for weak to moderate heating intensities, it is important to keep in mind that the components are coupled through the streamfunction and heating parameterization. Thus, they are neither purely dynamic nor diabatic. Nevertheless, we refer to them as the dynamic (ω_d) and diabatic components, where the diabatic component can be further split into one component due to latent heating ω_h and one due to latent cooling ω_c.

To incorporate latent cooling in the heating profile, we modify the step function used by Mak (1994) to be negative below the heating layer:

$$h(p) = H(p - p_{ht}) - (1 + \gamma)H(p - p_{hb})$$
$$= \begin{cases} 0 & \text{for} \quad p < p_{ht} \\ 1 & \text{for} \quad p_{ht} < p < p_{hb} , \\ -\gamma & \text{for} \quad p_{hb} < p \end{cases} \qquad (9)$$

where $p_{ht} = 0.4$ and $p_{hb} = 0.9$ are the pressures at the top and bottom of the heating layer, respectively, and γ is the fraction of latent cooling below p_{hb} with respect to the amount of latent heating above. For example, if $\gamma = 0.3$, the heating profile is 1 within the heating layer and -0.3 below, yielding latent heating (cooling) above (below) the bottom of the heating layer if $\omega_{hb} < 0$ (Fig. 1). Note from (7) that for constant λ and S, interior PV anomalies can only exist where $dh/dp \neq 0$. Thus, the step function in (9) yields interior PV anomalies at the heating boundaries p_{ht} and p_{hb} only (dashed horizontal lines in Fig. 1).

Note that $h(p)$ is the heating profile in the PV equation. The distribution of heating $\tilde{h}(p)$ in *physical space* is
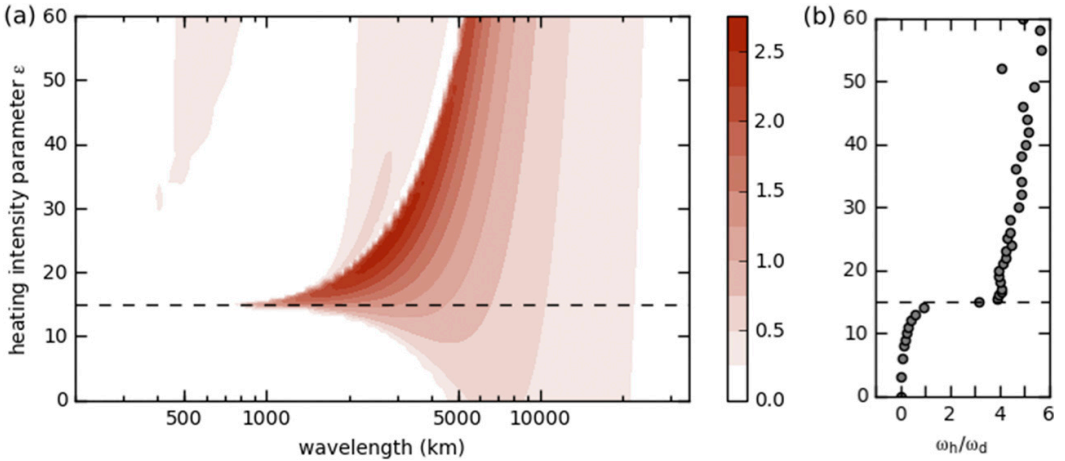
FIG. 2. (a) Growth rate $(10^{-5}\,\mathrm{s}^{-1})$ vs wavelength (km) for varying heating intensity parameter ε. (b) Amplitude of vertical motion due to latent heating ω_h divided by amplitude of dynamically induced vertical motion ω_d, both taken at the bottom of the heating layer. Dashed horizontal lines mark where $\varepsilon = 15$.

obtained by multiplying (9) by pressure, yielding a linearly decreasing profile with pressure within the heating layer.

c. Numerical solution

We use $n = (p_b - p_t)/\Delta p + 1 = 120$ vertical levels, where Δp is the vertical increment between two grid points. Vertical derivatives are expressed with standard finite-difference methods, using forward and backward differences at the model and heating boundaries and central differences elsewhere. Using the heating profile prescribed in (9) together with the boundary conditions $\omega = 0$ and (8), (6) and (7) form the eigenvalue problem

$$\mathbf{A}\boldsymbol{\xi} = \sigma\mathbf{B}\boldsymbol{\xi}, \qquad (10)$$

where $\mathbf{A}$ and $\mathbf{B}$ are matrices of dimension $2n \times 2n$, the wave frequency σ is the eigenvalue, and $\boldsymbol{\xi}$ is the eigenvector representing $\hat{\psi}(p)$ and $\hat{\omega}(p)$ through all vertical grid points from 1 to n:

$$\boldsymbol{\xi} = [\hat{\psi}_1, \hat{\psi}_2, \ldots, \hat{\psi}_n, \hat{\omega}_1, \hat{\omega}_2, \ldots, \hat{\omega}_n]. \qquad (11)$$

Applying standard solution techniques using the geev routine in the Linear Algebra Package (LAPACK; Anderson et al. 1999), which is based on the numerical QR algorithm, (10) can be solved for σ and $\boldsymbol{\xi}$. Hence, for a given wavenumber k, the full structure of ψ and ω can be derived from (4). At least 1 degree of freedom exists for all nontrivial solutions of (10), implying that the eigenvector $\boldsymbol{\xi}$ is not scaled and that we cannot quantitatively compare ψ and ω for different wavelengths and experiments. To alleviate this issue, we

tested several wavelength-dependent normalizations of $\hat{\psi}$ and $\hat{\omega}$ ranging from kinetic energy, available potential energy, total energy, minimum amplitude of the streamfunction, to the amplitude of the streamfunction at the surface. These normalizations allow for a more meaningful quantitative comparison of the solutions and yield important indications on how pertinent variables are influenced by diabatic effects. As we find similar behavior for all normalizations, we only present results normalized by total energy. Henceforth, all values except growth rate and wavelength are normalized with total energy, although not explicitly stated everywhere.

3. Choice of heating intensity and depth

a. Impact of heating intensity on growth rate and wavelength

Before including the effect of latent cooling, we examine the limitations of our linear model. Because of the normalization issues outlined in the previous subsection, we can neither directly infer the absolute heating rate from the heating intensity, nor assess the absolute magnitude of the model variables. Nevertheless, using realistic estimates of ψ and ω, we perform a scale analysis comparing the terms in the QG thermodynamic equation and contrast them with the term for ageostrophic advection of temperature, which is one order Rossby higher than the QG terms. When normalizing ψ and ω with a factor that yields surface meridional wind perturbations of $5\,\mathrm{m\,s}^{-1}$, we find that the magnitude of the ageostrophic

advection term is 25%–45% of the dominating QG terms when $0 \leq \varepsilon \leq 30$ (not shown). For comparison, using surface wind perturbations of $10 \, \mathrm{m \, s^{-1}}$, the corresponding ratio for the dry Eady limit ($\varepsilon = 0$) is 49%. We therefore argue that the inclusion of diabatic heating does not violate the QG approximation beyond what is regularly accepted in the dry Eady limit.

For $\varepsilon \leq 15$, an increase in ε yields an increase in the maximum growth rate and a decrease in the wavelength of the most unstable mode (Fig. 2a), consistent with several previous studies (e.g., Emanuel et al. 1987; Whitaker and Davis 1994; Moore and Montgomery 2004). As the wavelength of the instability is related to the vertical distance between the interacting PV anomalies (Hoskins et al. 1985), the decrease in wavelength for increasing ε is as expected because of the intensification of interior PV anomalies that acts to reduce the vertical distances between interacting PV anomalies. For $\varepsilon > 15$, the growth rate keeps increasing with increasing ε until $\varepsilon = 24$, although the wavelength is now also increasing. The latter indicates a regime shift, as it is in disagreement with the previously outlined arguments and findings. The implications of the regime shift are beyond the focus of this study.

b. Diabatically and dynamically induced vertical motion and estimated heating rates

The change in the qualitative behavior of the wavelength and the growth rate for $\varepsilon > 15$ is likely related to the dominance of the vertical motion due to latent heating ω_h compared to the dynamically induced ω_d (Fig. 2b). This diabatic dominance is not common in midlatitude cyclones as shown in a statistical analysis by Stepanyuk et al. (2017), in a model simulation of the intense *Queen Elizabeth II* storm by Pauley and Nieman (1992), and in an idealized baroclinic wave simulation by Rantanen et al. (2017). Thus, heating intensities $\varepsilon \leq 15$ seem to be most applicable to midlatitude cyclones.

Furthermore, using the scaling estimate by Mak (1994), a heating intensity parameter $\varepsilon = 30$ corresponds to a heating rate of $80 \, \mathrm{K \, day^{-1}}$. This is significantly larger than in the intense midlatitude cyclones studied by Pauley and Nieman (1992) and Dearden et al. (2016), where the maximum heating rates are below $20 \, \mathrm{K \, day^{-1}}$. Even though Joos and Wernli (2012) showed a locally confined maximum heating rate above $50 \, \mathrm{K \, day^{-1}}$ during the intensifying phase, the heating rate averaged over the heating layer was at least 2–3 times weaker. Moreover, Kuo et al. (1991) estimated heating rates up to $550 \, \mathrm{K \, day^{-1}}$ in the explosive *Queen Elizabeth II* storm, albeit at a highly nonlinear stage with the heating confined to a narrow band of about 250 km and a limited amount of time. Thus, there exist extreme cases where the average
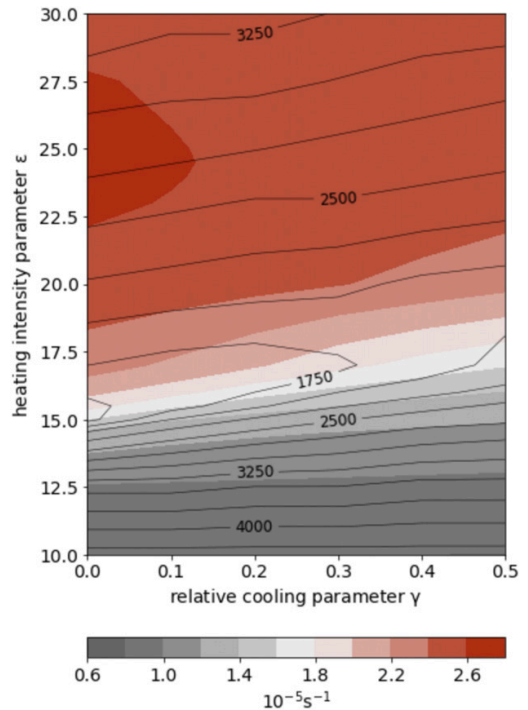

FIG. 3. Growth rate (shading, $10^{-5} \, \mathrm{s^{-1}}$) and wavelength (contours, km) of the most unstable mode for various heating intensity parameter ε and relative cooling parameter γ.

heating rate exceeds $100 \, \mathrm{K \, day^{-1}}$, though these values can be argued to be rare and not representative for a larger area of the developing cyclone. We therefore argue that heating intensities corresponding to $\varepsilon \lesssim 15$, that is, heating rates $\leq 40 \, \mathrm{K \, day^{-1}}$, are a realistic and representative choice.

c. Additional modes at strong heating intensities

For $\varepsilon > 15$, additional unstable modes at shorter wavelengths appear, which were studied in detail by Mak (1994) (Fig. 2a and his Figs. 6b,c). The first of these modes appears for $\varepsilon \gtrsim 20$ and is confined to the layer above the heating layer, whereas the second mode appears for $\varepsilon \gtrsim 35$ and is confined to the layer below the heating layer. While Mak (1994) indicated that the lower mode can be associated with mesoscale cyclones such as polar lows, we argue that the mode's shallow low-level westward tilt with height would be in the boundary layer where the atmosphere is commonly well mixed, as seen in the vertical cross sections of polar lows by Terpstra et al. (2015). Consequently, the suggested interaction between the PV anomalies at the surface and the
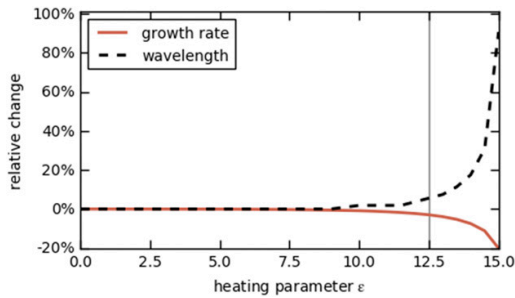
FIG. 4. Change in growth rate (red) and wavelength (dashed black) from $\gamma = 0.0$ to $\gamma = 0.5$ relative to the reference value at $\gamma = 0.0$ for the most unstable mode and various heating intensity parameters ε. The gray vertical line marks where $\varepsilon = 12.5$.

bottom of the heating layer is an unlikely feature of polar lows. Similarly, because of the unrealistically strong heating intensities necessary for these additional modes, we also question whether the upper mode identified by Mak (1994) can be associated with realistic atmospheric instabilities. Considering the limited validity of these additional modes, the aforementioned unrealistic dominance of ω_h, as well as the excessive estimated heating rates for large ε, we restrict our study to $\varepsilon \leq 15$.

d. Justification for chosen heating boundaries

Based on a subjective evaluation of vertical heating distributions in case studies of representative midlatitude cyclones (Pauley and Nieman 1992; Joos and Wernli 2012; Joos and Forbes 2016; Dearden et al. 2016), we find the bottom of the heating layer to be approximately between 950 and 800 hPa, and the top of the heating layer to be roughly between 500 and 300 hPa. Thus, our choice using the same heating boundaries as Mak (1994), where $p_{hb} = 900$ hPa and $p_{ht} = 400$ hPa, appears reasonable.

e. Impact from latent cooling

For increasing latent cooling, the wavelength of the most unstable mode increases at heating intensities $10 \leq \varepsilon \leq 15$, but decreases at intensities $18 \lesssim \varepsilon \leq 30$ (Fig. 3). In this range of heating intensities, the maximum growth rate decreases with increasing latent cooling. Comparing Fig. 3 with Fig. 2a, the effects of latent cooling are similar to the effect of decreasing ε. This relation between an increase in γ and a decrease in ε remains similar when examining the additional modes appearing at extreme heating intensities (not shown).

The changes in wavelength and growth rate for increasing latent cooling depicted in Fig. 3 increase exponentially for increasing ε (Fig. 4, shown only up to $\varepsilon = 15$).
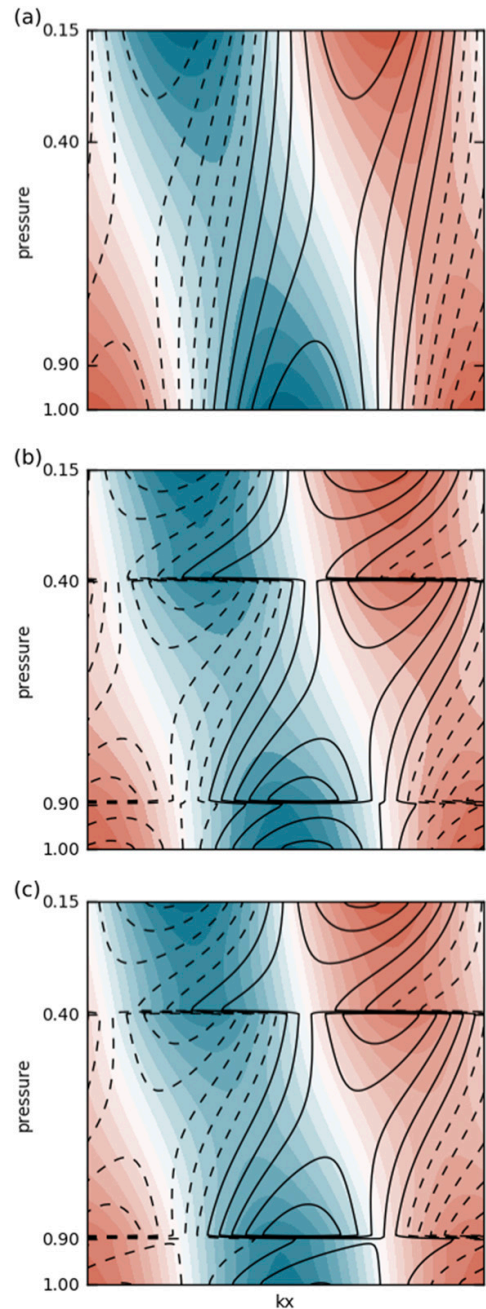

FIG. 5. Structure of streamfunction (shading) and $-\partial\psi/\partial p \propto$ temperature (contours) for the most unstable mode for (a) $\varepsilon = 0$ and $\gamma = 0.0$ (dry Eady mode), (b) $\varepsilon = 12.5$ and $\gamma = 0.0$, and (c) $\varepsilon = 12.5$ and $\gamma = 0.5$. Solid (dashed) contours and red (blue) shading represent positive (negative) values.

To investigate cases with a clear contribution from latent cooling, but at the same time staying clear of the threshold at $\varepsilon = 15$, we focus our analysis on $\varepsilon = 12.5$. At this heating intensity, the growth rate decreases by 3.0% and the wavelength increases by 5.3% when increasing γ from 0.0 to 0.5. The corresponding values if using $\varepsilon = 10$ are 0.9% and 1.3%, respectively.

4. Impact from latent heating and cooling on structure and amplitude

a. Streamfunction and temperature

Despite the noteworthy impact from latent heating and cooling on the growth rate, the structure of the streamfunction remains qualitatively similar to the dry Eady solution (Fig. 5a) when including latent heating (Fig. 5b) or when including both latent heating *and* cooling (Fig. 5c). It is particularly striking that there is barely any change in structure when adding latent cooling (Fig. 5c) to the results including latent heating (Fig. 5b). All solutions tilt westward with height, in accordance with baroclinic instability. The main difference is the presence of local extrema and weak kinks at the heating boundaries when adding latent heating and/or cooling. The meridional velocity $\partial\psi/\partial x$ is proportional to the streamfunction and phase shifted by 90° (not shown).

As expected from baroclinic instability theory, the structure of the temperature (contours in Fig. 5) tilts eastward throughout the whole model troposphere. When including latent heating and/or cooling, local temperature extrema are present within the heating layer and close to the heating boundaries. The sign of the temperature anomalies partly reverses across the heating boundaries, especially when $\varepsilon \to 15$ (not shown). This temperature reversal is consistent with the strengthening of the diabatic PV anomalies (not shown), where a positive (negative) PV anomaly is associated with warm (cold) air above and cold (warm) air below. Such a PV dipole is a common feature of the early development stage of midlatitude cyclones (e.g., Crezee et al. 2017).

b. Interior PV anomalies and diabatic heating

With $\varepsilon = 12.5$ and $\gamma = 0.0$, the amplitude of the PV anomalies at the top of the heating layer (blue stars in Fig. 6a) is almost twice as large as the PV anomalies at the bottom of the heating layer (red stars). As γ increases, the PV anomalies at the top of the heating layer weaken while the PV anomalies at the bottom of the heating layer strengthen. This response is in accordance with the increase in the heating step at the bottom of the heating
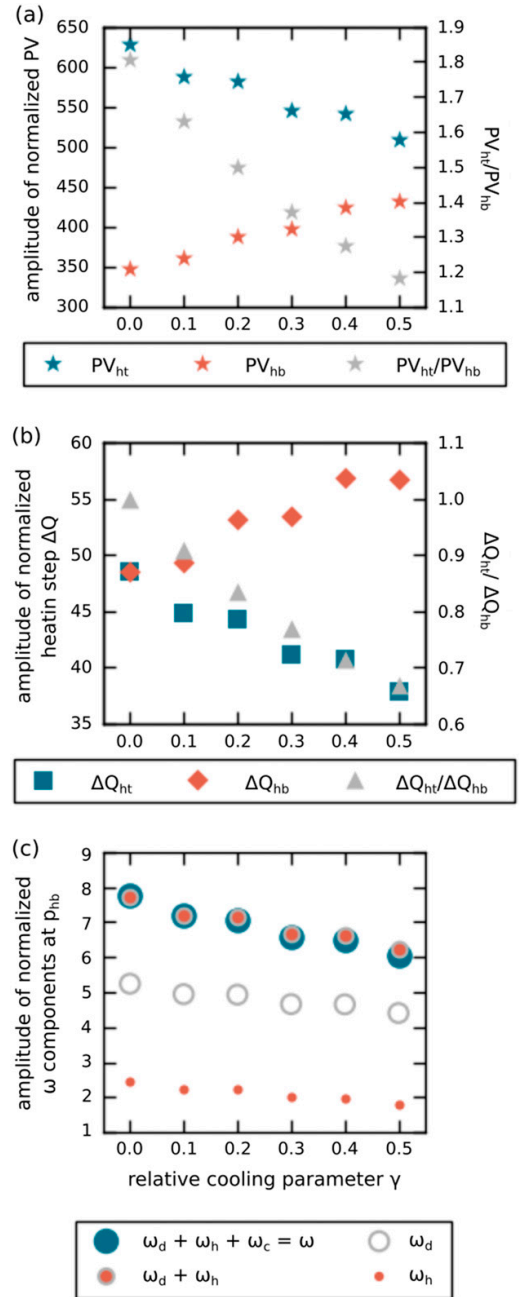

FIG. 6. (a) Amplitude of the PV anomalies at the top (blue) and bottom (red) of the heating layer and their relative amplitudes (gray). (b) Amplitude of the vertical difference of diabatic heating ΔQ around the top (blue) and bottom (red) of the heating layer and their relative amplitudes $\Delta Q_{ht}/\Delta Q_{hb}$ (gray). (c) Amplitude of ω_d (gray circles), ω_h (red dots), $\omega_d + \omega_h$ (red dots with gray circles), and $\omega = \omega_d + \omega_h + \omega_c$ (blue), all taken at the bottom of the heating layer. All quantities are nondimensional and normalized with respect to total energy and are shown for $\varepsilon = 12.5$ with varying relative cooling parameters γ.

layer and the decrease in the heating step at the top of the heating layer for increasing γ (Fig. 6b). The decrease of the heating step at the top of the heating layer must be related to reduced vertical motion, because that is the only parameter in the heating parameterization that is not fixed. Such a reduction in vertical motion has also an impact on the heating step at the bottom of the heating layer, but as latent cooling is added below the heating layer, there can still be a net increase of the heating step at this level.

The decrease in the PV anomalies at the top of the heating layer *relative* to the PV anomalies at the bottom of the heating layer (gray stars for $\varepsilon = 12.5$ in Fig. 6a) remains when examining other heating intensities where $\varepsilon \le 15$. The *absolute* change of the PV anomalies, however, depends on the relation between the reduction of midlevel latent heating and the increase in low-level latent cooling, which varies with heating intensity. For example, when $\varepsilon \to 15$, latent cooling weakens the diabatic PV anomalies at *both* levels, though more the upper anomalies than the lower anomalies (not shown), because the reduction of latent heating overcompensates the increase in the heating step at the bottom of the heating layer because of latent cooling. For weak heating intensities ($\varepsilon \to 0$), however, the reduction of latent heating by latent cooling is negligible and the PV anomalies at the top of the heating layer barely change for increasing latent cooling while the increase in the PV anomalies at the bottom of the heating layer is enhanced (not shown).

c. Diabatic heating and vertical motion

The zonal distribution of diabatic heating (contours in Fig. 7) is determined by the vertical motion at the bottom of the heating layer (shading in Fig. 7) and is mostly positioned in the warm and ascending southerly flow. This placement is consistent with midlatitude cyclones, where the primary cloud-producing flow is in the warm conveyor belt (e.g., Browning 1990).

The structure of the vertical motion remains similar when including latent heating and/or cooling and is mostly determined by the dynamic component ω_d (shading in Fig. 8). However, when diabatic effects are included, there is also a significant contribution from the component due to latent heating ω_h (black contours in Fig. 8). The amplitudes of both ω_d and ω_h at the bottom of the heating layer decrease when adding latent cooling (gray circles and red dots in Fig. 6c, respectively), contributing to a net decrease in the total vertical motion at this level (blue dots in Fig. 6c). This decrease in vertical motion is in accordance with a case study of midlatitude cyclones by Martínez-Alvarado et al. (2016) and with the decrease in absolute latent
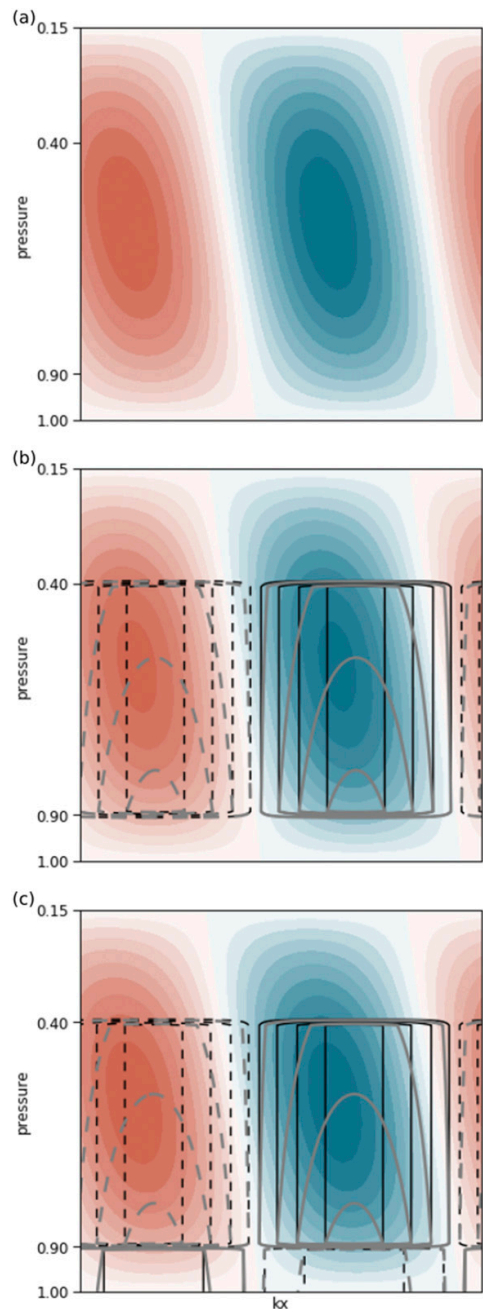

FIG. 7. As in Fig. 5, but for vertical motion (shading) and diabatic heating based on h (black contours) and $\tilde{h}$ (gray contours).
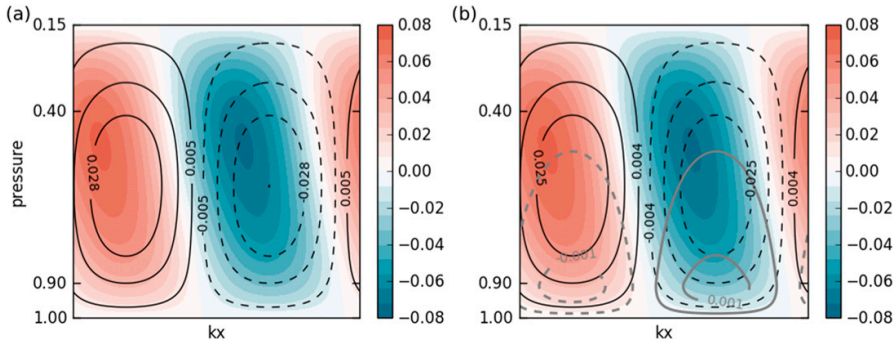
FIG. 8. Structure of the vertical motion components ω_d (shading), ω_h (black contours), and ω_c (gray contours) for the modes in Figs. 7b and 7c.

heating in the presence of latent cooling, as discussed in section 4b.

In contrast to the other components of vertical motion ω_d and ω_h, the component due to latent cooling ω_c increases when γ increases (not shown). However, since ω_c is both weaker and nearly in antiphase compared to the other vertical motion components (gray contours in Fig. 8), ω_c still contributes to a net reduction in vertical motion for increasing γ. This is evident when comparing the total vertical motion with the vertical motion that excludes ω_c (blue dots and red dots with the gray edge in Fig. 6c), where 12% of the total reduction of vertical motion from $\gamma = 0.0$ to $\gamma = 0.5$ stems from ω_c.

d. Relation between vertical motion and wavelength

As latent cooling is also related to increasing wavelengths (Fig. 3), the reduced vertical motion for increasing γ can also be related to the horizontal scale. For constant γ, an increase in wavelength is consistent with reduced vertical motion (Fig. 9), as expected from QG scaling $\omega(\partial/\partial p) \sim (U/L)R_0$ (e.g., Holton and Hakim 2012), where R_0 is the Rossby number. As long as γ is constant, this reduction with wavelength is true for all three components of ω (colored lines in Fig. 9), and holds for other reasonable values of ε and γ (not shown). When γ increases, however, there is, as noted in section 4c, a net increase in ω_c, despite the shift to longer wavelengths (not shown).

5. Energetics

To further elucidate the effect of latent cooling on baroclinic development we examine the diabatic contributions to the energetics. Following Lorenz (1955), the tendency of eddy available potential energy A_e can be expressed as

$$\frac{\partial A_e}{\partial t} = C_a + G_e - C_e, \qquad (12)$$

where

$$C_a = -\frac{\lambda}{S}\overline{\psi_x \psi_p}, \quad G_e = -\frac{1}{S}\overline{Q\psi_p}, \quad \text{and} \quad C_e = \overline{\omega\psi_p} \qquad (13)$$

represent the conversion from basic-state available potential energy to eddy available potential energy, the generation of eddy available potential energy from diabatic heating, and the conversion from eddy available potential energy to eddy kinetic energy, respectively. The bar denotes zonal and vertical averages. In this study, we split the diabatic term into components due to latent heating G_e^h and latent cooling G_e^c.
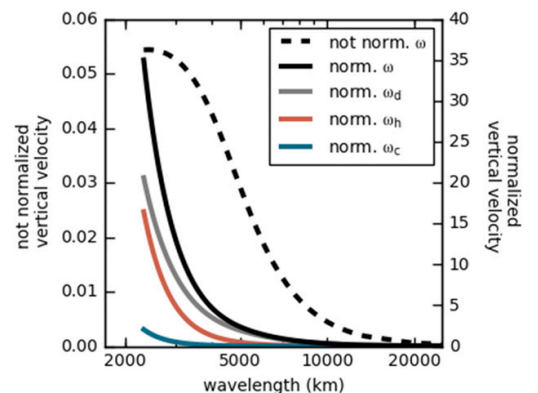

FIG. 9. Amplitude of nonnormalized (dashed) and normalized (solid) vertical motion at the bottom of the heating layer for $\varepsilon = 12.5$, $\gamma = 0.5$, and varying wavelengths. Black lines show total vertical motion, whereas colored lines show the different components.
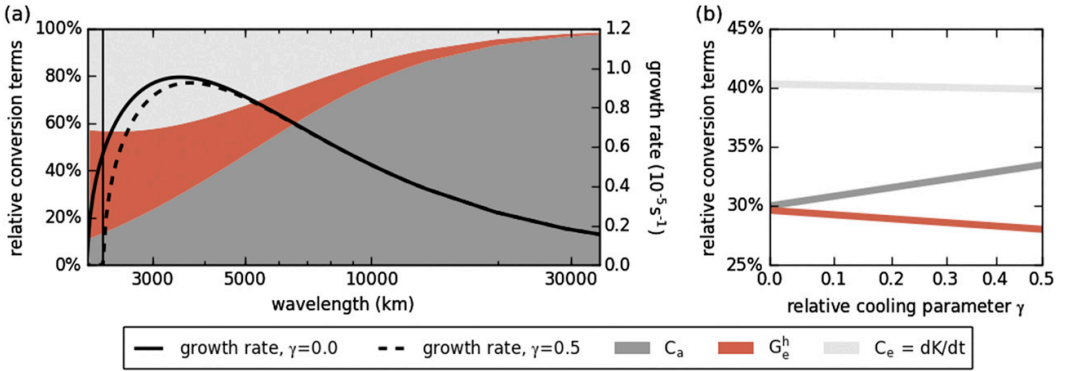
FIG. 10. Relative contributions to the energetics from $C_a = -(\lambda/S)\overline{\psi_x \psi_p}$ (dark gray), $G_e^h = -(1/S)\overline{Q\psi_p}$ (red), and $C_e = \overline{\omega\psi_p}$ (light gray) (a) with corresponding growth rates for $\gamma = 0.0$ (solid black) and $\gamma = 0.5$ (dashed black) and (b) for the most unstable mode with varying γ. The energetics in (a) are valid for both $\gamma = 0.0$ and $\gamma = 0.5$, but, as they can only be evaluated where the growth rate is nonzero, one should not consider the shading to the left of the shortwave cutoff (vertical line) for $\gamma = 0.5$. The change in the energetics with γ in (b) is only a result of the wavelength shift of the most unstable mode.

Although we find the contribution from G_e^c to be negligible (not shown), latent cooling still has an important indirect impact on the energetics through its modification of vertical motion and latent heating, and hence G_e^h.

The primary source of eddy available potential energy stems from G_e^h and C_e at short wavelengths and C_a at long wavelengths (Fig. 10), because G_e^h and C_e depend on the vertical motion, which is largest at short wavelengths (Fig. 9). Consistent with the decrease in vertical motion for increasing γ (Fig. 6c), the relative

importance of G_e^h and C_e decreases when latent cooling is included (Fig. 10b).

6. Sensitivity to heating profile

We investigate the sensitivity of our results to the shape of the idealized heating profile by diagnosing how the growth rate and structure respond to heating profiles that are more realistic than a step function. Motivated particularly by the heating distribution found in a simulation of a deep midlatitude cyclone studied by
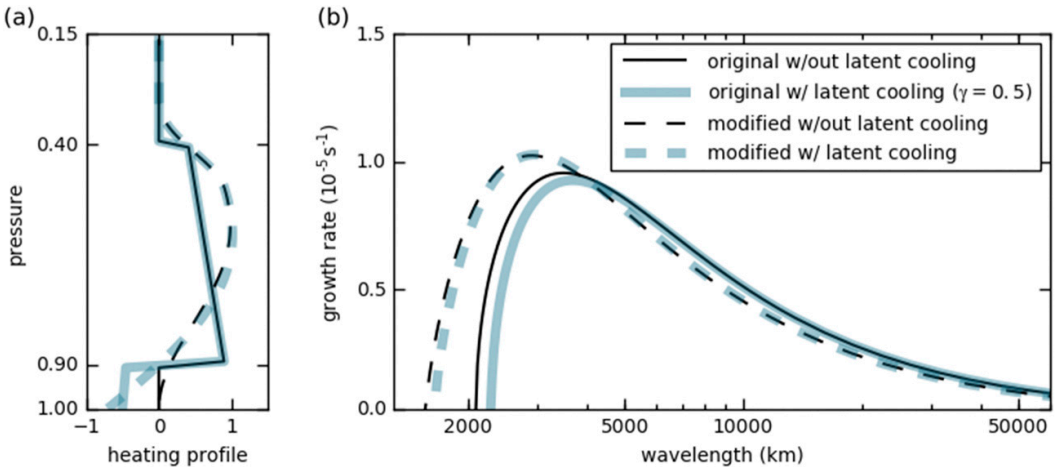

FIG. 11. (a) Original (solid) and modified (dashed) heating profiles $\bar{h}$ without latent cooling (black) and with latent cooling (blue, $\gamma = 0.5$ in original profile) for $\varepsilon = 12.5$. See text for definition of profiles. (b) Growth rates corresponding to the heating profiles in (a) for varying wavelengths.
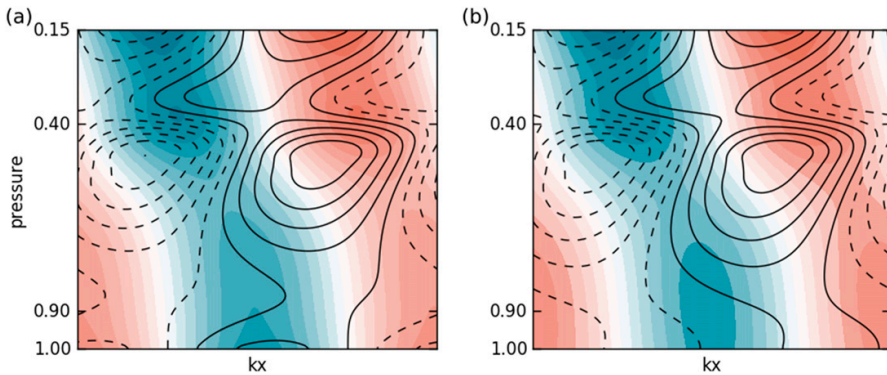
FIG. 12. Structure of streamfunction (shading) and temperature (contours) for the most unstable mode using the modified heating profiles in Fig. 11 with (a) latent heating only (dashed black profile in Fig. 11a), and (b) latent heating and cooling (dashed blue profile in Fig. 11a).

Dearden et al. (2016) as well as heating distributions from other case studies of midlatitude cyclones (e.g., Pauley and Nieman 1992; Joos and Forbes 2016), we devise the two modified heating profiles shown as dashed lines in Fig. 11a (see the appendix for details). Note that Fig. 11a shows the physical profile of heating $\tilde{h}$ obtained by multiplying the heating profile h with pressure p (see section 2b), yielding a better basis for comparison to the heating distribution in the previously mentioned case studies.

When using the modified profiles, the maximum growth rate is somewhat larger and shifted to shorter scales (see Fig. 11b), although latent cooling still has a stabilizing effect. The modified structures of the streamfunction and the temperature (Fig. 12) are smoother than the original structures shown in Fig. 5. However, they possess many of the same features, such as the collocation between warm (cold) air and upward (downward) motion (not shown), as well as the secondary maxima in the streamfunction at the top of the heating layer. The main difference is the shift from the two local maxima in temperature at the heating boundaries to one maximum around $p = 0.5$, as well as reduced maxima in temperature at the surface.

The structures of other quantities, such as vertical motion, diabatic heating, and meridional velocity, are also smoother but remain qualitatively similar when modifying the heating profile (not shown). These findings demonstrate that the idealized heating profile yields qualitatively meaningful results and that our interpretation is also applicable to more realistic heating profiles.

7. Sensitivity to static stability

So far, we assumed a constant basic-state static stability S. However, as argued by, for example, Lapeyre and Held (2004) and O'Gorman (2011), the effective stratification reduces when the atmosphere is moist, because parcel displacements in the presence of latent heating and cooling are nearly moist adiabatic. To inspect whether these moist effects are accounted for in our model, we combine the terms involving static stability and diabatic heating in the thermodynamic equation

$$S\omega + \frac{\varepsilon h \omega_{\text{hb}}}{2} = -\frac{RT_0}{p}\left(\frac{\partial \ln\theta_0}{\partial p}\omega + \frac{\partial F}{\partial p}\omega_{\text{hb}}\right)$$
$$\neq -\frac{RT_0}{p}\frac{\partial(\ln\theta_0 + f)}{\partial p}\omega, \qquad (14)$$

where θ_0 is the basic-state potential temperature and $\partial F/\partial p = \{[-\varepsilon h(p)]/2\}(p/RT_0) = (\partial f/\partial p)(\omega/\omega_{\text{hb}})$ represents the moist contribution to the effective stratification. Since the heating parameterization is based on ω_{hb}, and not ω, it is not straightforward to define an effective stratification expressed as the right-hand side of the inequality in (14). Furthermore, the effect of diabatic forcing on the effective stratification can be both positive and negative, depending on the sign of the heating profile h. The moist effects on stratification are thus only partly accounted for. We examine these effects further by testing the sensitivity of our results to changes in S. As we cannot accommodate any zonal variations of the basic-state static stability in our model, we reduce the stability in both the regions of ascent and descent in the baroclinic wave.

To test the sensitivity of our results to reduced stratification, we investigate how reducing the static stability by 25% affects the growth rates when latent heating and cooling are included. In addition to our reference profile S, we introduce

$$S_h = 4 - H(p - 0.41) + H(p - 0.89) \qquad (15)$$

and

$$S_{hc} = 4 - H(p - 0.41), \qquad (16)$$

where H is the Heaviside step function. These profiles prescribe reduced stability either in the heating layer only S_h or in the heating *and* the cooling layer S_{hc}. We argue that S_{hc} is most realistic, as the stratification below the heating layer is also nearly moist adiabatic because of evaporation and associated latent cooling. Note that the steps in static stability introduce PV anomalies and levels with basic-state meridional PV gradients because of the nonzero vertical gradients of S_h and S_{hc}.

When the static stability is reduced in parts of the model domain (profiles S_h and S_{hc}), the growth rates increase and the most unstable solution moves to shorter wavelengths (Fig. 13). This is expected, because a reduced stability is associated with enhanced vertical interaction between PV anomalies. The growth rates increase most when the stability is reduced all the way down to the surface S_{hc}, which is due to a deeper layer of reduced stability and hence a greater net reduction of the overall stability. For all stability profiles, the growth rates decrease when latent cooling is included, in accordance with the results in section 3.

We also tested the impact of the vertical extent of the layer of reduced effective stratification by varying the location and the magnitude of the reduced stability (not shown). When the upper boundary of the layer of weaker stability is shifted from 410 to 500 hPa and/or the lower boundary is shifted from 890 to 800 hPa, the growth rates decrease, because the overall reduction of stability is weaker. Furthermore, when S_h and S_{hc} are adjusted so that the mean stability is identical for all profiles, the growth rates are largest when the stability is not constant, that is, for S_h and S_{hc}. For these cases, the increased growth rates cannot be explained by a net reduction of overall static stability and are more likely related to the superpositioning of the diabatic PV anomalies and the PV anomalies induced by the steps in the static stability profile. Independent of the changes in static stability in this section, the effect of latent cooling remains detrimental for baroclinic instability.

8. Concluding remarks

Including diabatic effects representing both midtropospheric latent heating and low-level latent cooling with heating intensities comparable to realistic midlatitude cyclones into the Eady model, we find that latent cooling reduces baroclinic growth and shifts the most unstable mode to longer wavelengths. For quantitative
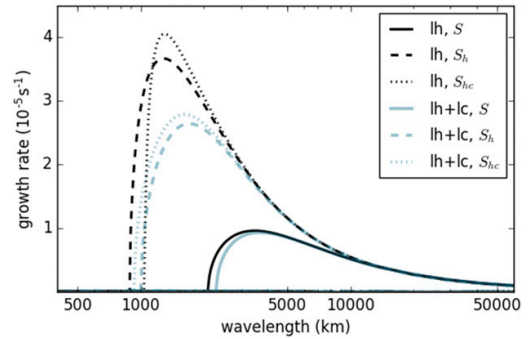

FIG. 13. Growth rates for various stability profiles: S (solid), S_h (dashed), and S_{hc} (dotted), for $\varepsilon = 12.5$ and only latent heating (black, $\gamma = 0.0$) as well as latent heating and cooling (blue, $\gamma = 0.5$). See text for definition of stability profiles.

comparison, we normalize the results by total energy and find that the reduced growth is consistent with weakening both vertical motion and latent heating within the cyclone when low-level cooling is included. Thus, latent cooling is primarily an indirect effect that influences midlatitude cyclones by reducing the intensifying effect of latent heating.

The reduction of latent heating weakens the vertical heating gradients at the top and bottom of the heating layer and thus leads to weaker diabatically induced PV anomalies. The decrease in the vertical heating gradient at the bottom of the heating layer, however, is counteracted by the latent cooling below. Hence, the net change of the PV anomaly at the bottom of the heating layer depends on the relative contributions from the reduced latent heating above and latent cooling below. Nevertheless, the overall effect of latent cooling is an enhancement of the low-level PV anomaly *relative* to the PV anomaly at the top of the heating layer.

The direct contribution from latent cooling to the generation of eddy available potential energy is negligible. However, the contribution from latent heating decreases when latent cooling is included. Thus, the influence of latent cooling on cyclone development is primarily indirect through suppression of vertical motion and latent heating.

We obtain similar results when using heating profiles mimicking heating distributions from realistic case studies of midlatitude cyclones. Furthermore, when testing the sensitivity of our results to stability profiles that take into account that the effective static stability is reduced in a saturated moist atmosphere, the response to latent cooling remains qualitatively the same. The insensitivity to these variations proves the robustness of our results obtained with the idealized model setup.

Consistent with previous studies, our findings confirm that latent cooling enhances the low-level PV anomaly

in midlatitude cyclones for realistic heating intensities at the early development stage. Overall, however, we find that latent cooling is detrimental to cyclone development through reducing vertical motion and latent heating. These indirect effects should be further assessed using more complex three-dimensional models with the capacity to omit the effects of latent cooling to test their influence on cyclone development.

APPENDIX

Modified Heating Profiles

The modified heating profiles used for the sensitivity study in section 6 are

$$
h(p) = \beta \times
\begin{cases}
0 & \text{for} \quad p < p_{\text{ht}} - \delta \\
\sin^2\left\{\dfrac{\pi[p - (p_{\text{ht}} - \delta)]}{2[(p_{\text{ht}} + \delta) - (p_{\text{ht}} - \delta)]}\right\} & \text{for} \quad p_{\text{ht}} - \delta < p < p_{\text{ht}} + \delta \\
1 & \text{for} \quad p_{\text{ht}} + \delta < p < p_{\text{hb*}} - \delta^* \\
\sin^2\left\{\dfrac{\pi[p - (p_{\text{hb*}} + \delta^*)]}{2[(p_{\text{hb*}} + \delta^*) - (p_{\text{hb*}} - \delta^*)]}\right\} & \text{for} \quad p_{\text{hb*}} - \delta^* < p < p_{\text{hb*}} + \delta^* \\
0 & \text{for} \quad p_{\text{hb*}} + \delta^* < p
\end{cases}
, \quad (A1)
$$

$$
h(p) = \beta \times
\begin{cases}
0 & \text{for} \quad p < p_{\text{ht}} - \delta \\
\sin^2\left\{\dfrac{\pi[p - (p_{\text{ht}} - \delta)]}{2[(p_{\text{ht}} + \delta) - (p_{\text{ht}} - \delta)]}\right\} & \text{for} \quad p_{\text{ht}} - \delta < p < p_{\text{ht}} + \delta \\
1 & \text{for} \quad p_{\text{ht}} + \delta < p < p_{\text{hb*}} - \delta^* \\
\sin\left\{\dfrac{\pi[p - p_{\text{hb}}]}{2[p_{\text{hb*}} - \delta^* - p_{\text{hb}}]}\right\} & \text{for} \quad p_{\text{hb*}} - \delta^* < p,
\end{cases}
\quad (A2)
$$

where the former (latter) excludes (includes) latent cooling at lower levels, and δ (δ^*) determines the sharpness of the smooth curve around $p = p_{\text{ht}}$ ($p = p_{\text{hb*}}$). The profiles shown in Fig. 11a are obtained by multiplying (A1) and (A2) by p, where $\beta = 1.8$, $\delta = 0.1$, $\delta^* = 0.25$, and $p_{\text{hb*}} = 0.75$.

REFERENCES

Ahmadi-Givi, F., G. Graig, and R. Plant, 2004: The dynamics of a midlatitude cyclone with very strong latent-heat release. *Quart. J. Roy. Meteor. Soc.*, **130**, 295–323, https://doi.org/10.1256/qj.02.226.

Anderson, E., and Coauthors, 1999: *LAPACK Users' Guide.* 3rd ed. Society for Industrial and Applied Mathematics, 407 pp.

Barth, M. C., and D. B. Parsons, 1996: Microphysical processes associated with intense frontal rainbands and the effect of evaporation and melting on frontal dynamics. *J. Atmos. Sci.*, **53**, 1569–1586, https://doi.org/10.1175/1520-0469(1996)053<1569:MPAWIF>2.0.CO;2.

Bretherton, F. P., 1966: Baroclinic instability and the short wavelength cut-off in terms of potential instability. *Quart. J. Roy. Meteor. Soc.*, **92**, 335–345, https://doi.org/10.1002/qj.49709239303.

Browning, K. A., 1990: Organization of clouds and precipitation in extratropical cyclones. *Extratropical Cyclones: The Erik Palmén Memorial Volume*, C. W. Newton and E. O. Holopainen, Eds., Amer. Meteor. Soc., 129–153.

Clough, S., and R. Franks, 1991: The evaporation of frontal and other stratiform precipitation. *Quart. J. Roy. Meteor. Soc.*, **117**, 1057–1080, https://doi.org/10.1002/qj.49711750109.

Craig, G., and H.-R. Cho, 1988: Cumulus heating and CISK in the extratropical atmosphere. Part I: Polar lows and comma clouds. *J. Atmos. Sci.*, **45**, 2622–2640, https://doi.org/10.1175/1520-0469(1988)045<2622:CHACIT>2.0.CO;2.

Crezee, B., H. Joos, and H. Wernli, 2017: The microphysical building blocks of low-level potential vorticity anomalies in an idealized extratropical cyclone. *J. Atmos. Sci.*, **74**, 1403–1416, https://doi.org/10.1175/JAS-D-16-0260.1.

Davis, C., and K. Emanuel, 1991: Potential vorticity diagnostics of cyclogenesis. *J. Atmos. Sci.*, **119**, 1929–1953, https://doi.org/10.1175/1520-0493(1991)119<1929:PVDOC>2.0.CO;2.

Dearden, C., G. Vaughan, T. Tsai, and J.-P. Chen, 2016: Exploring the diabatic role of ice microphysical processes in two North Atlantic summer cyclones. *Mon. Wea. Rev.*, **144**, 1249–1272, https://doi.org/10.1175/MWR-D-15-0253.1.

De Vries, H., J. Methven, T. H. Frame, and B. J. Hoskins, 2010: Baroclinic waves with parameterized effects of moisture interpreted using Rossby wave components. *J. Atmos. Sci.*, **67**, 2766–2784, https://doi.org/10.1175/2010JAS3410.1.

Eady, E. T., 1949: Long-waves and cyclone waves. *Tellus*, **1** (3), 33–52, https://doi.org/10.3402/tellusa.v1i3.8507.

Emanuel, K. A., M. Fantini, and A. J. Thorpe, 1987: Baroclinic instability in an environment of small stability to slantwise moist convection. Part I: Two-dimensional models. *J. Atmos. Sci.*, **44**, 1559–1573, https://doi.org/10.1175/1520-0469(1987)044<1559:BIIAEO>2.0.CO;2.

Forbes, R. M., and P. A. Clark, 2003: Sensitivity of extratropical cyclone mesoscale structure to the parametrization of ice microphysical processes. *Quart. J. Roy. Meteor. Soc.*, **129**, 1123–1148, https://doi.org/10.1256/qj.01.171.

Heifetz, E., C. Bishop, B. Hoskins, and J. Methven, 2004: The counter-propagating Rossby-wave perspective on baroclinic instability. I: Mathematical basis. *Quart. J. Roy. Meteor. Soc.*, **130**, 211–231, https://doi.org/10.1002/qj.200413059610.

Holton, J. R., and G. J. Hakim, 2012: *An Introduction to Dynamic Meteorology.* 5th ed. International Geophysics Series, Vol. 88, Academic Press, 532 pp.

Hoskins, B. J., M. E. McIntyre, and A. W. Robertson, 1985: On the use and significance of isentropic potential vorticity maps. *Quart. J. Roy. Meteor. Soc.*, **111**, 877–946, https://doi.org/10.1002/qj.49711147002.

Huang, H.-C., and K. A. Emanuel, 1991: The effects of evaporation on frontal circulations. *J. Atmos. Sci.*, **48**, 619–628, https://doi.org/10.1175/1520-0469(1991)048<0619:TEOEOF>2.0.CO;2.

Joos, H., and H. Wernli, 2012: Influence of microphysical processes on the potential vorticity development in a warm conveyor belt: A case-study with the limited-area model COSMO. *Quart. J. Roy. Meteor. Soc.*, **138**, 407–418, https://doi.org/10.1002/qj.934.

——, and R. M. Forbes, 2016: Impact of different IFS microphysics on a warm conveyor belt and the downstream flow evolution. *Quart. J. Roy. Meteor. Soc.*, **142**, 2727–2739, https://doi.org/10.1002/qj.2863.

Kuo, Y.-H., M. Shapiro, and E. G. Donall, 1991: The interaction between baroclinic and diabatic processes in a numerical simulation of a rapidly intensifying extratropical marine cyclone. *Mon. Wea. Rev.*, **119**, 368–384, https://doi.org/10.1175/1520-0493(1991)119<0368:TIBBAD>2.0.CO;2.

Lapeyre, G., and I. M. Held, 2004: The role of moisture in the dynamics and energetics of turbulent baroclinic eddies. *J. Atmos. Sci.*, **61**, 1693–1710, https://doi.org/10.1175/1520-0469(2004)061<1693:TROMIT>2.0.CO;2.

Lin, S. C., and P. J. Smith, 1979: Diabatic heating and generation of available potential energy in a tornado-producing extratropical cyclone. *Mon. Wea. Rev.*, **107**, 1169–1183, https://doi.org/10.1175/1520-0493(1979)107<1169:DHAGOA>2.0.CO;2.

Lorenz, E. N., 1955: Available potential energy and the maintenance of the general circulation. *Tellus*, **7**, 157–167, https://doi.org/10.3402/tellusa.v7i2.8796.

Mak, M., 1994: Cyclogenesis in a conditionally unstable moist baroclinic atmosphere. *Tellus*, **46A**, 14–33, https://doi.org/10.3402/tellusa.v46i1.15424.

Manabe, S., 1956: On the contribution of heat released by condensation to the change in pressure pattern. *J. Meteor. Soc. Japan*, **34**, 308–320, https://doi.org/10.2151/jmsj1923.34.6_308.

Martínez-Alvarado, O., F. Weidle, and S. L. Gray, 2010: Sting jets in simulations of a real cyclone by two mesoscale models. *Mon. Wea. Rev.*, **138**, 4054–4075, https://doi.org/10.1175/2010MWR3290.1.

——, S. L. Gray, and J. Methven, 2016: Diabatic processes and the evolution of two contrasting summer extratropical cyclones. *Mon. Wea. Rev.*, **144**, 3251–3276, https://doi.org/10.1175/MWR-D-15-0395.1.

Moore, R. W., and M. T. Montgomery, 2004: Reexamining the dynamics of short-scale, diabatic Rossby waves and their role in midlatitude moist cyclogenesis. *J. Atmos. Sci.*, **61**, 754–768, https://doi.org/10.1175/1520-0469(2004)061<0754:RTDOSD>2.0.CO;2.

O'Gorman, P. A., 2011: The effective static stability experienced by eddies in a moist atmosphere. *J. Atmos. Sci.*, **68**, 75–90, https://doi.org/10.1175/2010JAS3537.1.

Parker, D. J., and A. J. Thorpe, 1995: Conditional convective heating in a baroclinic atmosphere: A model of convective frontogenesis. *J. Atmos. Sci.*, **52**, 1699–1711, https://doi.org/10.1175/1520-0469(1995)052<1699:CCHIAB>2.0.CO;2.

Pauley, P. M., and S. J. Nieman, 1992: A comparison of quasigeostrophic and nonquasigeostrophic vertical motions for a model-simulated rapidly intensifying marine extratropical cyclone. *Mon. Wea. Rev.*, **120**, 1108–1134, https://doi.org/10.1175/1520-0493(1992)120<1108:ACOQAN>2.0.CO;2.

Pomroy, H. R., and A. J. Thorpe, 2000: The evolution and dynamical role of reduced upper-tropospheric potential vorticity in intensive observing period one of FASTEX. *Mon. Wea. Rev.*, **128**, 1817–1834, https://doi.org/10.1175/1520-0493(2000)128<1817:TEADRO>2.0.CO;2.

Rantanen, M., J. Räisänen, J. Lento, O. Stepanyuk, O. Räty, V. A. Sinclair, and H. Järvinen, 2017: OZO v. 1.0: Software for solving a generalised omega equation and the Zwack–Okossi height tendency equation using WRF Model output. *Geosci. Model Dev.*, **10**, 827–841, https://doi.org/10.5194/gmd-10-827-2017.

Robertson, F., and P. Smith, 1983: The impact of model moist processes on the energetics of extratropical cyclones. *Mon. Wea. Rev.*, **111**, 723–744, https://doi.org/10.1175/1520-0493(1983)111<0723:TIOMMP>2.0.CO;2.

Smith, P. J., 1980: The energetics of extratropical cyclones. *Rev. Geophys.*, **18**, 378–386, https://doi.org/10.1029/RG018i002p00378.

Snyder, C., and R. S. Lindzen, 1991: Quasi-geostrophic wave-CISK in an unbounded baroclinic shear. *J. Atmos. Sci.*, **48**, 76–86, https://doi.org/10.1175/1520-0469(1991)048<0076:QGWCIA>2.0.CO;2.

Stepanyuk, O., J. Räisänen, V. A. Sinclair, and H. Järvinen, 2017: Factors affecting atmospheric vertical motions as analyzed with a generalized omega equation and the OpenIFS model. *Tellus*, **69**, 1271563, https://doi.org/10.1080/16000870.2016.1271563.

Stoelinga, M. T., 1996: A potential vorticity–based study of the role of diabatic heating and friction in a numerically simulated baroclinic cyclone. *Mon. Wea. Rev.*, **124**, 849–874, https://doi.org/10.1175/1520-0493(1996)124<0849:APVBSO>2.0.CO;2.

Terpstra, A., T. Spengler, and R. W. Moore, 2015: Idealised simulations of polar low development in an Arctic moist baroclinic environment. *Quart. J. Roy. Meteor. Soc.*, **141**, 1987–1996, https://doi.org/10.1002/qj.2507.

Vincent, D. G., G. B. Pant, and H. J. Edmon Jr., 1977: Generation of available potential energy of an extratropical cyclone system. *Mon. Wea. Rev.*, **105**, 1252–1265, https://doi.org/10.1175/1520-0493(1977)105<1252:GOAPEO>2.0.CO;2.

Whitaker, J. S., and C. A. Davis, 1994: Cyclogenesis in a saturated environment. *J. Atmos. Sci.*, **51**, 889–907, https://doi.org/10.1175/1520-0469(1994)051<0889:CIASE>2.0.CO;2.

Paper II

Direct and Indirect Effects of Surface Fluxes on Moist Baroclinic Development in an Idealized Framework

Haualand, K. F. and Spengler, T.

Direct and Indirect Effects of Surface Fluxes on Moist Baroclinic Development in an Idealized Framework

KRISTINE F. HAUALAND AND THOMAS SPENGLER

Geophysical Institute, University of Bergen, and Bjerknes Centre for Climate Research, Bergen, Norway

ABSTRACT

The convoluted role of surface sensible and latent heat fluxes on moist baroclinic development demands a better understanding to disentangle their local and remote effects. Including diabatic effects in the Eady model, the direct effects of surface fluxes on the diabatic generation of eddy available potential energy as well as their indirect effects through modifications of the circulation and latent heating are investigated. It is shown that surface sensible heat fluxes have a minor impact, irrespective of their position and parameterization, while latent heating in the region equivalent to the warm conveyor belt is the dominant diabatic source for development. Downward surface sensible heat fluxes in proximity of the warm conveyor belt results in structural modifications that increase the conversion from basic-state available potential energy to eddy available potential energy, while concomitantly weakening the ascent and hence latent heating. The detrimental effects are easily compensated through provision of additional moisture into the warm conveyor belt. Upward surface heat fluxes in the cold sector, on the other hand, are detrimental to growth. When downward (upward) surface sensible heat fluxes are located below the equivalent of the warm conveyor belt, the diabatically induced PV anomaly at the bottom of the latent heating layer becomes dominant (less dominant). Shifting the downward surface sensible heat fluxes away from the warm conveyor belt results in substantial changes in the growth rate, latent heat release, low-level structure, and energetics, where the effect of surface sensible heat fluxes might even be beneficial.

1. Introduction

The influence of surface sensible and latent heat fluxes on midlatitude cyclone development is uncertain and varies with environmental conditions in the atmosphere and ocean (e.g., Nuss and Anthes 1987; Kuo and Reed 1988; Mullen and Baumhefner 1988). Nuss and Anthes (1987) found that the effect of surface fluxes varies from reducing the growth rate of extratropical cyclones by 25% to enhancing it by 15%. Moreover, when cyclones move over regions with different air–sea temperature contrasts, the role of surface fluxes often changes substantially during the development (Kuo et al. 1991a) and may even reverse or partially cancel (Langland et al. 1995). With state-of-the-art numerical weather prediction models still struggling to correctly represent the amount and

location of diabatic processes in cyclone development (e.g., Schäfler et al. 2018) as well as climate models featuring significant biases in sea surface temperatures resulting in a misrepresentation of storm tracks (e.g., Keeley et al. 2012; Lee et al. 2018), improving our understanding of the influence of surface fluxes on cyclone development will allow us to identify associated sources of model biases and forecast uncertainties.

While surface latent heat fluxes are usually upward in most parts of the cyclone (e.g., Carrera et al. 1999; Zhang et al. 1999), surface sensible heat fluxes often feature a dipole with upward fluxes in the cold sector and downward fluxes in the warm sector of the cyclone (e.g., Danard and Ellenton 1980; Fleagle and Nuss 1985; Neiman and Shapiro 1993; Sinclair et al. 2010; Booth et al. 2012). Such a distribution of surface sensible heat fluxes can reduce low-level baroclinicity (Branscome et al. 1989; Zhang and Stone 2011) and ascent in the

Corresponding author: Kristine Flacké Haualand, kristine.haualand@uib.no

warm sector of the cyclone (Kuo et al. 1991a), potentially weakening cyclone growth (Haltiner 1967; Kuo and Low-Nam 1990).

Under different environmental conditions, however, surface sensible heat fluxes can also be upward in the warm sector. For example, during the early phase of an explosive midlatitude cyclone studied by Kuo et al. (1991a), polar air from a previous cold-air outbreak resulted in upward surface sensible heat fluxes in the warm sector. When excluding these fluxes in numerical simulations of the storm, the cyclone development was considerably weaker. This impact from surface fluxes is supported by the climatological study by Gyakum and Danielson (2000), where the strongest cyclogenesis was associated with cold air downstream of the developing cyclone in conjunction with higher sea surface temperatures and thereby larger surface fluxes. Furthermore, strong upward oceanic surface fluxes warmed, moistened, and destabilized the cold boundary layer of the vigorous Presidents' Day snowstorm, resulting in a strong low-level baroclinic zone that aided cyclone development at an early stage (Bosart 1981). Thus, under certain conditions, surface sensible heat fluxes can enhance, rather than weaken, low-level baroclinicity while reducing static stability (Reed and Albright 1986; Atlas 1987; Carrera et al. 1999), yielding favorable conditions for cyclone intensification.

Another contribution to cyclone growth is associated with surface latent heat fluxes that moisten the air in the boundary layer (Mailhot and Chouinard 1989). Combining this effect with a reduced static stability can lead to substantially enhanced latent heating and cyclone growth (Uccellini et al. 1987; Nuss and Anthes 1987; Carrera et al. 1999; Hirata et al. 2019). Zhang et al. (1999) stressed the importance of this moist effect on midlatitude cyclone development and found the impact of surface heat fluxes only to be significant when latent heating was included in the numerical experiments. As latent heating strongly intensifies and alters cyclone development (e.g., Craig and Cho 1988; Kuo et al. 1991b; Balasubramanian and Yau 1996), the influence of surface fluxes should be studied in conjunction with latent heating.

Investigating both of these diabatic effects in baroclinic life cycle experiments using a primitive equation global spectral model, Gutowski and Jiang (1998) found that surface heat fluxes destabilize the cold sector and stabilize the warm sector, resulting in a shift of convective heating to the cold sector. Consequently, in a follow-up study including constant surface sensible heat fluxes, Jiang and Gutowski (2000) examined the effect of

convective heating only above the cold sector. While surface fluxes can indeed modify the convective heating in the cold sector, the impact on the warm conveyor belt, where most of the latent heating occurs (Browning 1990), is probably more crucial for the development of the storm.

To investigate the role of surface fluxes in a framework that includes latent heating in the warm conveyor belt, we use the numerical extension of Mak's (1994) 2D quasigeostrophic (QG) linear model that was introduced by Haualand and Spengler (2019, hereafter HS19). This model is based on the Eady (1949) model and includes latent heating proportional to low-level vertical motion. Here, we further extend the model with different parameterizations of surface sensible heat fluxes based on either air–sea temperature differences (similar to Mak 1998), warm-air advection, or the location and intensity of the warm conveyor belt and investigate the impact of varying their intensity and location on the growth rate, structure, and energetics of the baroclinic wave in the presence of latent heating. We focus on the incipient stage of midlatitude cyclones, as later stages are typically highly nonlinear (e.g., Kuo et al. 1991b) and therefore inadequately represented by our linear model.

While surface sensible heat fluxes directly affect baroclinic development by altering the diabatic generation of eddy available potential energy, surface sensible and latent heat fluxes can also *indirectly* influence baroclinic development through changes in the circulation and moisture supply. For example, Boutle et al. (2010), Pfahl et al. (2014), and Dacre et al. (2019) found that surface latent heat fluxes remote from the cyclone area strongly control the input of moisture into the warm conveyor belt and hence the latent heat release. To examine and quantify this indirect effect of surface latent heat fluxes, we vary the latent heating intensity to evaluate the sustained surface latent heat fluxes needed to provide the additional moisture supply to the warm conveyor belt to overcome the detrimental effects from local surface sensible heat fluxes.

2. Model

a. Basic equations and model setup

We extend the linear 2D QG model formulated by Mak (1994) and HS19, which includes different diabatic forcings in the Eady (1949) model, by implementing various formulations of surface sensible heat fluxes. Following Mak (1994), we use pressure as the vertical coordinate and assume wavelike solutions in the x direction for the QG streamfunction ψ and vertical motion ω:
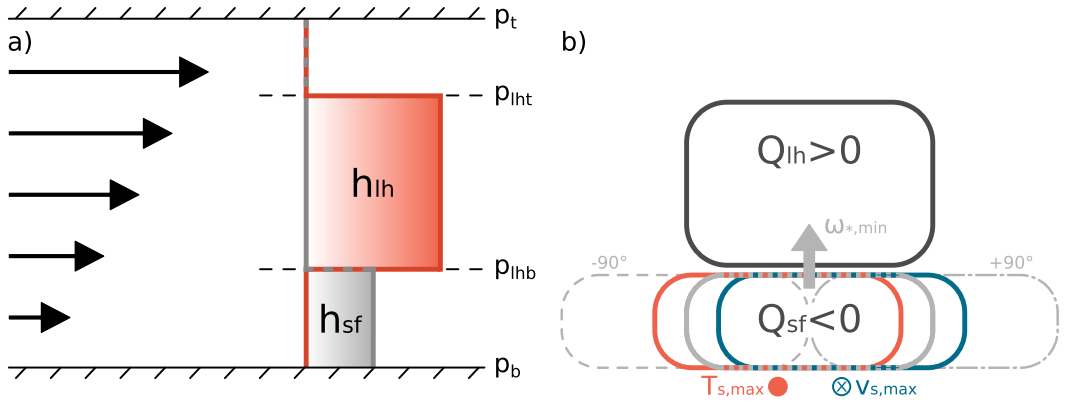
FIG. 1. Schematic of (a) the linearly increasing zonal wind with decreasing pressure (black arrows) and vertical profiles of latent heating (red) and surface fluxes (gray) and (b) vertical and zonal locations of downward surface sensible heat fluxes relative to the area of latent heating for the formulations based on T_s [(8), red], v_s [(9), blue], and ω_* [(11), gray]. Black dashed lines in (a) indicate heating boundaries where internal diabatically produced PV can form. Gray dot–dashed and dashed lines in (b) respectively indicate the location of the surface fluxes based on a $+90°$ and $-90°$ zonal phase shift relative to ω_*.

$$[\psi, \omega] = \mathrm{Re}\{[\hat{\psi}(p), \hat{\omega}(p)]\exp[i(kx - \sigma t)]\}, \quad (1)$$

where the hat denotes Fourier transformed variables, k is the zonal wavenumber, and σ is the wave frequency. The nondimensionalized ω and potential vorticity (PV) equations can then be expressed as

$$\frac{d^2\hat{\omega}}{dp^2} - Sk^2\hat{\omega} = i2\lambda k^3\hat{\psi} + k^2\hat{Q} \quad (2)$$

and

$$(\bar{u}k - \sigma)\left(\frac{d^2\hat{\psi}}{dp^2} - Sk^2\hat{\psi}\right) = i\frac{d\hat{Q}}{dp}, \quad (3)$$

where $Q = Q_{lh} + Q_{sf}$ is the diabatic heating rate *divided by pressure*, representing both latent heating Q_{lh} and heating associated with surface sensible heat fluxes Q_{sf}, S is the basic-state static stability as defined in HS19, λ is the basic-state vertical wind shear, and $\bar{u}(p) = \lambda(p_b - p) + u_0$ is the basic-state zonal wind (arrows in Fig. 1a). The set of equations is completed with the boundary conditions $\hat{\omega} = 0$ at p_t and p_b together with the thermodynamic equation

$$(\bar{u}k - \sigma)\frac{d\hat{\psi}}{dp} + i\hat{Q} + \lambda k\hat{\psi} = 0 \quad \text{at} \quad p = p_t, p_b, \quad (4)$$

where p_t and p_b are the pressure at the top and bottom of the domain, respectively.

For simplicity, we assume constant S and λ. Note that Mak (1998) prescribed S as a step function with a smaller value in the lowest layer. Our choice of a constant S is based on the argument that in the presence of latent heating, the effective static stability not only reduces in the surface flux layer but also in the latent heating layer where parcel displacements are nearly moist adiabatic (HS19). Furthermore, the effect of reduced stratification related to moist processes and surface fluxes is incorporated partially through the diabatic heating (see HS19 for further clarification). Following HS19, we refer to $d\psi/dp$, which is proportional to the negative density perturbation, as temperature, and choose representable model parameters for large-scale midlatitude flow (see Table 1). The only difference from Mak (1994) and HS19 is a uniform increase of $\bar{u}$ by $u_0 = 4\,\mathrm{m\,s^{-1}}$, consistent with the surface flux implementation introduced by Mak (1998), whereas the differences from Mak (1998) are in S (as noted above), λ, and p_t.

b. Parameterization of latent heating

Following Mak (1994), latent heating *divided by pressure* is proportional to upward motion at the bottom of the latent heating layer and is parameterized as

$$\hat{Q}_{lh} = -\frac{\varepsilon_{lh}h_{lh}(p)}{2}\hat{\omega}_*(k), \quad (5)$$

TABLE 1. Nondimensional values of model parameters. Value from HS19 (Mak 1998) is indicated in parentheses (square brackets) if different from this study. See Mak (1998) for a detailed description of S.

Parameter	S	λ	u_0	f	p_t	p_b
Nondimensional value	4 [*]	3.5 [5.0]	0.4 (0.0)	1	0.15 [0.0]	1

TABLE 2. Values of nondimensional surface flux intensity parameter (ε_{sf}) and respective units for different surface flux parameterizations.

Surface flux parameterization	T_s	v_s	$\omega_{*,0°}$	$\omega_{*,-90°}$	$\omega_{*,+90°}$	$\omega_{*,180°}$
ε_{sf} (nondimensional)	1.5	1.4	3.12	3.12	−3.12	−3.12
Units of dimensional ε_{sf}	$K\,Pa\,m^{-2}$	$K\,m^{-1}$	$K\,Pa^{-1}$	$K\,Pa^{-1}$	$K\,Pa^{-1}$	$K\,Pa^{-1}$

where ε_{lh} is the latent heating intensity parameter, ω_* is the vertical motion at the bottom of the latent heating layer, and h_{lh} is the vertical profile of latent heating *divided by pressure*. Consistent with Mak (1994) we let

$$h_{lh}(p) = H(p - 0.4) - H(p - 0.9)$$
$$= \begin{cases} 0 & \text{for} \quad p < 0.4 \quad \text{and} \quad p > 0.9 \\ 1 & \text{for} \quad 0.4 < p < 0.9 \end{cases}, \quad (6)$$

where $p_{lht} = 0.4$ and $p_{lhb} = p_* = 0.9$ are the nondimensional pressure at the top and bottom of the latent heating layer, corresponding to 400 and 900 hPa, respectively. We have also tested other levels for the heating boundaries, which yield qualitatively similar results (not shown).

We use the same latent heating intensity parameter $\varepsilon_{lh} = 12.5$ for all experiments, which corresponds to a heating rate approaching $40 \, \text{K day}^{-1}$ when $\omega \sim 10^{-3} \, \text{hPa s}^{-1}$. This choice is based on the arguments about reasonable heating rates by HS19, where similar heating rates yield qualitatively comparable results. Note that the heating should be viewed as heating anomalies rather than total heating.

c. Parameterization of surface sensible heat fluxes

1) FORMULATIONS MOTIVATED BY TEMPERATURE AND TEMPERATURE ADVECTION

We apply the linearized version of the bulk relation for surface sensible heat fluxes from Monin–Obukhov theory

$$Q_{sf} \propto |\mathbf{v}_s|(\text{SST} - T_s), \quad (7)$$

where $|\mathbf{v}_s|$ is the surface wind speed, SST is the sea surface temperature, and T_s is the temperature of the overlying air. Following Mak (1998), we assume a constant sea surface temperature and define the surface fluxes *divided by pressure* as

$$\hat{Q}_{sf,T} = \varepsilon_{sf} h_{sf}(p) \frac{\partial \hat{\psi}}{\partial p}\Big|_s, \quad (8)$$

where the subscript s denotes a surface value and the impact of horizontal wind speed is incorporated in the intensity parameter ε_{sf}. This formulation does not, however, take into account that surface sensible heat fluxes

are typically located where the meridional temperature advection $v_s(\partial \overline{T}/\partial y) \propto -ik\psi_s\lambda$ is anomalously strong (Boutle et al. 2010). Thus, we introduce an alternative formulation based on meridional wind anomalies:

$$\hat{Q}_{sf,v} = -\varepsilon_{sf} h_{sf}(p) ik\hat{\psi}_s, \quad (9)$$

where the basic-state meridional temperature gradient is incorporated in the intensity parameter ε_{sf}. Note that the dimensional form of the surface flux intensity parameter ε_{sf} has different units in (8) and (9) (see Table 2).

The heating profile for surface fluxes h_{sf} is independent of the flux formulation and given by

$$h_{sf}(p) = H(p - 0.9) = \begin{cases} 0 & \text{for} \quad p < 0.9 \\ 1 & \text{for} \quad p > 0.9 \end{cases}. \quad (10)$$

Note that interior PV anomalies for the given profiles of surface fluxes and latent heating in conjunction with constant S and λ can only exist at the two heating boundaries where $dQ/dp \neq 0$ (see dashed lines relative to the heating profiles in Fig. 1a).

2) FORMULATION MOTIVATED BY SENSITIVITY TO HORIZONTAL LOCATION

In addition to the surface flux formulations above, we introduce a third formulation based on ω_*

$$\hat{Q}_{sf,\omega} = \varepsilon_{sf} h_{sf}(p) \hat{\omega}_*. \quad (11)$$

While this choice is not necessarily based on physical or observational arguments, it has the advantage that we can directly control the relative position between the surface fluxes and the latent heating, independent of potential alterations in the wave structure related to diabatic effects. As low-level upward motion is located near warm-air advection, the surface fluxes based on this formulation are similar to the formulations based on temperature [see (8)] and meridional wind [see (9)] anomalies.

By including an imaginary part in the intensity parameter ε_{sf}, we phase shift $Q_{sf} = \text{Re}\{\hat{Q}_{sf}(p)\exp[i(kx - \sigma t)]\}$ such that downward surface sensible heat fluxes are located upstream ($\text{Im}\{\varepsilon_{sf}\} > 0$) or downstream ($\text{Im}\{\varepsilon_{sf}\} < 0$) of the region of latent heating (see schematic in Fig. 1b for the relative location of the surface fluxes and Table 2 for the numerical value of ε_{sf} for the respective locations).

This allows us to investigate how the relative positioning of surface sensible heat fluxes and latent heating changes the growth rate and the structure of the solution. Although we are shifting the surface fluxes from their typical location relative to the latent heating, such a sensitivity analysis helps us to better understand how alterations in the location of surface fluxes change the relative role of PV anomalies at different vertical levels and hence affect cyclone structure and development.

3) SURFACE FLUX INTENSITY

To ensure a fixed ratio between the maximum intensity of latent heating and surface sensible heat fluxes, i.e., $\max(Q_{lh})/\max(Q_{sf})$, across all experiments, we adjust the surface flux intensity parameter ε_{sf} between experiments accordingly. This is necessary, because changes in the surface flux intensity can cause modifications in the structure that modify the relative strength of the surface fluxes compared to the amount of latent heating. A fixed ratio ensures that the relative intensity of surface fluxes is similar in the different experiments. The ratio is maintained across experiments by varying ε_{sf} in a trial-and-error approach for each of the surface flux formulations.

We tested surface flux intensities that range from zero to intensities 3 times larger than the latent heating rate. As the surface flux intensity is highly dependent on various factors, e.g., the type of cyclone and differences in the sea surface temperature underneath a cyclone, it is difficult to define a universal intensity for the incipient stage of the cyclone. For example, surface sensible heat fluxes from composites along the frontal passage of 10 midlatitude cyclones ranged from about $-30 \, \text{W m}^{-2}$ in the warm sector to about $100 \, \text{W m}^{-2}$ in the cold sector (Persson et al. 2005), while the surface fluxes in a Met Office Unified Model analysis of a mature midlatitude cyclone were significantly stronger and ranged from $-100 \, \text{W m}^{-2}$ in the warm sector to $250 \, \text{W m}^{-2}$ in the cold sector (Sinclair et al. 2010).

Nevertheless, as our results are qualitatively similar for all investigated intensities, we restrict our presentation to heating rates associated with surface fluxes that reach 50% of the latent heating intensity, which corresponds to about $150 \, \text{W m}^{-2}$ when the surface fluxes affect the air column between 1000 and 900 hPa. The corresponding values of ε_{sf} are shown in Table 2 for all surface flux formulations used in this study. Choosing lower/higher intensities would result in a weaker/stronger effect by surface fluxes, but yield qualitatively similar results.

d. Numerical method

We apply a numerical solution technique, where (2)–(4) form an eigenvalue problem that can be solved for the eigenvalue σ and the eigenvectors $\hat{\psi}(p)$ and $\hat{\omega}(p)$ for a given wavenumber k. We use a resolution of 171 vertical levels and calculate solutions for 122 different wavenumbers. Further details can be found in HS19.

e. Normalization of solution

As the nontrivial solution of the eigenvalue problem formed by (2)–(4) contains at least 1 degree of freedom, we cannot compare ψ and ω quantitatively for different experiments and wavelengths (see HS19 for further clarification). Consistent with HS19, we therefore normalize all variables with respect to the domain averaged total eddy energy and argue that such a scaling yields a sound basis for a robust and reliable intercomparison.

We assessed the validity of the QG approximation by comparing the scale of the QG terms in the momentum equations to the ageostrophic advection term. Consistent with HS19, we find that the ageostrophic term is less than 50% of the dominant QG terms when using a dimensional surface velocity of $5 \, \text{m s}^{-1}$ (not shown). We therefore argue that our linear QG framework is suitable to investigate the impact of different types of diabatic heating as long as we stay clear of the intensity threshold discussed by HS19, beyond which the diabatic component of ω dominates over the dynamic component.

3. Impact of surface sensible heat fluxes on cyclone development

We first focus on the surface flux formulations based on T_s in (8) and v_s in (9), followed by the formulation based on ω_* in (11), which includes the sensitivity experiments where we zonally shift the surface fluxes relative to the location of the latent heating. Given the limitations of the linear QG framework, this study mainly focuses on the incipient stage of cyclone development.

a. Parameterizations using T_s and v_s

1) GROWTH RATE

The main modification of the dry Eady growth rate is due to the inclusion of latent heating, with the surface sensible heat fluxes only playing a minor role (Fig. 2). Including only surface sensible heat fluxes based on T_s and v_s, without latent heating, introduces an additional mode with weakly positive growth rates (up to one-third of the maximum Eady growth rate) at shorter wavelengths, while growth rates at long wavelengths are almost unchanged compared to the dry Eady mode (not shown). As in Mak (1998), the growth rates at short wavelengths become similar to the Eady growth rates
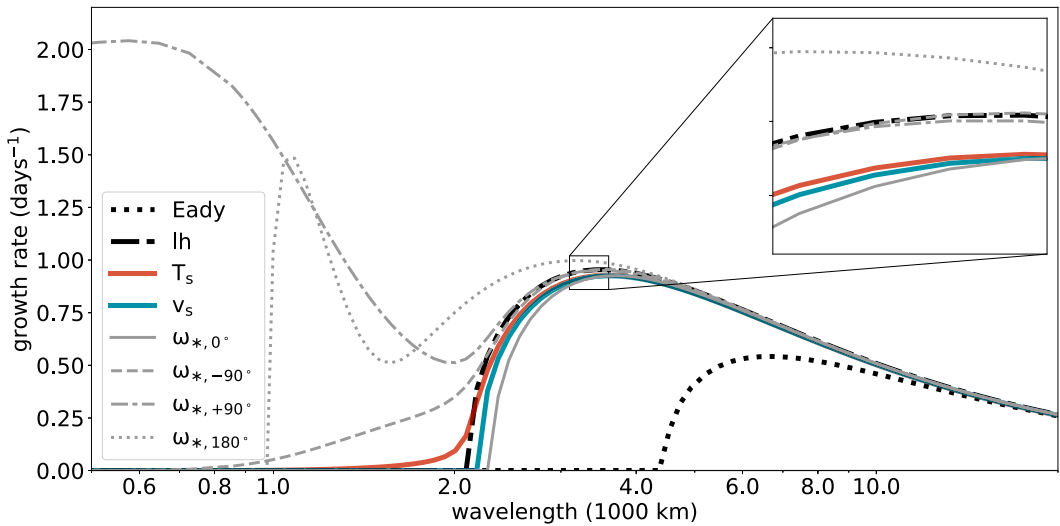
FIG. 2. Growth rate vs wavelength without diabatic heating (Eady, black dotted), with latent heating only (lh, black dot–dashed), as in HS19, and with latent heating and surface sensible heat fluxes, where the surface fluxes are formulated with respect to T_s [(8), red], v_s [(9), blue], or ω_* [(11), gray]. The big box at the upper right shows a zoom-in of the area in the small box. The results for the surface fluxes formulated with respect to ω_* are shown for four different phase shifts. See text for further explanation.

when using Mak's (1998) discontinuous static stability profile (see section 2a). Surface fluxes in conjunction with latent heating reduce baroclinic growth (red and blue lines in Fig. 2), which is consistent with the destruction of eddy available potential energy and low-level baroclinicity by surface sensible heat fluxes.

2) GENERAL STRUCTURE OF THE MOST UNSTABLE MODE

Comparing the structure of temperature (shading), meridional wind (yellow contours), and latent heating (black contours) for the most unstable modes, the solutions with surface fluxes (Figs. 3c,d) bear great resemblance compared to the solution including latent heating only (Fig. 3b). The overall structure of these diabatically influenced solutions even remains qualitatively similar to the dry Eady solution (Fig. 3a). All experiments feature a baroclinically unstable structure, with the meridional wind, and hence the streamfunction, as well as the PV anomalies (position of extrema marked by gray dots), and vertical motion (not shown) tilting westward with height, while the temperature tilts eastward with height. Thus, all solutions are energetically consistent, with warm air ascending poleward.

The cooling from surface sensible heat fluxes (dashed gray contours in Figs. 3c,d) formulated with respect to temperature (meridional wind) is slightly upstream (downstream) of the area of upward motion and is

hence located more or less directly below the area of latent heating.

3) AMPLITUDE AND LOCATION OF POTENTIAL VORTICITY ANOMALIES

Evaluating the terms in the PV equation, (3), we find that the maximum tendency from meridional advection of basic-state PV (rotated plus symbols in Fig. 3) is located less than 90° upstream (downstream) of the upper (lower) positive boundary PV anomaly for all experiments. The positive tendencies contribute to both the exponential growth of the PV anomalies associated with the unstable wave solution as well as to the upstream (downstream) advection of the upper (lower) PV anomaly. This setup counteracts the advection by the basic-state zonal wind and ensures that the boundary PV anomalies are phase locked. Similarly, the maximum *diabatic* tendency (nonrotated plus symbols) at the heating boundaries is located less than 90° upstream (downstream) of the upper (lower) diabatically induced positive PV anomaly, resulting in net amplification and propagation that ensures phase locking.

The cooling associated with the surface fluxes below the layer of latent heating increases the vertical heating gradient and hence, according to the PV equation, (3), the dominance of the diabatic PV anomaly at the bottom of the latent heating layer. At the surface, however, the downward surface fluxes induce a *negative* diabatic
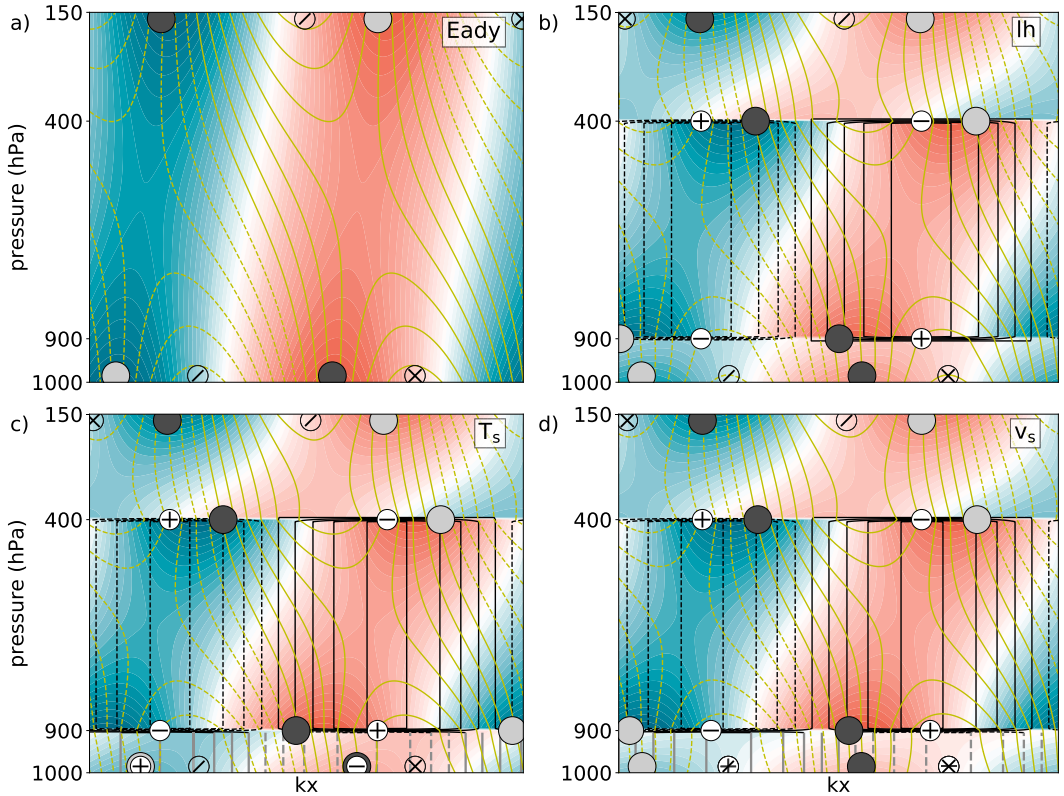
FIG. 3. Temperature (shading), meridional wind (yellow contours), latent heating (black contours), and heating from surface sensible heat fluxes (gray contours) for the most unstable solution (a) without diabatic heating (Eady), (b) with latent heating only (lh), and with latent heating and surface fluxes, where the surface fluxes are either formulated with respect to (c) T_s or (d) v_s. Dark (light) gray dots show position of maximum (minimum) PV anomalies at the four interfaces. Plus and minus symbols show maxima and minima of PV tendency due to either diabatic forcing (nonrotated + and − symbols) or meridional advection of basic-state PV (rotated + and − symbols), respectively, which overlap at the surface in (d).

PV anomaly that suppresses the existing surface PV anomaly. The contribution from the diabatic tendency associated with surface fluxes is therefore decreasing the dominance of the surface PV anomaly relative to the other PV anomalies.

The increasing dominance of the PV anomaly at the bottom of the latent heating layer relative to the surface PV anomaly is depicted in Fig. 4a, where the vertical integral of maximum PV across the bottom of the latent heating layer (red dots) becomes larger than the integral of maximum PV around the surface (black dots) when surface fluxes based on T_s and v_s are included. As a positive PV anomaly is associated with warm air above and cold air below (Hoskins et al. 1985), the decreased dominance of the surface PV anomaly relative to the PV anomaly at the bottom of the latent heating layer is consistent with a weakening

of the positive temperature anomalies below 900 hPa (Figs. 3c,d).

Although the diabatic PV tendency suppresses the surface PV anomaly, the positive contribution from meridional advection of basic-state PV dominates over the diabatic contribution (not shown), resulting in net amplification of the surface PV anomaly. The dominance of meridional advection also ensures that the surface PV anomaly remains phase locked and is advected downstream. This is even the case when the negative diabatic tendency is located downstream of the surface PV, opposing its downstream propagation, as in the formulation based on v_s (Fig. 3d).

4) COMPONENTS OF VERTICAL MOTION

To study the impact of surface fluxes on vertical motion, we split ω into components due to the dynamic and
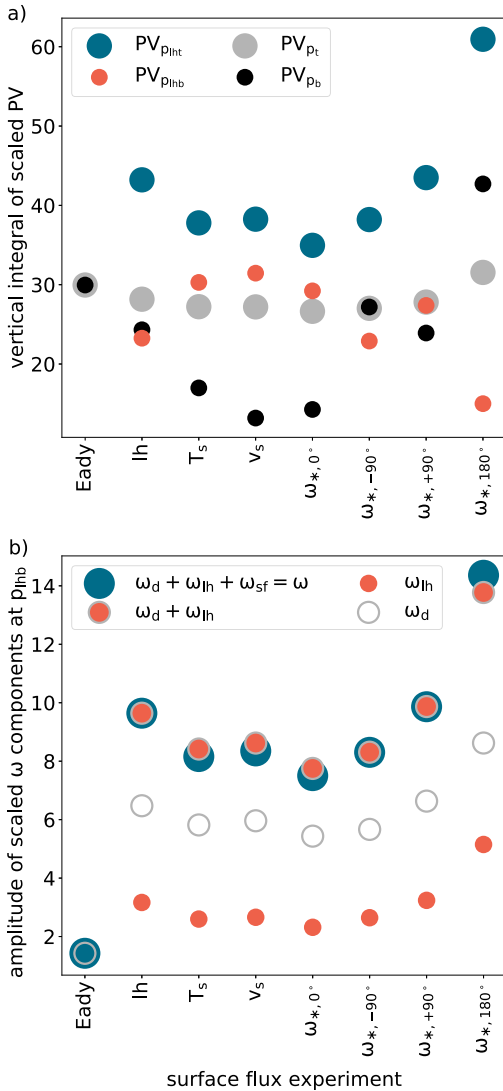
FIG. 4. (a) Vertical integral of the magnitude of scaled PV anomalies (proportional to the magnitude of the PV anomalies) at the model boundaries $p_t = 0.15$ (gray) and $p_b = 1.0$ (black) and the heating interfaces $p_{lht} = 0.4$ (blue) and $p_{lhb} = 0.9$ (red). (b) Amplitude of scaled components of ω_* at the bottom of the latent heating layer, where the subscripts d, lh, and sf denote dynamic, latent heating, and surface flux components, respectively. Results are shown for experiments without diabatic heating (Eady), latent heating only (lh), and for surface fluxes based on T_s, v_s, and ω_* (see text for further explanation). All solutions are scaled with respect to the total energy averaged over the domain.

diabatic forcings on the right-hand side of the ω equation, (2) [see Mak (1994) and HS19 for further details].

Consistent with the low-level cooling by surface sensible heat fluxes around the area of upward motion and below the area of latent heating, the vertical velocity component due to the forcing by surface fluxes reduces the total vertical velocity (cf. blue dots with red dots enclosed by gray circles in Fig. 4b). Even though one has to be careful when comparing absolute vertical velocity magnitudes across experiments (see the normalization issue in section 2e), the weakening of the vertical velocity also causes a reduction in the latent heating component of the vertical velocity (red dots), as the latent heating is parameterized with ω_*. As the dynamic component (gray circles) is enhanced in the presence of latent heating, it also diminishes when surface fluxes are included.

5) ENERGETICS

The effect of surface sensible heat fluxes on the energetics is investigated using the energy framework introduced by Lorenz (1955), where the tendency of domain-averaged eddy available potential energy A_e is defined as

$$\frac{\partial A_e}{\partial t} = C_a + G_e - C_e, \tag{12}$$

with

$$C_a = -\frac{\lambda}{S}\overline{\psi_x \psi_p}, \quad G_e = -\frac{1}{S}\overline{Q\psi_p}, \quad \text{and} \quad C_e = \overline{\omega \psi_p} \tag{13}$$

representing the conversion from basic-state available potential energy to eddy available potential energy (C_a), the generation of eddy available potential energy through diabatic heating (G_e), and the conversion from eddy available potential energy to eddy kinetic energy (C_e), respectively. The bar denotes zonal and vertical averages. We further split the diabatic term into components due to latent heating G_e^{lh} and surface fluxes G_e^{sf} using the respective heating rates Q_{lh} and Q_{sf}. We define changes in G_e^{sf} as direct effects of surface fluxes, while changes in C_a, C_e, and G_e^{lh} due to surface fluxes are referred to as indirect effects.

Comparing the different terms in the energy equation, (12), relative to the net source of eddy available potential energy A_e, we find a weak and negative contribution from G_e^{sf} when surface fluxes are included (Fig. 5). This negative contribution is largest when the surface fluxes are based on surface temperature, because the downward surface fluxes are then more directly collocated with the low-level positive temperature anomalies (Fig. 3c).

The positive contribution from G_e^{lh} reduces when surface fluxes are included. This is consistent with the
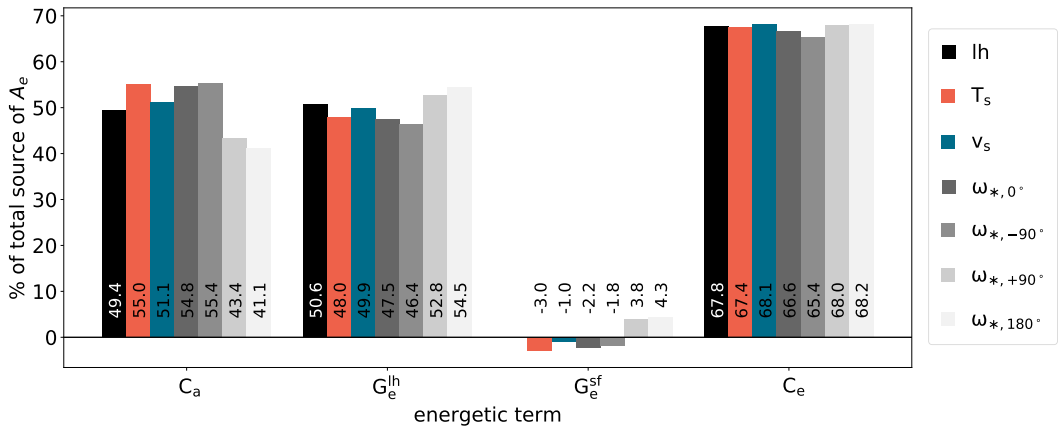
FIG. 5. Relative contributions from the energy terms for experiments with latent heating only (lh, black) and for surface fluxes based on T_s (red), v_s (blue), and ω_* (gray). Each term is scaled with respect to the total source of eddy available potential energy, i.e., $C_a + G_e^{lh} + G_e^{sf}$.

reduced vertical velocity, and hence latent heating, caused by the downward surface fluxes underneath the region of ascent discussed above. Furthermore, as latent heating is associated with enhanced baroclinic growth, a weakening of latent heating by surface fluxes is in agreement with the decrease in growth rate when surface fluxes are added (Fig. 2).

The contribution from C_a increases when surface fluxes are included. This is consistent with a downstream shift of the temperature field in the surface flux layer (Figs. 3c,d), which better collocates the positive temperature anomalies with the northward flow, thereby increasing the meridional heat flux.

The contributions from C_e barely change when surface fluxes are included. This can be explained by the combination of a decrease in C_e due to the reduction in vertical velocity associated with surface fluxes and an increase in C_e due to the downstream shift in the low-level temperature field that better collocates the positive temperature anomalies with upward motion. The net effect on C_e is therefore either weakly negative (when fluxes are based on T_s) or weakly positive (when fluxes are based on v_s).

b. Parameterizations using ω_* including phase shifts

When downward surface sensible heat fluxes are proportional to upward motion at the bottom of the latent heating layer, the location of the surface fluxes and the PV anomalies (Fig. 6a) is between the corresponding locations when surface fluxes are based on temperature (Fig. 3c) and meridional wind (Fig. 3d). The maximum growth rate (gray solid line in Fig. 2) and the amplitude of the PV anomalies as well as the vertical velocity components (Fig. 4) are comparable to the corresponding growth rates and amplitudes for the surface

flux formulations based on surface temperature and meridional wind.

1) SURFACE FLUXES SHIFTED 180°

When we shift upward surface fluxes *in phase* with upward motion, and hence latent heating (cf. black and gray contours in Fig. 6d), the growth rate (dotted gray line in Fig. 2) of the deep mode at long wavelengths ($\gtrsim 2000$ km) is larger than in all other experiments. The increased growth rate is consistent with a strengthening of the vertical velocity by surface fluxes (cf. blue dots with red dots enclosed by gray circles in Fig. 4b), as well as an increase in the generation of eddy available potential energy by latent heating and surface fluxes (lightest gray bars in Fig. 5).

The zonal collocation of upward surface sensible heat fluxes and latent heating reduces the vertical heating gradient at the bottom of the heating layer and hence the dominance of the PV anomaly at this level relative to the other PV anomalies (Fig. 4a). On the other hand, the relative dominance of the surface PV anomaly is enhanced with this surface flux configuration, because the positive diabatic PV tendency (nonrotated plus symbol in Fig. 6d) at the surface is located near the surface PV anomaly. This results in a stronger surface PV anomaly compared to the PV anomaly at the bottom of the latent heating layer, in contrast to the previous surface flux formulations.

2) SURFACE FLUXES SHIFTED ±90°

When surface fluxes are shifted 90° upstream (downstream), upward surface fluxes are located at the leading (trailing) edge of the warm sector (cf. black and gray contours in Figs. 6b,c). For both of these formulations,
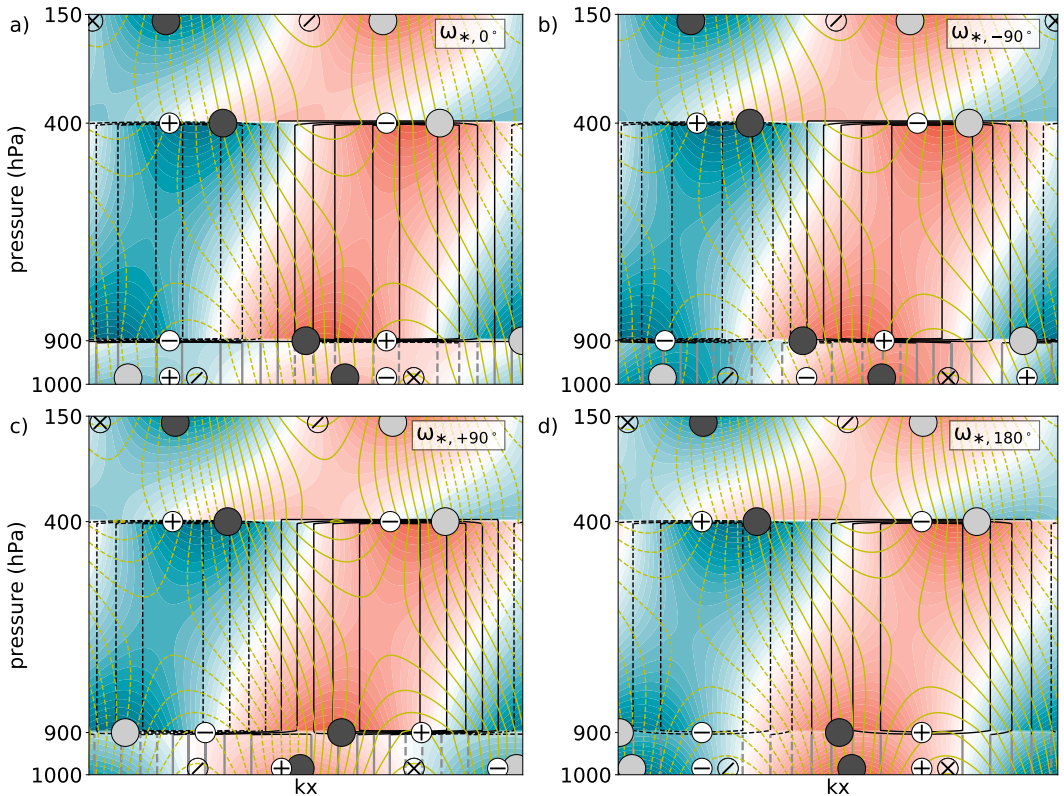
FIG. 6. As in Fig. 3, but for surface fluxes formulated with respect to ω_*. Downward surface fluxes are (a) 0°, (b) −90°, (c) +90°, and (d) 180° out of phase with upward motion.

the maximum growth rate (gray dashed and dot–dashed lines in Fig. 2) is, at long wavelengths, comparable to when no surface fluxes are included (black dashed line), and surface fluxes are neither enhancing nor suppressing the vertical velocity (cf. blue dots with red dots enclosed by gray circles in Fig. 4b).

Despite the similar growth rates and vertical velocities, these surface flux formulations are associated with a different low-level structure of temperature and PV (Figs. 6b,c). When the downward surface fluxes are shifted *upstream* of the latent heating, the surface fluxes are less out of phase with temperature compared to when the downward fluxes are located directly below the area of latent heating (Figs. 6a,b). The negative contribution from $G_e^{\rm sf}$ is therefore slightly weaker (Fig. 5). Concurrently, the low-level temperature anomalies become stronger, in accordance with a slightly larger contribution from C_a. The increase in $G_e^{\rm sf}$ and C_a is associated with a slightly weaker contribution from $G_e^{\rm lh}$ and C_e relative to the net source of A_e.

In contrast to the upstream shift of surface fluxes, a *downstream* shift results in an upstream displacement of the low-level temperature field, such that warm air collocates with heating from the surface fluxes (Fig. 6c). The contribution from $G_e^{\rm sf}$ is therefore positive (Fig. 5). Concurrently, the shift in temperature results in a reduced collocation between temperature and meridional wind at low levels, yielding a decrease in C_a and hence A_e. Thus, the decrease in C_a is associated with an increase in the contribution from $G_e^{\rm lh}$ and C_e relative to the net source of A_e.

Consistent with the upstream (downstream) shift in surface fluxes, there is an upstream (downstream) shift in the maximum vertical gradient in diabatic heating and hence the PV anomaly at the bottom of the latent heating layer (gray dots in Figs. 6a–c). This displacement results in a less ideal westward tilt between the diabatically induced PV anomalies and a weaker dominance of the PV anomaly at the bottom of the latent heating layer relative to the other PV anomalies (Fig. 4a).

At the surface, the *upstream* shift in surface fluxes shifts the negative diabatic PV tendency (nonrotated symbols in Fig. 6) upstream and further away from the surface PV anomaly compared to when the downward surface fluxes are located directly below the area of latent heating. With the negative impact from the diabatic PV tendency being reduced, the surface PV anomaly becomes more dominant relative to the other PV anomalies (Fig. 4a).

As mentioned above, the *downstream* shift of surface fluxes is associated with an upstream shift in temperature, which is per definition also shifting the surface PV anomaly upstream (Hoskins et al. 1985). The surface PV anomaly is now farther away from the positive PV tendency associated with meridional advection (rotated symbols in Fig. 6), but almost entirely in phase with the diabatic PV tendency, which is in contrast to the other surface flux formulations. The positive contribution from the diabatic PV tendency strengthens the relative dominance of the surface PV anomaly compared to when the downward surface fluxes are located directly below the area of latent heating (Fig. 4a).

The upstream (downstream) displacement of the PV anomaly at the surface (bottom of the latent heating layer) associated with the downstream shift of the surface fluxes results in an eastward tilt with height between the low-level PV anomalies (Fig. 6c). Although an eastward tilt is not beneficial for baroclinic instability, both low-level PV anomalies remain phase locked with similar magnitudes (cf. red and black dots in Fig. 4a). This is most likely due to a strong impact of the upper-level PV anomaly on the surface PV anomaly. These anomalies feature the typical westward tilt with height and thereby favor baroclinic development.

3) ADDITIONAL MODES

Additional unstable modes exist for two of the phase-shifted surface flux formulations at wavelengths shorter than 2000 km (dotted and dot–dashed lines in Fig. 2). However, we argue that these modes are unphysical, because the dynamic component of the vertical velocity is much smaller than its diabatic component (not shown), which indicates that these solutions are not reasonable for typical midlatitude cyclones (HS19). With a horizontal scale in the meso-α range, we also argue that these modes are probably too small to be reasonably resolved in the QG framework at hand. Nevertheless, as this is an idealized study that aims to broaden our understanding of moist baroclinic modes, we briefly discuss and contextualize these modes below.

The structure of the unstable mode corresponding to the $\omega_{*,180°}$ experiment at around 1000-km wavelength

is mainly around the top of the latent heating layer and does not feature any surface cyclone, whereas the structure corresponding to the $\omega_{*,+90°}$ experiment at around 600-km wavelength is shallow and mainly within the surface flux layer, where it tilts *eastward* with height (not shown). Neither of these additional modes bear resemblance to real cyclones nor to the additional mode at short wavelengths presented in the related surface flux study by Mak (1998), where the structure is tilting *westward* with height in the surface flux layer.

The absence of Mak's (1998) low-level mode is related to the inclusion of latent heating and the lack of a vertically varying static stability. As explained in section 2a, we argue that the static stability profile presented by Mak (1998) is not representative for this study when latent heating is included. Consequently, we do not recover Mak's (1998) low-level mode.

While Mak (1998) argued that his low-level mode resembles the structure of polar lows, HS19 questioned if such a low-level mode is physical, as the interacting PV anomalies are situated at the bottom and top of the mixed boundary layer, rendering their interactions questionable. To further test the model's capability to represent polar lows, we conducted additional experiments with a more representative polar low environment, where the tropopause was lowered from 150 to 500 hPa and the Coriolis parameter f was increased from 1.0 to 1.4 (corresponding to a latitude of 74°N). Accordingly, the top of the latent heating layer was also lowered from 400 to 600 hPa. The main outcome is that the growth rates increase and shift to shorter wavelengths mainly around 1000–2000 km (not shown). These modifications are mainly due to the increase in Coriolis parameter and to the shallower latent heating layer, with the lowering of the tropopause playing a minor role. The corresponding structures are similar to the original structures in Figs. 3 and 6, though the lower tropopause consistently makes the deep modes shallower (not shown) and thereby remarkably similar to the structure of the idealized polar lows in Terpstra et al. (2015, their Fig. 5b). This confirms the hypothesis of Terpstra et al. (2015) that the development of polar lows resembles that of moist midlatitude cyclones with a lowered tropopause, alongside potential modifications by surface fluxes.

4. Impact of surface latent heat fluxes and moisture supply

While we are able to directly include the role of surface sensible heat fluxes in our model, we investigate the impact of surface latent heat fluxes indirectly by keeping ε_{sf} the same as in Table 2 while increasing the latent heating intensity parameter ε_{lh} from its default value of

12.5 to the intensity needed to match the growth rate of the experiment only including latent heating (Fig. 2). The resulting change of ε_{lh} is then inserted into (5) to estimate the corresponding average dimensional change in latent heating $\Delta\overline{Q}$ for a vertical velocity scaling of $10^{-3}\,\text{hPa}\,\text{s}^{-1}$ (Table 3). Assuming pseudoadiabatic ascent, the corresponding additional water vapor supply equals the average change in saturation humidity mixing ratio $\overline{q}_s$

$$\frac{d\overline{q}_s}{dt} = -\frac{c_p}{L}\Delta\overline{Q}, \qquad (14)$$

where c_p is the heat capacity at constant pressure and L is the latent heat of condensation. The additional water supply can then be used to estimate the required sustained surface latent heat flux to alter the air parcels accordingly:

$$Q_{lf} = L\frac{d\overline{q}_s}{dt}\frac{p_{lht} - p_{lhb}}{g} = -c_p\frac{p_{lht} - p_{lhb}}{g}\Delta\overline{Q}, \qquad (15)$$

where $(p_{lhb} - p_{lht})/g$ represents the mass of the heating layer, with g being the gravitational constant.

For surface flux formulations based on surface temperature, meridional wind, and vertical motion at the bottom of the latent heating layer, where the maximum growth rate reduces compared to when no surface fluxes are included, the estimated intensity of sustained surface latent heat fluxes required to overcome the detrimental effects range from 36 to $43\,\text{W}\,\text{m}^{-2}$ (Table 3). These values are small compared to the passage of midlatitude cyclones, where surface latent heat fluxes range from 30 to $140\,\text{W}\,\text{m}^{-2}$ in the warm sector and even reach up to $200\,\text{W}\,\text{m}^{-2}$ further ahead of the warm sector (Persson et al. 2005). We therefore argue that the moisture input from surface latent heat fluxes into the warm conveyor belt increases the latent heat release sufficiently to compensate for the detrimental effects of surface sensible heat fluxes, such that the net effect of surface sensible and latent heat fluxes is beneficial for cyclone development.

5. Concluding remarks

We included surface sensible heat fluxes in conjunction with moderate latent heating in the linear QG Eady (1949) model to investigate the direct and indirect effects of surface fluxes on the incipient stage of midlatitude cyclone development, where direct and indirect are defined as either directly influencing the diabatic generation of eddy available potential energy or related to indirect changes in the circulation and latent heating that affect the energetics, respectively. We find that

TABLE 3. Estimated changes of the latent heating intensity parameter (ε_{lh}) and latent heating (Q_{lh}) as well as sustained surface latent heat fluxes (SSLH) necessary to overcome the detrimental effects of surface sensible heat fluxes for the deep modes at long wavelengths in Fig. 2.

Surface flux parameterization	T_s	v_s	$\omega_{*,0^\circ}$
$\Delta\varepsilon_{lh}$ (nondimensional)	0.31	0.34	0.37
ΔQ_{lh} (K day^{-1})	0.61	0.67	0.72
SSLH (W m^{-2})	36	39	43

changes in the growth rate and structure due to surface sensible heat fluxes are rather small compared to changes related to latent heating. Growth rates reduce when downward surface sensible heat fluxes are located around warm surface air, poleward surface winds, or low-level ascent. This is expected from the decrease in low-level baroclinicity, where surface sensible heat fluxes cool (heat) the warm (cold) sector. The surface fluxes also yield a weakening of vertical motion and thus latent heat release, which also leads to a reduction in growth rate.

We tested different parameterizations to represent surface sensible heat fluxes and found that the results are more sensitive to the actual location of the surface sensible heat fluxes than to the type of surface flux parameterization. When upward surface sensible heat fluxes are located directly below the layer of latent heating, the growth rate increases. However, when the surface sensible heat fluxes are located one-quarter wavelength up- or downstream from the region of latent heating, the maximum growth rate is almost unaffected compared to the experiment with latent heating only.

The structure of the most unstable mode for all experiments is generally consistent with the energetics of baroclinic instability, featuring a QG streamfunction, meridional wind, PV anomalies, and vertical motion tilting westward with height as well as a temperature field tilting eastward with height. Surface sensible heat fluxes modify the relative role of the low-level PV anomalies by shifting the low-level temperature structure. When downward surface sensible heat fluxes are located below the equivalent of the warm conveyor belt, the diabatically induced PV anomaly at the bottom of the latent heating layer becomes more dominant than the PV anomalies at the model boundaries. This is consistent with enhanced vertical heating gradients at the interface between the layers of latent heating and surface fluxes.

In contrast, when *upward* surface sensible heat fluxes are located below the area of latent heating, the diabatic PV anomaly at the interface between the layers of latent heating and surface fluxes becomes the least dominant PV anomaly, while the surface PV anomaly becomes

more dominant due to a positive diabatic PV tendency at the surface. Moreover, when downward surface sensible heat fluxes are located upstream or downstream of the area of latent heating, the diabatically induced PV anomaly at the bottom of the latent heating layer is shifted accordingly, resulting in a weaker or stronger westward tilt with height relative to the diabatic PV anomaly at the top of the layer of latent heating. Such a setup is less ideal for baroclinic development. Concurrently, the diabatic PV tendency around the surface PV anomaly is less negative—or even positive—compared to when downward surface sensible heat fluxes are located below the layer of latent heating. Consequently, the importance of the surface PV anomaly is similar to the diabatic PV anomaly at the bottom of the latent heating layer.

When downward surface sensible heat fluxes are located near the warm conveyor belt, the collocation of warm air with northward flow is improved, resulting in a positive impact on the conversion from basic-state available potential energy to eddy available potential energy. In contrast, the direct and indirect effects on the diabatic generation of eddy available potential energy are detrimental, where the indirect effect is related to a reduction in vertical motion and hence latent heating. Despite the reduction in vertical motion, the conversion from eddy available potential energy to eddy kinetic energy is, however, not significantly affected by surface fluxes.

The impact on the energetics described in the previous paragraph is qualitatively identical when surface sensible heat fluxes are shifted a quarter wavelength upstream. However, when the downward surface sensible heat fluxes are located one-quarter wavelength downstream, as well as when they are completely out of phase with latent heating, the qualitative impact on the energetics reverses, with a positive impact on the diabatic generation of eddy available potential energy and a negative impact on the conversion from basic-state available potential energy to eddy available potential energy. Hence, while the upstream and downstream shift of surface fluxes may result in similar growth rates, the low-level structure and energetics are quite different, which is potentially important for other aspects of the development, such as nonlinear processes. In general, our surface flux formulations yield a reduced strength in vertical motion at the bottom of the latent heating layer, except when the surface fluxes are reversed or shifted downstream, in which case the vertical motion at the bottom of the latent heating layer strengthens. However, similar to the other formulations, the modification of vertical motion does not significantly affect the conversion from eddy available potential energy to eddy kinetic energy.

When we simultaneously lower the tropopause, increase the Coriolis parameter, and make the latent heating layer shallower to better represent polar environments, our results are qualitative similar, though growth rates increase and unstable modes shift toward shorter wavelengths. Furthermore, consistent with a shallower troposphere, the structure of the unstable modes becomes shallower and thereby more similar to polar lows, supporting earlier findings that polar lows grow through moist baroclinic instability.

While our model framework only allows for a direct investigation of surface sensible heat fluxes, estimated modifications in moisture supply related to changes in latent heating indicate that the detrimental effects of the surface sensible heat fluxes are easily compensated by the indirect effect of providing additional moisture into the warm conveyor belt through surface latent heat fluxes. This finding further highlights the importance of previously identified moisture pathways into the warm conveyor belt (Boutle et al. 2010; Pfahl et al. 2014; Dacre et al. 2019), whereas local surface fluxes in the cold sector energetically do not appear to be a viable option. The moisture pathways into the warm conveyor belt and their connection to local and remote surface fluxes should thus be studied further using more complex models that are able to represent peripheral moisture sources from preceding cyclones or from moist air masses originating in the subtropics.

REFERENCES

Atlas, R., 1987: The role of oceanic fluxes and initial data in the numerical prediction of an intense coastal storm. *Dyn. Atmos. Oceans*, **10**, 359–388, https://doi.org/10.1016/0377-0265(87)90025-X.

Balasubramanian, G., and M. Yau, 1996: The life cycle of a simulated marine cyclone: Energetics and PV diagnostics. *J. Atmos. Sci.*, **53**, 639–653, https://doi.org/10.1175/1520-0469(1996)053<0639:TLCOAS>2.0.CO;2.

Booth, J. F., L. Thompson, J. Patoux, and K. A. Kelly, 2012: Sensitivity of midlatitude storm intensification to perturbations in the sea surface temperature near the Gulf Stream. *Mon. Wea. Rev.*, **140**, 1241–1256, https://doi.org/10.1175/MWR-D-11-00195.1.

Bosart, L. F., 1981: The Presidents' Day snowstorm of 18–19 February 1979: A subsynoptic-scale event. *Mon. Wea. Rev.*, **109**, 1542–1566, https://doi.org/10.1175/1520-0493(1981)109<1542:TPDSOF>2.0.CO;2.

Boutle, I., R. Beare, S. Belcher, A. Brown, and R. Plant, 2010: The moist boundary layer under a mid-latitude weather system.

Bound.-Layer Meteor., **134**, 367–386, https://doi.org/10.1007/s10546-009-9452-9.

Branscome, L. E., W. J. Gutowski Jr., and D. A. Stewart, 1989: Effect of surface fluxes on the nonlinear development of baroclinic waves. *J. Atmos. Sci.*, **46**, 460–475, https://doi.org/10.1175/1520-0469(1989)046<0460:EOSFOT>2.0.CO;2.

Browning, K. A., 1990: Organization of clouds and precipitation in extratropical cyclones. *Extratropical Cyclones: Erik Palmén Memorial Volume*, C. W. Newton and E. O. Holopainen, Eds., Amer. Meteor. Soc., 129–153.

Carrera, M. L., J. R. Gyakum, and D.-L. Zhang, 1999: A numerical case study of secondary marine cyclogenesis sensitivity to initial error and varying physical processes. *Mon. Wea. Rev.*, **127**, 641–660, https://doi.org/10.1175/1520-0493(1999)127<0641:ANCSOS>2.0.CO;2.

Craig, G., and H.-R. Cho, 1988: Cumulus heating and CISK in the extratropical atmosphere. Part I: Polar lows and comma clouds. *J. Atmos. Sci.*, **45**, 2622–2640, https://doi.org/10.1175/1520-0469(1988)045<2622:CHACIT>2.0.CO;2.

Dacre, H. F., O. Martinez-Alvarado, and C. O. Mbengue, 2019: Linking atmospheric rivers and warm conveyor belt airflows. *J. Hydrometeor.*, **20**, 1183–1196, https://doi.org/10.1175/JHM-D-18-0175.1.

Danard, M. B., and G. E. Ellenton, 1980: Physical influences on East Coast cyclogenesis. *Atmos.–Ocean*, **18**, 65–82, https://doi.org/10.1080/07055900.1980.9649078.

Eady, E. T., 1949: Long-waves and cyclone waves. *Tellus*, **1** (3), 33–52, https://doi.org/10.3402/tellusa.v1i3.8507.

Fleagle, R. G., and W. A. Nuss, 1985: The distribution of surface fluxes and boundary layer divergence in midlatitude ocean storms. *J. Atmos. Sci.*, **42**, 784–799, https://doi.org/10.1175/1520-0469(1985)042<0784:TDOSFA>2.0.CO;2.

Gutowski, W. J., Jr., and W. Jiang, 1998: Surface-flux regulation of the coupling between cumulus convection and baroclinic waves. *J. Atmos. Sci.*, **55**, 940–953, https://doi.org/10.1175/1520-0469(1998)055<0940:SFROTC>2.0.CO;2.

Gyakum, J. R., and R. E. Danielson, 2000: Analysis of meteorological precursors to ordinary and explosive cyclogenesis in the western North Pacific. *Mon. Wea. Rev.*, **128**, 851–863, https://doi.org/10.1175/1520-0493(2000)128<0851:AOMPTO>2.0.CO;2.

Haltiner, G., 1967: The effects of sensible heat exchange on the dynamics of baroclinic waves. *Tellus*, **19**, 183–198, https://doi.org/10.1111/j.2153-3490.1967.tb01472.x.

Haualand, K. F., and T. Spengler, 2019: How does latent cooling affect baroclinic development in an idealized framework? *J. Atmos. Sci.*, **76**, 2701–2714, https://doi.org/10.1175/JAS-D-18-0372.1.

Hirata, H., R. Kawamura, M. Nonaka, and K. Tsuboki, 2019: Significant impact of heat supply from the Gulf Stream on a "superbomb" cyclone in January 2018. *Geophys. Res. Lett.*, **46**, 7718–7725, https://doi.org/10.1029/2019GL082995.

Hoskins, B., M. McIntyre, and W. Robertson, 1985: On the use and significance of isentropic potential vorticity maps. *Quart. J. Roy. Meteor. Soc.*, **111**, 877–946, https://doi.org/10.1002/qj.49711147002.

Jiang, W., and W. J. Gutowski, 2000: Moist baroclinic instability in the presence of surface–atmosphere coupling. *J. Atmos. Sci.*, **57**, 2923–2935, https://doi.org/10.1175/1520-0469(2000)057<2923:MBIITP>2.0.CO;2.

Keeley, S., R. Sutton, and L. Shaffrey, 2012: The impact of North Atlantic sea surface temperature errors on the simulation of North Atlantic European region climate. *Quart. J. Roy. Meteor. Soc.*, **138**, 1774–1783, https://doi.org/10.1002/qj.1912.

Kuo, Y.-H., and R. J. Reed, 1988: Numerical simulation of an explosively deepening cyclone in the eastern Pacific. *Mon. Wea. Rev.*, **116**, 2081–2105, https://doi.org/10.1175/1520-0493(1988)116<2081:NSOAED>2.0.CO;2.

——, and S. Low-Nam, 1990: Prediction of nine explosive cyclones over the western Atlantic Ocean with a regional model. *Mon. Wea. Rev.*, **118**, 3–25, https://doi.org/10.1175/1520-0493(1990)118<0003:PONECO>2.0.CO;2.

——, R. J. Reed, and S. Low-Nam, 1991a: Effects of surface energy fluxes during the early development and rapid intensification stages of seven explosive cyclones in the western Atlantic. *Mon. Wea. Rev.*, **119**, 457–476, https://doi.org/10.1175/1520-0493(1991)119<0457:EOSEFD>2.0.CO;2.

——, M. Shapiro, and E. G. Donall, 1991b: The interaction between baroclinic and diabatic processes in a numerical simulation of a rapidly intensifying extratropical marine cyclone. *Mon. Wea. Rev.*, **119**, 368–384, https://doi.org/10.1175/1520-0493(1991)119<0368:TIBBAD>2.0.CO;2.

Langland, R., R. Elsberry, and R. Errico, 1995: Evaluation of physical processes in an idealized extratropical cyclone using adjoint sensitivity. *Quart. J. Roy. Meteor. Soc.*, **121**, 1349–1386, https://doi.org/10.1002/qj.49712152608.

Lee, R., T. Woollings, and B. Hoskins, 2018: Impact of Gulf Stream SST biases on the global atmospheric circulation. *Climate Dyn.*, **51**, 3369–3387, https://doi.org/10.1007/s00382-018-4083-9.

Lorenz, E. N., 1955: Available potential energy and the maintenance of the general circulation. *Tellus*, **7**, 157–167, https://doi.org/10.3402/tellusa.v7i2.8796.

Mailhot, J., and C. Chouinard, 1989: Numerical forecasts of explosive winter storms: Sensitivity experiments with a meso-α scale model. *Mon. Wea. Rev.*, **117**, 1311–1343, https://doi.org/10.1175/1520-0493(1989)117<1311:NFOEWS>2.0.CO;2.

Mak, M., 1994: Cyclogenesis in a conditionally unstable moist baroclinic atmosphere. *Tellus*, **46**, 14–33, https://doi.org/10.3402/tellusa.v46i1.15424.

——, 1998: Influence of surface sensible heat flux on incipient marine cyclogenesis. *J. Atmos. Sci.*, **55**, 820–834, https://doi.org/10.1175/1520-0469(1998)055<0820:IOSSHF>2.0.CO;2.

Mullen, S. L., and D. P. Baumhefner, 1988: Sensitivity of numerical simulations of explosive oceanic cyclogenesis to changes in physical parameterizations. *Mon. Wea. Rev.*, **116**, 2289–2329, https://doi.org/10.1175/1520-0493(1988)116<2289:SONSOE>2.0.CO;2.

Neiman, P. J., and M. Shapiro, 1993: The life cycle of an extratropical cyclone. Part I: Frontal-cyclone evolution and thermodynamic air–sea interaction. *Mon. Wea. Rev.*, **121**, 2153–2176, https://doi.org/10.1175/1520-0493(1993)121<2153:TLCOAE>2.0.CO;2.

Nuss, W. A., and R. A. Anthes, 1987: A numerical investigation of low-level processes in rapid cyclogenesis. *Mon. Wea. Rev.*, **115**, 2728–2743, https://doi.org/10.1175/1520-0493(1987)115<2728:ANIOLL>2.0.CO;2.

Persson, P. O. G., J. Hare, C. Fairall, and W. Otto, 2005: Air–sea interaction processes in warm and cold sectors of extratropical cyclonic storms observed during FASTEX. *Quart. J. Roy. Meteor. Soc.*, **131**, 877–912, https://doi.org/10.1256/qj.03.181.

Pfahl, S., E. Madonna, M. Boettcher, H. Joos, and H. Wernli, 2014: Warm conveyor belts in the ERA-Interim dataset (1979-2010). Part II: Moisture origin and relevance for precipitation. *J. Climate*, **27**, 27–40, https://doi.org/10.1175/JCLI-D-13-00223.1.

Reed, R. J., and M. D. Albright, 1986: A case study of explosive cyclogenesis in the eastern Pacific. *Mon. Wea. Rev.*, **114**, 2297–2319, https://doi.org/10.1175/1520-0493(1986)114<2297:ACSOEC>2.0.CO;2.

Schäfler, A., and Coauthors, 2018: The North Atlantic Waveguide and Downstream Impact Experiment. *Bull. Amer. Meteor. Soc.*, **99**, 1607–1637, https://doi.org/10.1175/BAMS-D-17-0003.1.

Sinclair, V. A., S. E. Belcher, and S. L. Gray, 2010: Synoptic controls on boundary layer characteristics. *Bound.-Layer Meteor.*, **134**, 387–409, https://doi.org/10.1007/s10546-009-9455-6.

Terpstra, A., T. Spengler, and R. W. Moore, 2015: Idealised simulations of polar low development in an Arctic moist baroclinic environment. *Quart. J. Roy. Meteor. Soc.*, **141**, 1987–1996, https://doi.org/10.1002/qj.2507.

Uccellini, L. W., R. A. Petersen, K. F. Brill, P. J. Kocin, and J. J. Tuccillo, 1987: Synergistic interactions between an upper-level jet streak and diabatic processes that influence the development of a low-level jet and a secondary coastal cyclone. *Mon. Wea. Rev.*, **115**, 2227–2261, https://doi.org/10.1175/1520-0493(1987)115<2227:SIBAUL>2.0.CO;2.

Zhang, D.-L., E. Radeva, and J. Gyakum, 1999: A family of frontal cyclones over the western Atlantic Ocean. Part II: Parameter studies. *Mon. Wea. Rev.*, **127**, 1745–1760, https://doi.org/10.1175/1520-0493(1999)127<1745:AFOFCO>2.0.CO;2.

Zhang, Y., and P. H. Stone, 2011: Baroclinic adjustment in an atmosphere–ocean thermally coupled model: The role of the boundary layer processes. *J. Atmos. Sci.*, **68**, 2710–2730, https://doi.org/10.1175/JAS-D-11-078.1.

Paper III

Relative importance of tropopause structure and diabatic heating for baroclinic instability

Haualand, K. F. and Spengler, T.

Relative importance of tropopause structure and diabatic heating for baroclinic instability

Kristine Flacké Haualand[1] and Thomas Spengler[1]

[1]Geophysical Institute, University of Bergen, and Bjerknes Centre for Climate Research, Bergen, Norway

Correspondence: Kristine Flacké Haualand (Kristine.Haualand@uib.no)

Abstract. Misrepresentations of wind shear and stratification around the tropopause in numerical weather prediction models can lead to errors in potential vorticity gradients with repercussions for Rossby wave propagation and baroclinic instability. Using a diabatic extension of the linear quasi-geostrophic Eady model featuring a tropopause, we investigate the influence of such discrepancies on baroclinic instability by varying tropopause sharpness and altitude as well as wind shear and stratification in the lower stratosphere, which can be associated with model or data assimilation errors or a downward extension of a weakened polar vortex. We find that baroclinic development is less sensitive to tropopause sharpness than to modifications in wind shear and stratification in the lower stratosphere, where the latter are associated with a net change in the vertical integral of the horizontal potential vorticity gradient across the tropopause. To further quantify the relevance of these sensitivities, we compare these findings to the impact of including mid-tropospheric latent heating. For representative modifications of wind shear, stratification, and latent heating intensity, the sensitivity of baroclinic instability to tropopause structure is significantly less than that to latent heating of different intensities. These findings indicate that tropopause sharpness is less important for baroclinic development than previously anticipated and that latent heating and the structure in the lower stratosphere play a more crucial role, with latent heating being the dominant factor.

1 Introduction

The tropopause is characterised by sharp vertical transitions in vertical wind shear and stratification, resulting in large horizontal and vertical gradients of potential vorticity (PV) (e.g., Birner et al., 2006; Schäfler et al., 2020). These PV gradients act as wave guides for Rossby waves and are crucial for their propagation (see review by Wirth et al., 2018, and references therein). Hence, the common notion that tropopause sharpness must be important for midlatitude weather and its predictability (e.g., Schäfler et al., 2018). In addition to the potentially important impact from the structure of the tropopause, baroclinic development is also greatly influenced by diabatic heating associated with cloud condensation (e.g., Manabe, 1956; Craig and Cho, 1988; Snyder and Lindzen, 1991). As diabatic heating strongly influences the horizontal scale and intensification of cyclones (e.g., Emanuel et al., 1987; Balasubramanian and Yau, 1996; Moore and Montgomery, 2004), its misrepresentation is a common source for errors in midlatitude weather and cyclone forecasting (Beare et al., 2003; Gray et al., 2014; Martínez-Alvarado et al., 2016). While the effect of diabatic heating on baroclinic development is relatively well known, few studies have investigated the

25 impact of tropopause sharpness on baroclinic development. Here, we quantify and contrast these two contributions to baroclinic instability using an idealised framework.

The initialisation of the tropopause in weather and climate prediction models is based on a sparse observational network of satellites and radiosondes, resulting in large estimates of analysis errors and analysis error variance in the tropopause regions (Hamill et al., 2003; Hakim, 2005). Given this challenge in constraining the atmospheric state near the tropopause, it is difficult

30 to evaluate how potential errors influence the initial state in weather forecast models and thereby the overall predictability of midlatitude weather. In addition to errors related to observations, the representation of tropopause sharpness is further modified by data assimilation techniques (Birner et al., 2006; Pilch Kedzierski et al., 2016). For example, investigating the representation of the tropopause inversion layer, Birner et al. (2006) concluded that data assimilation smoothed the analysis of the sharp vertical temperature gradient just above the tropopause. In contrast, Pilch Kedzierski et al. (2016) found that data

35 assimilation improved the representation of these sharp gradients, although the gradients were still too smooth and their location displaced from the actual tropopause compared to satellite and radiosonde observations. Given the unclear contributions from data assimilation and observational errors, it remains uncertain how well tropopause sharpness is represented in model analysis and especially how important such a representation is for baroclinic development.

Even if these sharp structures were well represented at the initial state, forecast errors at the tropopause have been shown to

40 quickly develop in a few days (e.g., Dirren et al., 2003; Hakim, 2005; Gray et al., 2014; Saffin et al., 2017). Using medium-range forecasts from three operational weather forecast centres, Gray et al. (2014) showed that PV gradients at the tropopause were smoothed with forecast lead time due to horizontal resolution and numerical dissipation. One can expect such a smoothing to dominate even more in global climate prediction models due to the coarser resolution. It is, however, unclear how much these forecast errors near the tropopause contribute to forecast errors for midlatitude cyclones.

45 Another challenge influencing the forecast skill related to structures near the tropopause is the chosen altitude of the top of the atmospheric model, because it affects how artefacts from the upper boundary imprint themselves at the tropopause. Lifting the model lid has been shown to significantly improve the medium-range forecast of the stratosphere (Charron, 2012) as well as climate predictions on intraseasonal to interannual time scales (Marshall and Scaife, 2010; Hardiman et al., 2012; Charlton-Perez et al., 2013; Osprey et al., 2013; Butler et al., 2016; Kawatani et al., 2019). However, no studies have investigated the

50 direct impact of the model lid on tropopause sharpness. With the discrepancies related to a low model lid potentially affecting the representation of the tropopause, it is valuable to understand how sensitive baroclinic development is to such modifications of the tropopause.

While the modelling challenges related to the model lid, model resolution, data assimilation techniques, and observations typically lead to a smoothing of the sharp PV gradients around the tropopause, they may also contribute to misrepresentations

55 of wind (Schäfler et al., 2020) and temperature (Pilch Kedzierski et al., 2016) in the stratosphere that result in further deviations in the stratospheric PV gradients. Even if such deviations were small, a change in the difference in wind shear and stratification across a finite tropopause alters the vertical integral of the horizontal PV gradient. For example, increasing the wind in the lower stratosphere, which alters the vertical integral of the horizontal PV gradient by weakening the amplitude of the negative wind shear above the tropopause, influences the nonlinear decay in baroclinic lifecycles (Rupp and Birner, 2021). The authors

also indicated that the linear growth phase of the development might respond more to changes in the stratospheric wind if the horizontal PV gradients were further modified. As no previous studies have directly investigated how modifications in the vertical integral of the horizontal PV gradient influences baroclinic development, the importance of preserving the vertical integral of PV gradients remains unclear.

While tropopause sharpness is mainly related to vertical changes *across* the tropopause, misrepresentations of either stratification or vertical wind shear may also lead to implicit modifications of the altitude of the tropopause itself. Such fluctuations of the tropopause are associated with enhanced analysis and forecast errors (Hakim, 2005) and are often induced by baroclinic waves through vertical and meridional heat transport (Egger, 1995). While some studies argue that baroclinic instability is sensitive to the level of the tropopause (Blumen, 1979; Harnik and Lindzen, 1998), Müller (1991) found that the vertical distance between the waves at the tropopause and at the surface is not very important for baroclinic development. Thus, the net effect on baroclinic instability by altering stratification and wind shear in ways that affect tropopause altitude remains unclear.

To evaluate the relative importance of the various aspects of tropopause structure and diabatic heating for baroclinic instability, we use a moist extension of the linear quasi-geostrophic (QG) Eady (1949) model where we vary wind shear and stratification across the tropopause using different heating intensities. While previous idealised studies focused on the impact of abrupt environmental changes across the tropopause (e.g., Blumen, 1979; Müller, 1991; Wittman et al., 2007) and how sharp and smooth transitions across the tropopause affected neutral modes and the longwave cutoff (de Vries and Opsteegh, 2007) as well as wave frequency, energetics, and singular modes (Plougonven and Vanneste, 2010), we systematically investigate the sensitivity of the most unstable baroclinic mode to both changes across the tropopause region as well as different degrees of smoothing. We also include the effect of latent heating and contrast its impact on baroclinic growth to the structure of the tropopause.

2 Model and methods

2.1 Model setup and solution procedure

Focusing on the incipient stage of baroclinic development, we use a numerical extension of the linear 2D QG model by Eady (1949), formulated similarly to the model of Haualand and Spengler (2019) and Haualand and Spengler (2020), which is based on an analytic version of Mak (1994). We use pressure as the vertical coordinate and assume wavelike solutions in the x direction for the QG streamfunction ψ and vertical motion ω:

$$[\psi, \omega] = \mathrm{Re}\left\{ \left[\hat{\psi}(p), \hat{\omega}(p)\right] \exp(i(kx - \sigma t)) \right\}, \tag{1}$$

where the hat denotes Fourier transformed variables, k is the zonal wavenumber, and σ is the wave frequency. The non-dimensionalised ω and potential vorticity (PV) equations can then be expressed as

$$\frac{d^2\hat{\omega}}{dp^2} - Sk^2\hat{\omega} = i2\lambda k^3\hat{\psi} + k^2\hat{Q} \tag{2}$$

3

and

$$(\overline{u}k - \sigma)\left[\frac{d}{dp}\left(\frac{1}{S}\frac{d\hat{\psi}}{dp}\right) - k^2\hat{\psi}\right] + k\frac{d}{dp}\left(\frac{\lambda}{S}\right)\hat{\psi} = i\frac{d}{dp}\left(\frac{\hat{Q}}{S}\right) \,, \tag{3}$$

where S is the basic-state static stability as defined in Haualand and Spengler (2019), λ is the basic-state vertical wind shear, and $\overline{u}$ is the basic-state zonal wind. As introduced by Mak (1994) and implemented by Haualand and Spengler (2019), the diabatic heating rate *divided by pressure* is $Q = -\frac{\varepsilon}{2}h(p)\omega_{lhb}$, where ε is the heating intensity parameter, $h(p)$ is the vertical heating profile defined as 1 between the bottom (p_{lhb}) and the top of the heating layer (p_{lht}) and zero elsewhere, and ω_{lhb} is the vertical velocity at the bottom of the heating layer.

Unlike Mak (1994) and Haualand and Spengler (2019), we include an idealised tropopause with a default setup of uniform λ and S in the troposphere and in the stratosphere, separated by a discontinuity at the tropopause. The discontinuity introduces an interface condition for the vertical integral of the PV equation across the tropopause:

$$\left[\frac{1}{S}\frac{\partial\psi}{\partial p}\right]_{p_*^+}^{p_*^-} \propto \left[\frac{\lambda}{S}\right]_{p_*^+}^{p_*^-} \,, \tag{4}$$

where p_* is the pressure at the sharp tropopause interface and p_*^+ and p_*^- denote locations just below and just above the tropopause, respectively. Following Haualand and Spengler (2019), we refer to $\partial\psi/\partial p$, which is proportional to the negative density perturbation, as temperature. In line with Bretherton (1966), the jump in λ/S is proportional to the vertical integral of $\partial\overline{q}/\partial y$ across the sharp tropopause. Thus, the changes in λ and S across the tropopause introduce a meridional PV gradient at the tropopause, which is positive for the parameter space we explore.

The set of equations is completed with the boundary conditions $\hat{\omega} = 0$ at p_t and p_b, the thermodynamic equation

$$(\overline{u}k - \sigma)\frac{d\hat{\psi}}{dp} + i\hat{Q} + \lambda k\hat{\psi} = 0 \quad \text{at} \quad p = p_b, \tag{5}$$

as well as $\partial\psi/\partial p = 0$ at p_t, where p_t and p_b are the pressure at the top and bottom of the domain, respectively. The upper boundary condition is in line with Müller (1991) and Rivest et al. (1992) and prescribes vanishing temperature anomalies. As temperature anomalies at the model boundaries can be interpreted as PV anomalies (e.g., Bretherton, 1966; de Vries et al., 2010), this boundary condition is associated with zero PV anomalies at the model top, ensuring that the instability is mainly restricted to the troposphere, where PV anomalies at the tropopause mutually interact with PV anomalies at the surface. Additional tropospheric PV anomalies appear at the top and bottom of the heating layer in the presence of latent heating Q.

The default setup is the same as in Haualand and Spengler (2019) with the following exceptions (summarised in Table 1). The tropopause is at $p = p_* = 0.25$, corresponding to 250 hPa, and the model top is, in accordance with Mak (1998), at $p = p_t = 0$. Furthermore, the wind shear λ reverses sign across the tropopause, from $\lambda_{tr} = 3.5$ in the troposphere to $\lambda_{st} = -3.5$ in the stratosphere, with the zonal wind profile being defined as

$$\overline{u} = \begin{cases} \lambda_{tr}(p_b - p) & \text{for} \quad p \geq p_* \\ u_* + \lambda_{st}(p_* - p) & \text{for} \quad p < p_* \end{cases} \,, \tag{6}$$

Table 1. Setup of sharp and smooth CTL experiments

	λ_{st} [λ_{tr}]	S_{st} [S_{tr}]	p_*	$\hat{\alpha}$	δ
nondimensional	-3.5 [3.5]	4 [1]	0.25	1	0.15
dimensional	-0.035 [0.035]	0.04 [0.01]	250	1	150
units	ms^{-1}hPa^{-1}	m^2 s^{-2} hPa^{-2}	hPa	…	hPa

δ only applicable for smooth experiments.

which we argue is a good representation of the zonal wind profile in the midlatitudes when compared to observations (e.g.,
Birner et al., 2006; Houchi et al., 2010; Schäfler et al., 2020). In the stratosphere, the stratification $S_{st} = 4$ remains the same as
that of the full model domain in Mak (1994) and Haualand and Spengler (2019), but is reduced to $S_{tr} = 1$ in the troposphere,
which is a more representative value for the midlatitude troposphere (e.g., Birner, 2006; Grise et al., 2010; Gettelman and
Wang, 2015) and is consistent with previous studies (Rivest et al., 1992; de Vries and Opsteegh, 2007; Wittman et al., 2007).
The choice of a weaker tropospheric stratification results in stronger vertical motion and hence a larger scaling of latent heating
as well as increased growth rates. To compensate for this, we consistently reduce the heating intensity parameter of $\varepsilon = 12.5$
from Haualand and Spengler (2019) to $\varepsilon = 2$, such that the growth rates and the scaling of latent heating remain of the same
order of magnitude as in Haualand and Spengler (2019).

Equations (2), (3), and (5) form an eigenvalue problem that is solved numerically for the eigenvalue σ and the eigenvectors
$\hat{\psi}(p)$ and $\hat{\omega}(p)$ for a given wavenumber k. Due to the normalization constraint mentioned in Haualand and Spengler (2019),
the eigenvectors $\hat{\psi}(p)$ and $\hat{\omega}(p)$ are scaled arbitrarily and cannot be compared quantitatively across experiments. We use a
numerical resolution of 201 vertical levels with increments of 5 hPa and calculate solutions for 200 different wavenumbers.
See Haualand and Spengler (2019) for further details.

2.2 Smoothing procedure

To investigate the sensitivity of baroclinic instability to smoothing the tropopause, we substitute the step function of λ/S
around the tropopause with a sine function that gradually increases from $(\lambda/S)_{st}$ in the upper stratosphere to $(\lambda/S)_{tr}$ in the
lower troposphere in a vertical range symmetric around the sharp tropopause interface, i.e., $p_* - \delta/2 \leq p \leq p_* + \delta/2$:

$$\frac{\lambda}{S}(p) = \begin{cases} (\lambda/S)_{st} \, \hat{\alpha} & \text{for} & 0 \leq p < p_* - \delta/2, \\ \frac{1+\alpha}{2}(\lambda/S)_{tr} + \frac{1-\alpha}{2}(\lambda/S)_{tr} \, \sin[\tau(p)] & \text{for} & p_* - \delta/2 \leq p \leq p_* + \delta/2, \\ (\lambda/S)_{tr} & \text{for} & p_* + \delta/2 < p \leq 1, \end{cases} \quad (7)$$

where $\tau(p)$ increases linearly from $-\pi/2$ at $p = p_* - \delta/2$ to $\pi/2$ at $p = p_* + \delta/2$ such that $\sin[\tau(p)] \in [-1, 1]$ for $p \in [p_* -$
$\delta/2, p_* + \delta/2]$, and $\alpha = \hat{\alpha} \dfrac{(\lambda/S)_{st}}{(\lambda/S)_{tr}}$ is the scaling parameter, with $\hat{\alpha}$ being an offset parameter that shifts $(\lambda/S)_{st}$ such that the
vertical integral of $\partial \overline{q}/\partial y$ around the tropopause region is modified when $\hat{\alpha} \neq 1$ compared to when $\hat{\alpha} = 1$. We conduct sharp
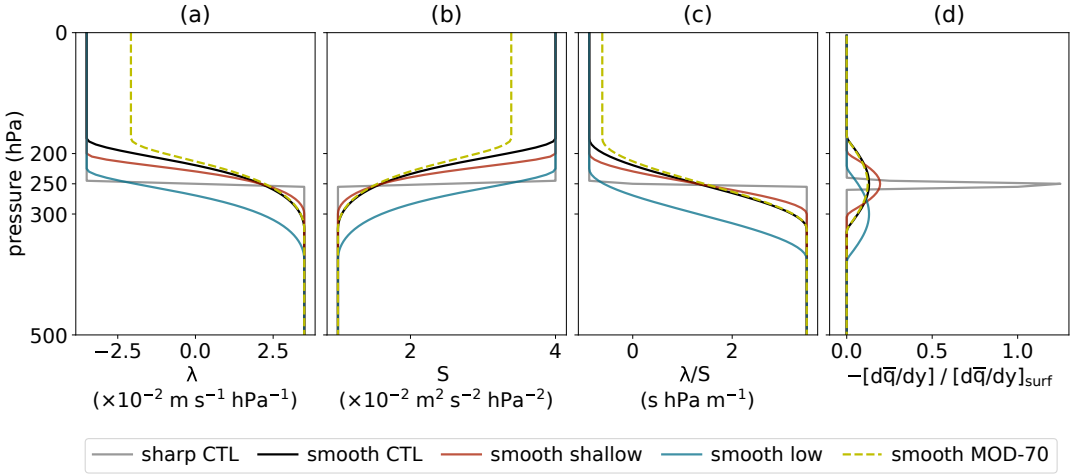
Figure 1. Vertical profiles of λ, S, λ/S, and $\partial\overline{q}/\partial y$ near the tropopause for some key experiments.

and smooth experiments with $p_* = 250$ hPa, $\hat{\alpha} = 1$, and $\delta = 0$ hPa and $\delta = 150$ hPa for the "sharp CTL" and "smooth CTL", respectively (grey and black profiles in Fig. 1). These settings are summarised in Table 1 together with the default setup of λ and S. We further vary δ between 50 hPa and 200 hPa (compare black and red profiles in Fig. 1), p_* between 200 hPa and 300 hPa (compare black and blue profiles), and $\hat{\alpha}$ between 1 and 0.7 (compare black and dashed yellow profiles). Note that due to the finite resolution of the model grid, there is always some smoothing even for the sharp profiles, which results in a finite value of $\partial\overline{q}/\partial y$ in Fig. 1d.

The choices for δ, p_*, and $\hat{\alpha}$ are based on vertical profiles in the midlatitudes from observational studies (Birner et al., 2002; Birner, 2006; Grise et al., 2010; Gettelman and Wang, 2015; Schäfler et al., 2020), where the motivation for varying the offset parameter down to $\hat{\alpha} = 0.7$ is based on the finding that some models only capture about 70% of the observed magnitude of the wind shear (Schäfler et al., 2020, see their Fig. 9 c,d). Experiments with $\hat{\alpha} \neq 1$, resulting in a modified vertical integral of the horizontal PV gradient, are labeled "MOD", with the offset parameter $\hat{\alpha}$ shown in percentage after "MOD", such that "MOD-70" corresponds to $\hat{\alpha} = 0.7$ and means that $(\lambda/S)_{st}$ is reduced to 70% of its original value. In some cases we also refer to experiments with $\hat{\alpha} = 1$ and hence an unaltered vertical integral of the horizontal PV gradient as "NO-MOD" experiments to avoid confusion with the MOD experiments.

After smoothing λ/S, we define the smoothed profiles of λ and S (see Fig. 1a,b) by letting

$$\lambda(p) = \lambda_{st}\hat{\alpha} + \Delta\lambda \cdot \gamma(p) \quad \text{and} \quad S(p) = S_{st}\hat{\alpha} + \Delta S \cdot \gamma(p),$$

where $\Delta\lambda = \lambda_{tr} - \lambda_{st}\,\hat{\alpha}$ and $\Delta S = S_{tr} - S_{st}\,\hat{\alpha}$ are the respective differences in λ across the tropopause region and

$$
\gamma(p) = \begin{cases}
0 & \text{for} & 0 \leq p < p_* - \delta/2, \\[2mm]
-\hat{\alpha}\dfrac{\lambda_{st} - S_{st}\,\dfrac{\lambda}{S}(p)}{\Delta\lambda - \Delta S\,\dfrac{\lambda}{S}(p)} & \text{for} & p_* - \delta/2 \leq p \leq p_* + \delta/2, \\[2mm]
1 & \text{for} & p_* + \delta/2 < p \leq 1,
\end{cases}
$$

is a factor based on the smoothed profile of λ/S ensuring that the smoothing of λ and S is distributed equally from $p = p_* - \delta/2$

160 to $p = p_* + \delta/2$ relative to the total increments $\Delta\lambda$ and ΔS. After defining the smoothed profile $\lambda(p)$, we set $\overline{u}(p) = \int_{p_b}^{p} \lambda(p)\,dp$, where we assumed $\overline{u}(p_b) = 0$.

Note that if the step function of λ shifts sign at the tropopause, while S is positive everywhere, the zero value of the smoothed profile of λ/S will be located at a higher vertical level than the discontinuity of the original sharp profile at p_*. Thus, the maximum vertical gradient of λ and S is, unlike that of λ/S, typically shifted above the tropopause (compare e.g., black

165 lines in Fig. 1a-c).

2.3 Energy equations

The relation between baroclinic growth and changes in wind shear and stratification across the tropopause is investigated from the energetics perspective following Lorenz (1955). The tendency of domain averaged eddy available potential energy EAPE is

170 $$\frac{\partial}{\partial t}(\text{EAPE}) = C_a - C_e + G_e,\tag{8}$$

where $C_a = -\dfrac{\lambda}{S}\overline{\psi_x\psi_p}$ is the conversion from basic-state available potential energy (APE) to EAPE, $C_e = \overline{\omega\psi_p}$ is the conversion from EAPE to eddy kinetic energy, and $G_e = -\dfrac{1}{S}\overline{Q\psi_p}$ is the diabatic generation of EAPE. The bar denotes zonal and vertical averages.

2.4 Validity of QG assumptions

175 Although several other studies have implemented discontinuous vertical profiles of λ and/or S around an idealised tropopause in QG models (e.g., Robinson, 1989; Rivest et al., 1992; Juckes, 1994; Plougonven and Vanneste, 2010), Asselin et al. (2016) argued that the quasi-geostrophic approximation is less appropriate near sharp gradients and narrow zones like the tropopause. Hence, to justify our modelling framework, we tested the validity of the QG approximation by comparing the magnitude of the QG terms in the thermodynamic equation with the magnitude of the nonlinear vertical advection term neglected in the QG

180 framework. As such a quantitative comparison between linear and nonlinear terms requires a scaling of variables (see section 2.1), we chose a maximum surface wind of $5\ \mathrm{ms}^{-1}$ across all experiments, which is in line with our focus on the incipient stage of baroclinic development.

For the sharp CTL experiment, where profiles are discontinuous across the tropopause, the nonlinear vertical advection term is less than 0.25 of the dominant QG term in the thermodynamic equation at all grid points in the baroclinic wave apart from the tropopause interface (not shown). Given the discontinuity at the tropopause due to the jump in wind shear and stratification, the temperature is actually undefined at this level and it is therefore inconsistent to evaluate the thermodynamic equation at this interface.

For the smooth CTL experiment, where profiles are smoothed across the tropopause, the vertical advection term is also less than 0.25 of the dominant QG term at most grid points, though near the tropopause this ratio becomes up to 7.5 (4.7) [3.3] when the vertical extent of the tropopause is 100 (150) [200] hPa. Thus, there are grid points where the non-linear vertical advection term becomes dominant. However, that we obtained qualitatively similar solutions for all smoothing ranges, including the sharp experiment, indicates the suitability of QG framework to explore the sensitivity to the sharpness of the tropopause.

3 Impact of wind shear and stratification across the tropopause on baroclinic growth

3.1 Control setup with sharp jet and stratification jump

Introducing the effect of variations in λ and S across the tropopause, we first compare the sharp CTL experiment, where both λ and S are discontinuous across the tropopause (see Sect. 2.1), with setups where either only λ is discontinuous across the tropopause (sharp CTL-λ) or only S is discontinuous across the tropopause (sharp CTL-S). For the sharp CTL experiment, the growth rate [wavelength] of the most unstable mode (black line in Fig. 2) is stronger [longer] than if only λ is discontinuous (grey) and weaker [shorter] than if only S is discontinuous (blue). For all of these experiments, there is a longwave cutoff that is related to a non-matching phase speed of the waves at the tropopause and the surface, which is in line with the arguments by Blumen (1979), de Vries and Opsteegh (2007), and Wittman et al. (2007). The qualitative differences in growth rate and wavelength of the most unstable mode as well as the shortwave and longwave cutoffs between these three experiments are the same as those found by Müller (1991) (see his Fig. 2). We present a more detailed discussion of these findings in subsection 3.2, where we explore the parameter space of λ and S more extensively.

Below the tropopause, the structure of ψ (shading in Fig. 3a) and temperature T (black contours) for the most unstable mode is similar to the structure of the most unstable Eady mode, with ψ tilting westward and T tilting eastward with height. Together with the westward tilt in both ω (Fig. 3a) and meridional wind $v = ik\psi$ (not shown, but phase shifted a quarter of a wavelength upstream from ψ), this structure is baroclinically unstable and is consistent with warm air ascending poleward and cold air descending equatorward.

In contrast to the Eady model, where the tropopause is represented by a rigid lid, the inclusion of a tropopause with discontinuous profiles of λ and S introduces nonzero ω at the tropopause interface. Just below the tropopause, this nonzero ω adiabatically cools (warms) the air upstream of the positive (negative) temperature anomaly (compare grey contours and shading in Fig. 3a), thereby weakening the temperature wave as well as accelerating its downstream propagation. This effect is opposed by the meridional temperature advection, which warms (cools) the air upstream of the positive (negative) temperature anomaly just below the tropopause. Thus, with a negative meridional temperature gradient associated with the positive
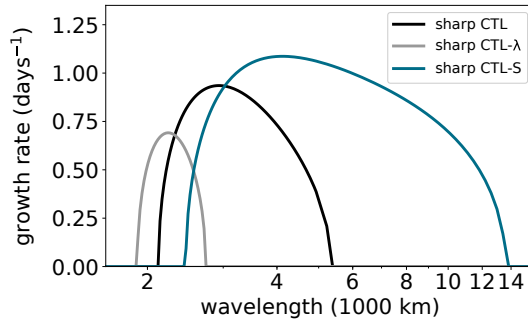
Figure 2. Growth rate vs. wavelength for the sharp CTL (black), CTL-λ (grey), and CTL-S (blue) experiments. See text for further details.
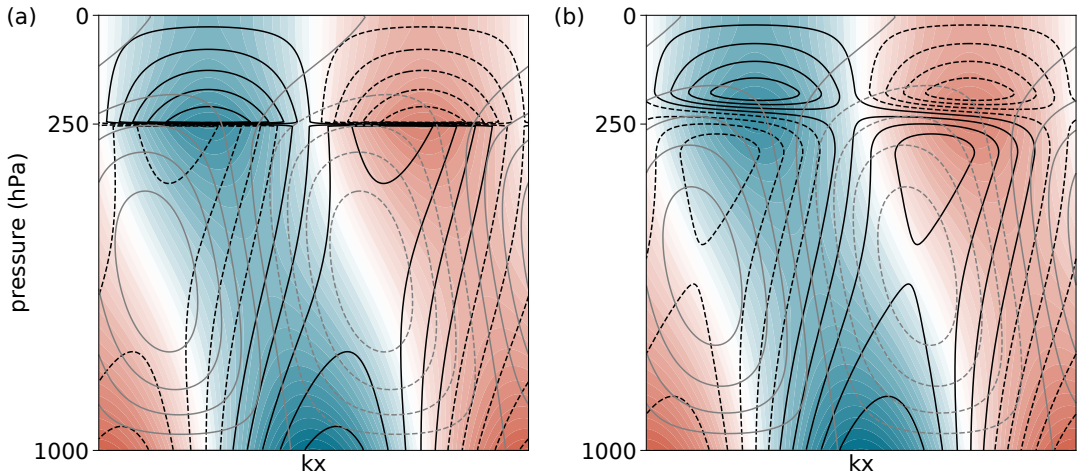

Figure 3. Structure of ψ (shading), $-\partial\psi/\partial p$ (black contours), and ω (grey contours) for (a) the sharp CTL experiment and (b) the smooth CTL experiment. Values are not comparable to physical values due to normalisation constraint mentioned in Sect. 2.1.

wind shear λ via the thermal wind relation, meridional temperature advection amplifies the temperature wave and retards its downstream propagation at this level. The net effect is propagation against the zonal wind such that the propagation speed of the temperature wave just below the tropopause matches the propagation speed of the wave at the surface. Only when these propagation speeds are identical, the waves can phase lock and travel together with a common propagation speed that equals the average phase speed of the two waves (de Vries and Opsteegh, 2007).

The phase of the temperature wave reverses across the tropopause and does not tilt with height in the entire stratosphere (shading in Fig. 3). Such a barotropic structure is in line with the lack of mutual intensification of PV anomalies in this layer. There is a monotonic decay of the temperature anomaly toward the top of the model domain related to the upper boundary condition $\partial\psi/\partial p = 0$. Together with the barotropic structure, this decay yields $T \propto -\partial\psi/\partial p$ being exactly in phase with $-\psi$

225   and therefore also exactly 90 degrees out of phase with $v = ik\psi$. Nevertheless, due to the reversal of the wind shear across the tropopause, the meridional temperature advection is still retarding the downstream wave propagation above the tropopause such that the stratospheric part of the wave propagates together with the tropospheric part.

However, due to the 90 degrees phase shift between v and T, meridional advection can no longer amplify the stratospheric part of the temperature wave. Instead, the amplification of the wave in the stratosphere is entirely due to ω, where ω is almost

230   in phase with temperature. Hence, the role of ω on the amplification of the wave reverses across the tropopause.

The weakening and acceleration of the temperature wave just below the tropopause associated with nonzero ω is in line with a weaker growth rate, higher phase speed, and hence longer wavelength compared to the most unstable Eady mode (compare contour at the black dot with the black contour in Fig. 4). Such effects on baroclinic development were also found in similar experiments by Müller (1991) and partly by de Vries and Opsteegh (2007).

235   ## 3.2   Sensitivity to variations in stratospheric wind shear and/or stratification

Varying λ_{st} and S_{st} while holding λ_{tr} and S_{tr} fixed changes $\partial\overline{q}/\partial y$ through its relation to the jump in λ/S across the tropopause (see Eq. (4) and related arguments), which has implications for baroclinic growth through the arguments of mutual intensification by interacting PV anomalies (Hoskins et al., 1985). For the parameter space explored in this study, decreasing λ_{st} relative to λ_{tr} always increases $\partial\overline{q}/\partial y$, whereas increasing S_{st} relative to S_{tr} increases $\partial\overline{q}/\partial y$ only when λ_{st} is positive

240   and decreases $\partial\overline{q}/\partial y$ when λ_{st} is negative (Fig. 4d).

The increase in $\partial\overline{q}/\partial y$ for varying λ_{st} and S_{st} yields the observed decrease in phase speed and wavelength (compare pattern of black contours in Fig. 4b-d). As argued by Wittman et al. (2007), the relation between $\partial\overline{q}/\partial y$, phase speed, and wavelength is in line with the proportionality of the phase speed of Rossby waves to $-1/k \cdot \partial\overline{q}/\partial y$. Thus, a larger positive $\partial\overline{q}/\partial y$ reduces the phase speed, which can be partly compensated by increasing the wavenumber k. A similar qualitative relation between

245   increasing wavelengths for decreasing $\partial\overline{q}/\partial y$ related to varying λ_{st} and S_{st} was found by Müller (1991) (see his Fig. 2b). Müller (1991) also found that decreasing λ_{st} reduces the phase speed for a ratio of static stability of 1.5 across the tropopause (see his Fig. 3a-c), which is confirmed by our results (Fig. 4c). Furthermore, our results also show that this relation between λ and phase speed holds for all investigated configurations of S_{st}.

The sensitivity on the growth rate is less straightforward, with growth rates being largest in the upper right corner of the

250   λ-S parameter space, where the wind shear is uniform and the stratification in the stratosphere is larger than in the troposphere (Fig. 4a). Growth rates decrease from this maximum toward weaker λ_{st} and S_{st}. A similar sensitivity on the growth rate to changes in λ and S was found by Müller (1991), where the growth rate of the most unstable mode also peaked when λ_{st} and S_{st} were large and decreased toward weaker λ_{st} and S_{st} (see his Fig. 2a). While the decrease in growth rates toward the upper left corner of the λ-S parameter space in Fig. 4a can be explained by the absence of a tropopause due to a uniform λ and S
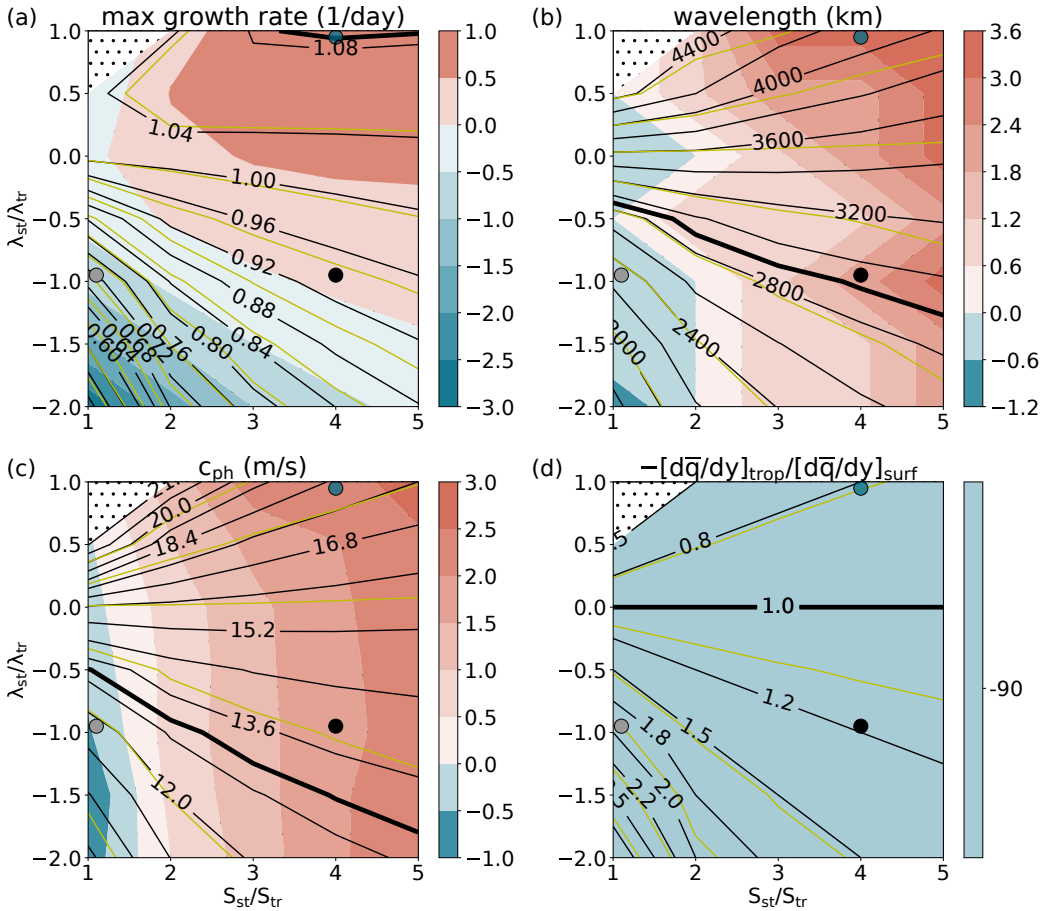
Figure 4. Growth rate, wavelength, and phase speed of the most unstable mode together with absolute value of $\partial \overline{q}/\partial y$ at the tropopause relative to its value at the surface for various λ and S in the stratosphere (subscript st) and troposphere (subscript tr). Black (yellow) contours show absolute values of experiments with discontinuous (smooth) profiles, and shading shows relative difference between the discontinuous and smooth experiments in percentage. The values for the most unstable Eady mode with a rigid lid at the tropopause using λ_{tr} and S_{tr} are marked by a bold contour. Small black dots indicate regions where no solution is calculated due to the absence of unstable solutions. Big black, grey, and blue dots mark the configurations of λ and S used for the sharp CTL, CTL-λ, and CTL-S experiments in Fig. 2, respectively.
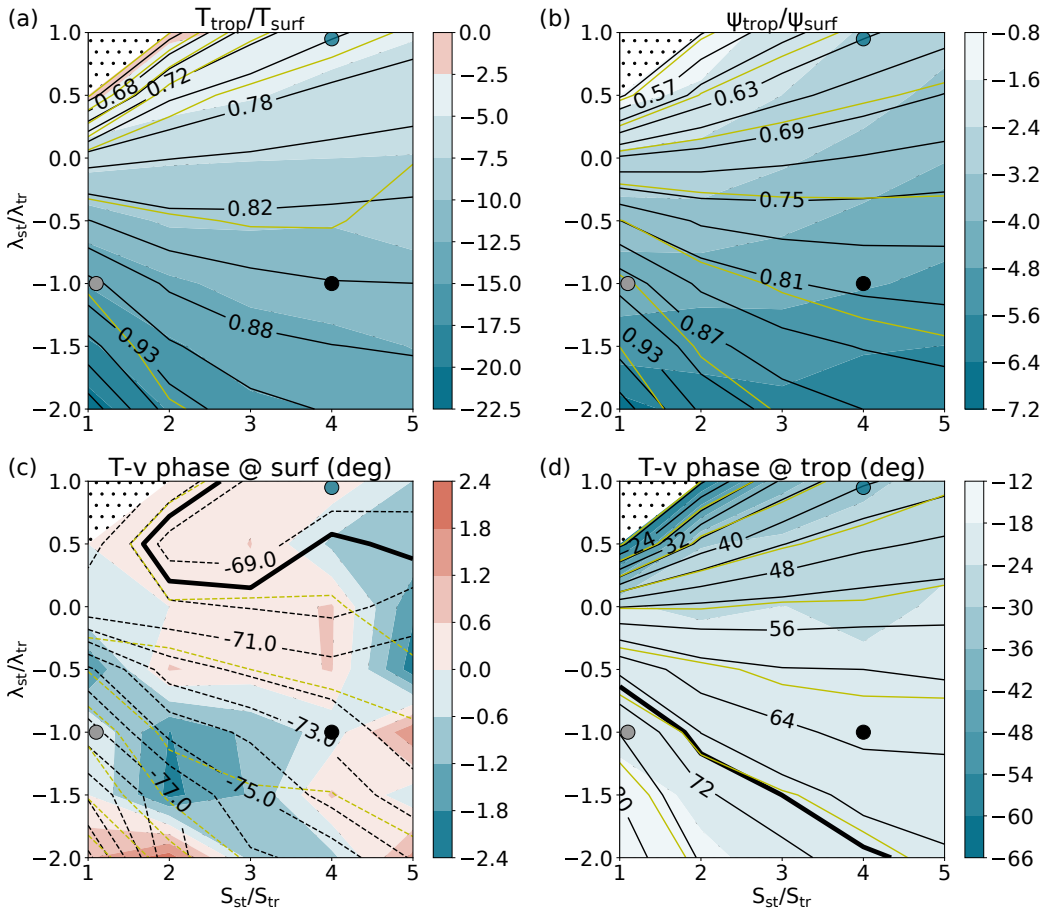
Figure 5. Same as Fig. 4, but for $-\partial\psi/\partial p$ and ψ at the tropopause relative to surface and the phase shift of T and v at the surface and just below the tropopause.

resulting in no upper level wave and hence no instability, the relation of the growth rate to the choices in the λ-S parameter space is more complex.

To further understand the changes in growth rate, we consider the conversion of basic-state APE to EAPE (C_a), which is constant with height in the troposphere where PV anomalies mutually intensify (not shown). As this energy conversion term

is the main source for EAPE when dry baroclinic waves intensify, it should reflect the observed changes in growth rate. We
260 therefore explore this term by considering the location and amplitude of $v \sim \psi_x$ and $T \sim \psi_p$.

Just below the tropopause, v and T are more in phase when λ_{st} is positive (Fig. 5d), which is beneficial for the energy
conversion. At the surface, v and T are generally less in phase than just below the tropopause and changes in phase between
v and T are small for different λ_{st} and S_{st} (Fig. 5c). Given that C_a is constant throughout the troposphere, the different phase
relation between v and T at the surface and just below the tropopause are consistent with larger amplitudes of $v = ik\psi$ and T
265 at the surface relative to the amplitudes just below the tropopause (Fig. 5a,b). This dominance of v and T at the surface relative
to just below the tropopause is strongest when the phase between v and T just below the tropopause and the magnitude of
$\partial \overline{q}/\partial y$ are small (compare pattern of Figs. 4d, 5a, and 5d). For positive λ_{st}, we thus argue that the beneficial phase relation
between v and T and the larger amplitudes of v and T at the surface favour a larger conversion of basic-state APE to EAPE
(C_a) compared to when λ_{st} is negative. With a large source of EAPE, baroclinic growth is expected to intensify.

270 To justify the argument relating increased growth rates to an increased source of EAPE through C_a, we need to understand
what sets the phase relation between v and T. Due to the difference condition for temperature across the tropopause in Eq.
(4), where the difference in $1/S \cdot \partial \psi / \partial p$ is proportional to the jump in λ/S and hence the vertical integral of $\partial \overline{q}/\partial y$ across
the tropopause, the temperature anomaly typically reverses across the tropopause (see example in Fig. 3a). When the jump in
λ/S is large, the temperature difference is also large, such that the temperature anomaly just below the tropopause becomes
275 zonally more aligned with the opposite temperature anomaly just above the tropopause, reducing the freedom for a phase shift
to a more beneficial phase relation with the meridional wind. In contrast, when the jump in λ/S is small, the difference in
temperature across the tropopause is less constrained such that the temperature anomaly just below the tropopause can more
easily be shifted upshear to be more in phase with the meridional wind.

In line with these arguments, the jump in temperature across the tropopause is monotonically increasing with decreasing
280 $\lambda_{st}/\lambda_{tr}$ when S_{st} and S_{tr} are constant (not shown). In contrast, as mentioned in the beginning of this subsection, an increase
in S_{st} relative to S_{tr} increases the jump in λ/S only when λ_{st} is positive and is therefore not always associated with an increase
in the difference of T across the tropopause. Furthermore, as S appears on both sides of the difference condition in Eq. (4), an
increase of S_{st} relative to S_{tr} can compensate for a significant part of the changes in the jump of $1/S \cdot \partial \psi / \partial p$, which would
leave the temperature more or less unaltered.

285 It is also worth noting that increasing S_{st} yields a more dominant omega term in the thermodynamic equation that amplifies
the temperature anomaly just above the tropopause (as discussed in section 3.1). For a given difference in temperature across
the tropopause, the latter effect allows the temperature wave below the tropopause to move more freely away from its antiphase
relation with the wave above the tropopause, thereby improving its correlation with v. The above arguments related to the
complex role of S on temperature near the tropopause demonstrate that the phase relation between v and T just below the
290 tropopause is more sensitive to changes in λ than S (as shown in Fig. 5d).

The arguments related to the beneficial phase relation between v and T for large λ_{st} together with the absence of instability
for uniform λ and S, i.e., no tropopause, yield the observed pattern in growth rates (Fig. 4a), with a maximum where λ
is uniform and the jump in S is large. Hence, baroclinic growth is not largest when the tropopause is at its most abrupt

configuration (lower right corner around the black dot in Fig. 4), but rather when the linear increase in zonal wind is extended

295   to above the tropopause (upper right corner around the blue dot in Fig. 4).

4 Impact of smoothing the tropopause on baroclinic growth

4.1 Sensitivity to variations in stratospheric wind shear and/or stratification

Smoothing the vertical profiles of λ and S in a vertical extent of 150 hPa around the tropopause yields a similar structure of the most unstable mode as for the experiments with discontinuous profiles (compare Figs. 3a and b). Moreover, the sensitivity to λ

300   and S for growth rate, wavelength, phase speed, and $\partial \overline{q}/\partial y$, as well as the amplitude and phase of v and T remain qualitatively the same after smoothing (compare black and yellow contours in Figs. 4 and 5), with growth rates still peaking when λ_{st} and S_{st} are large.

Even though smoothing weakens the maximum of $\partial \overline{q}/\partial y$ by 90% (shading in Fig. 4d), the growth rate, wavelength, and phase speed change by less than $\pm 4\%$ (shading in Fig. 4a-c). In line with a weaker $\partial \overline{q}/\partial y$ and the dispersion relation for

305   Rossby waves (as discussed in Sect. 3.2), smoothing increases the wavelength and the phase speed for most of the investigated configurations of λ_{st} and S_{st} (Fig. 4b,c) and decreases the growth rates by up to 2.9% when λ_{st} is negative and S_{st} is weak (Fig. 4a).

However, when λ_{st} and S_{st} are large, the growth rate *increases* by up to 0.9% (Fig. 4a). We argue that this enhancement is related to an improved phase relation between v and T compared to the experiments with discontinuous profiles (shading

310   in Fig. 5d), where a smooth tropopause with a wider vertical distribution of $\partial \overline{q}/\partial y$ yields more flexibility in relative location between the temperature anomalies just below and above the tropopause. Such an improved phase relation is associated with enhanced conversion of basic-state APE to EAPE and may overcompensate for the detrimental impact from the weakening of $\partial \overline{q}/\partial y$. In fact, for the most realistic setup where both λ and S change across the tropopause (around the black dot in Fig. 4a), the sensitivity on the growth rate from smoothing is almost negligible, indicating that the positive impact related to the

315   improved phase relation between v and T is balanced by the detrimental impact from the weakening of $\partial \overline{q}/\partial y$. This suggests that baroclinic growth is typically not very sensitive to an accurate representation of λ and S around the tropopause.

The perhaps largest qualitative difference from the impact of smoothing on the overall instability analysis is an additional mode at long wavelengths when λ_{st} is negative and S_{st} is large (Fig. 6). The streamfunction structure of this mode features its strongest westward tilt with height within the smoothed tropopause region and decays rapidly above (not shown). This mode

320   exists only due to the additional levels of opposing and nonzero $\partial \overline{q}/\partial y$ in the smoothed tropopause region. We will not focus on these modes at long wavelengths, as we argue that their weak growth rate and long wavelength as well as their westward tilt bound solely to the tropopause region make them less relevant for an assessment for typical midlatitude cyclones.
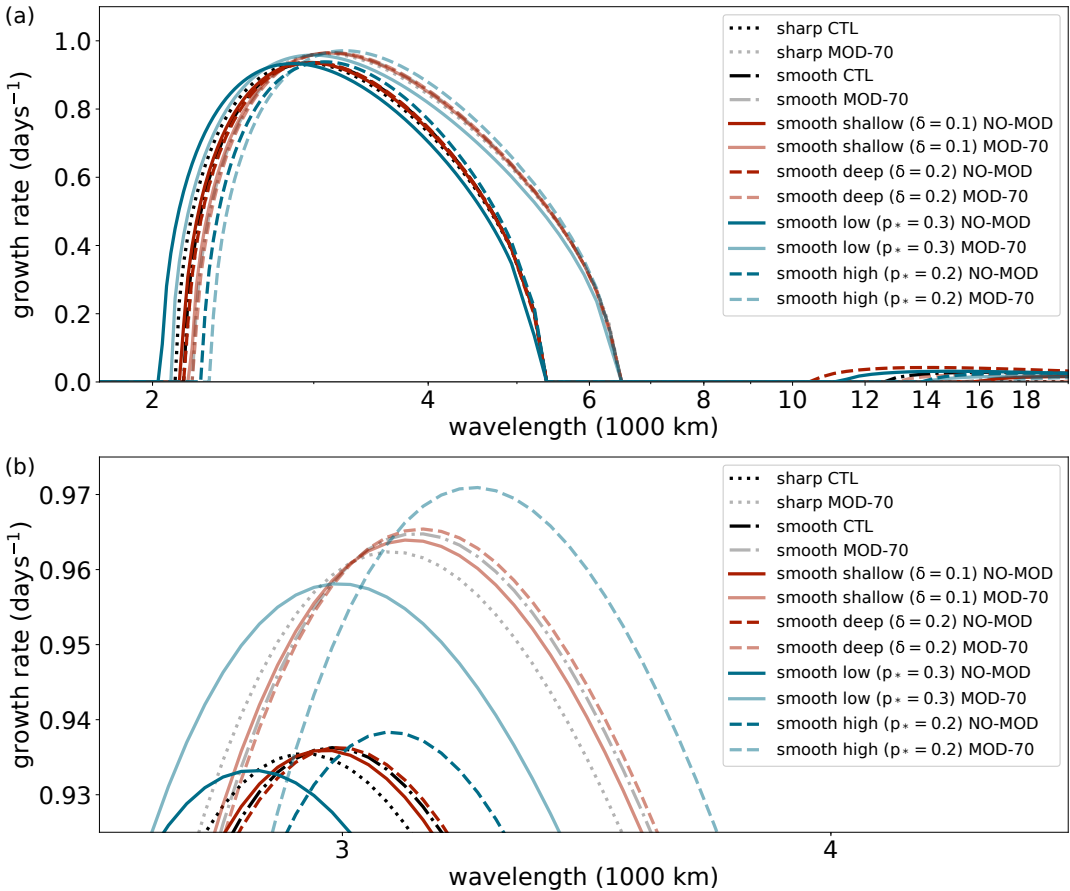
Figure 6. (a) Growth rate vs. wavelength for $\lambda_{tr} = 3.5$, $\lambda_{st} = -3.5$, $S_{tr} = 1$, $S_{st} = 4$ and various sensitivity experiments, with the default smooth experiment being associated with a tropopause region of 150 hPa depth centered at an altitude of 250 hPa. See text for further details. (b) Zoom-in of (a).

4.2 Sensitivity to vertical extent and altitude of tropopause

Comparing the sensitivity of baroclinic growth to the vertical extent of smoothing, tropopause height, and changes in the vertical integral of $\partial \overline{q}/\partial y$ (see details in Sect. 2.2), the greatest sensitivity is related to the changes in the vertical integral of $\partial \overline{q}/\partial y$, where the growth rates of the sharp and smooth MOD-70 experiments are similar and increase by 2.7% to 3.5%

compared to their NO-MOD counterpart experiments (compare sharp and faint colours in Fig. 6). The increase in growth rate from the NO-MOD experiments to the MOD-70 experiments is associated with a decrease in $\partial \overline{q}/\partial y$ at the tropopause toward a more optimal value that better matches with the $\partial \overline{q}/\partial y$ at the surface (not shown), such that the waves at the tropopause and at the surface can more easily phase lock and travel together with the same phase speed (Blumen, 1979; de Vries and Opsteegh, 2007; Wittman et al., 2007). For the NO-MOD experiments, the sensitivity to tropopause height (solid and dashed blue in Fig. 6) and vertical extent of smoothing (solid and dashed red) changes the growth rate by only -0.24% to 0.31% compared to the sharp control experiment (black).

The sensitivity to vertical extent of smoothing and tropopause height is qualitatively the same for both the NO-MOD and the MOD-70 experiments. Lowering (raising) the tropopause weakens (enhances) the growth rate (solid and dashed blue in Fig. 6). This can be related to an increased (decreased) vertical average of S from the surface to the tropopause (Fig. 7)

$$\overline{S}_{tr} = \frac{1}{p_* - p_b} \int\limits_{p_b}^{p_*} S_{tr} \, dp,$$

where the stratification is related to the growth rate through the inverse proportionality between the static stability and the maximum Eady growth rate (Lindzen and Farrell, 1980; Hoskins et al., 1985).

In contrast to the sensitivity to tropopause height, increasing the vertical extent of smoothing does not necessarily have a monotonic impact on the growth rate. Deepening the tropopause region from a narrow (solid red in Fig. 6) to an intermediate (dash-dotted black) vertical extent of smoothing increases the growth rate. However, deepening the tropopause further from an intermediate to a wide (dashed red) extent of smoothing barely changes the growth rate. Moreover, when increasing the smoothing further, i.e., beyond the displayed sensitivity range, the growth rate starts to decrease (not shown). For the MOD-70 experiments, the turnover point, i.e., where increased extent of smoothing starts to weaken the growth rate, exists at a larger extent of smoothing that is beyond our sensitivity range considered for the NO-MOD experiments (not shown).

The maximum in growth rate for some intermediate degree of smoothing is associated with an intermediate $\partial \overline{q}/\partial y$ and an intermediate phase speed of the wave at the tropopause (recall that the phase speed for Rossby waves is proportional to $-\partial \overline{q}/\partial y$). Such an intermediate phase speed appears to be the most optimal phase speed yielding the best match in phase speed for the surface wave, such that the waves at these two levels phase lock and intensify each other as efficiently as possible.

Changes in growth rate relative to the sharp CTL experiment are summarised in Fig. 8, including experiments with simultaneous modifications of the vertical extent and altitude of the tropopause for different modifications of the vertical integral of the PV gradient. This figure highlights that the main relative change in growth rate is related to the modification of the vertical integral of the PV gradient rather than modifications of vertical extent and altitude of the tropopause.

4.2.1 Changes in growth rate and corresponding forecast error

The changes in growth rate may seem small, but as variables grow nearly exponentially at the incipient stage of development, errors grow quickly with time. Relative to a reference experiment (subscript *ref*), the forecast error of the relative wave
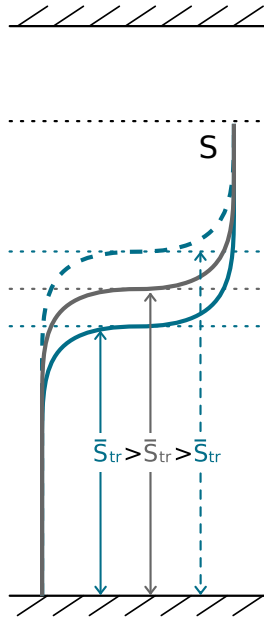
Figure 7. Schematic illustrating how the altitude of the tropopause modifies the vertical average of the tropospheric stratification $\overline{S}$.

amplitude A'/A_{ref} at the time $t = t_1$ is

$$\left.\frac{A'}{A_{\mathrm{ref}}}\right|_{t=t_1} = \left(1 + \left.\frac{A'}{A_{\mathrm{ref}}}\right|_{t=0}\right) \exp[(\sigma - \sigma_{\mathrm{ref}})t] - 1. \tag{9}$$

360 Assuming perfect initial conditions, i.e., $A'/A_{\mathrm{ref}} = 0$ at $t = 0$, the forecast error for the NO-MOD smooth experiments relative to the sharp control experiment is less than +/- 1% [2%] during a short-range forecast of 2 days [medium-range forecast of 5 days], while the corresponding error for the MOD-70 experiments is up to 6% [17%] (dashed lines in Fig. 9). In comparison, assuming a relative initial error of 5%, the relative forecast error is down to 4% [3%] after 2 [5] days for the NO-MOD smooth experiments, and up to 12% [22%] for the MOD-70 experiments. The decrease in the relative error for some of the NO-MOD

365 smooth experiments is a result of an underestimate of the growth rate relative to the sharp control experiment, which reduces the initial positive relative error. If the growth rates are compared to the growth rate of a weakly smoothed experiment instead of the sharp reference experiment, the error is more or less unaltered. We therefore let the growth rate of the sharp experiment be the reference for the error growth calculations.

Keeping in mind that these results are based on a highly idealised model, the findings indicate that it is not so important

370 if models fail to accurately represent λ and S around the tropopause. Instead, it is much more important that λ and S are well represented in the lower stratosphere, such that the vertical integral of $\partial\overline{q}/\partial y$ around the tropopause region is preserved.
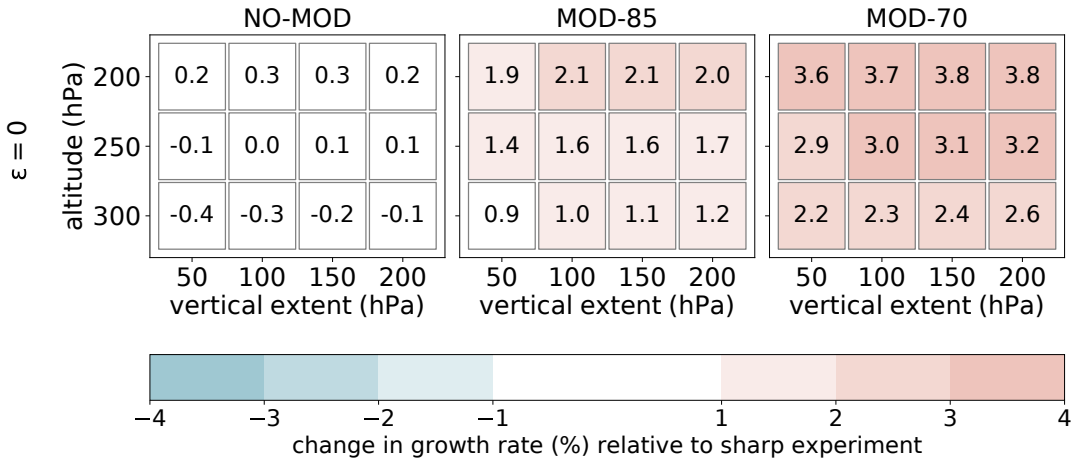
Figure 8. Change in growth rate (shading and numbers) for various smooth experiments relative to CTL with discontinuous profiles from Fig. 6 for no latent heating ($\varepsilon = 0$).

The importance of representing the lower stratospheric winds is further supported by Rupp and Birner (2021), who found that baroclinic lifecycle experiments are sensitive to changes in the wind structure in the lower stratosphere. Such changes in wind structure are often related to a downward extension of a weak polar vortex after sudden stratospheric warming events (Baldwin and Dunkerton, 2001), which have been shown to significantly alter midlatitude weather in the troposphere (see review by Kidston et al., 2015, and references therein).

4.3 Sensitivity to latent heating intensity

Including latent heating in the mid-troposphere does not significantly change the qualitative findings of the sensitivity experiments from section 4.2 (compare Fig. 10 with Fig. 6). Nevertheless, the most unstable mode at shorter wavelengths is associated with dominant diabatic PV anomalies at the heating boundaries (Fig. 11b), which align with the westward tilt of ψ (Fig. 11a). Growth rates peak at shorter wavelengths, which is consistent with the presence of diabatic PV anomalies and hence a shallower effective depth of interacting PV anomalies (Hoskins et al., 1985).

For some of the experiments, the weak and positive growth rates at long wavelengths are split into two modes (Fig. 10). The longest of the two is similar to their adiabatic counterpart mentioned in the end of Sect. 4.1, while the shortest of the two is associated with the increased dominance of the diabatic PV anomalies at the top of the heating layer. Due to the irrelevance for midlatitude cyclones mentioned in section 4.1, these modes are beyond the scope of this study.

In line with the dominance of diabatic PV anomalies in the lower and middle troposphere, latent heating also weakens the relative sensitivity to the modifications of the vertical integral of $\partial \overline{q} / \partial y$ across the tropopause (compare Fig. 10 with Fig. 6),
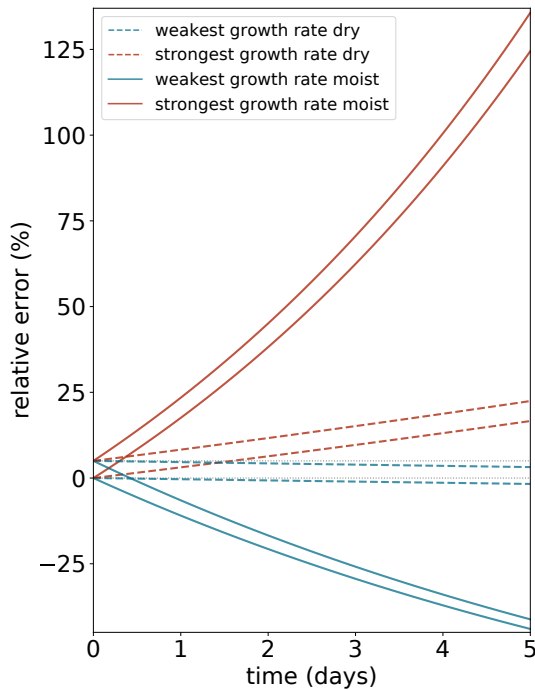
Figure 9. Evolution of error for the weakest (blue) and strongest (red) maximum growth rates from Fig. 6 (dashed, dry) and Fig. 10 (solid, moist) starting with initial relative errors of 0% and 5% (grey dotted horizontal lines).

with growth rates for the MOD-70 experiments increasing by only 1.0-1.1% relative to the NO-MOD counterpart experiment
instead of 2.7-3.5% as for the adiabatic experiments. Keeping the idealised context of this study in mind, this finding indicates
that the presence of latent heating makes models relatively less vulnerable to an inaccurate representation of λ and S around
the tropopause.

Decreasing (increasing) the heating parameter from $\varepsilon = 2$ to $\varepsilon = 1.5$ ($\varepsilon = 2.5$), which corresponds to a 25% decrease (in-
crease) in latent heating and associated precipitation, yields a much larger variation in the maximum growth rate compared to
the tropopause sensitivity experiments for a fixed heating parameter (Fig. 12). The change in growth rate relative to the sharp
experiment for $\varepsilon = 2$ is between -10.2% (for $\varepsilon = 1.5$) and +14.2% (for $\varepsilon = 2.5$), and the corresponding error after 2 [5] days is
between -21% [-44%] (for $\varepsilon = 1.5$) and +38% [+124%] (for $\varepsilon = 2.5$) if there are no initial errors, and a few percent larger if
the relative initial error is 5% instead (solid lines in Fig. 9). In comparison, the corresponding numbers for the relative change
in growth rate when changing the latent heating intensity ε by only 5% [10%] instead of 25% are between -2.4% [-4.5%] and
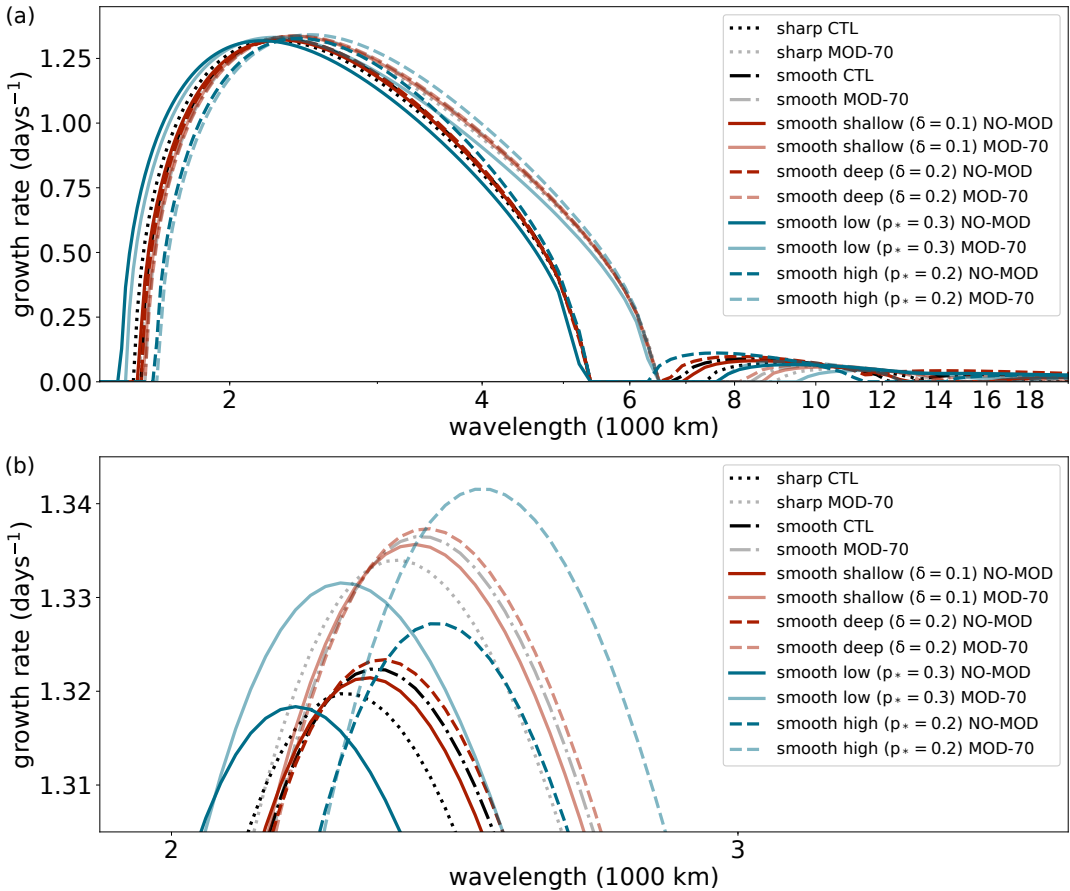+2.4% [+4.9%] instead of -10.2% and +14.2%.

19

Figure 10. Same as Fig. 6 but including latent heating with $\varepsilon = 2$.

All aforementioned changes associated to the intensity of the diabatic heating are larger than the relative changes in growth rate for the various tropopause smoothing experiments for a fixed $\varepsilon = 2$ (middle row in Fig. 12), which range between -0.2% and +1.7%. Moreover, these findings remain similar when using smooth vertical profiles of latent heating as in Haualand and Spengler (2019) (see their Fig. 11a), with the relative change in growth rate being between -5.0% and +3.0% when changing the latent heating intensity ε by 5% (not shown). Again, these numbers are all larger than the change in growth rate relative to the experiment with the discontinuous profiles for a fixed $\varepsilon = 2$, which are between -2.1 and +1.9% when using a smooth
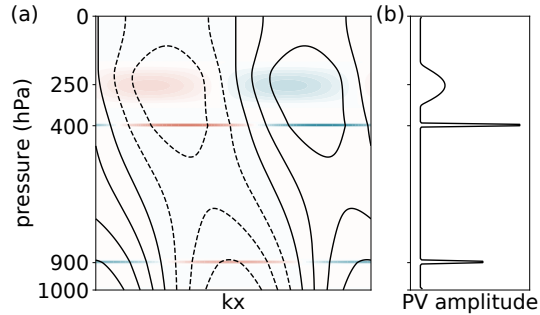
405

20

Figure 11. (a) Structure of interior PV (shading) and ψ (contours) for the most unstable mode of the default smooth experiment including latent heating and (b) amplitude of interior PV anomalies. Values are not comparable to physical values due to normalisation constraint mentioned in Sect. 2.1.

heating profile. With such a high sensitivity of the forecast error to heating intensity, our results indicate that it is much more important to adequately represent diabatic processes than the sharpness of the tropopause.

5 Conclusions

410   Including sharp and smooth transitions of vertical wind shear and stratification across a finite tropopause in a linear QG model extended from the Eady (1949) model, we investigated the relative importance of changes across the tropopause region at different degrees of smoothing on baroclinic development and compared its sensitivity to that of diabatic heating. We found that impacts related to tropopause structure are secondary to diabatic heating related to mid-tropospheric latent heating.

In contrast to the Eady mode, where the tropopause is represented by a rigid lid, the inclusion of an idealised tropopause with
415   abrupt changes in wind shear and/or stratification introduces nonzero vertical motion at the tropopause. The vertical motion leads to adiabatic cooling/warming at the tropopause, which opposes the effect of meridional temperature advection. The adiabatic cooling/warming weakens the amplitude of the wave at the tropopause but accelerates its downstream propagation, resulting in weaker growth rates and higher phase speed than the most unstable Eady mode.

In agreement with the dispersion relation for Rossby waves, increasing (decreasing) $\partial \overline{q}/\partial y$ at the tropopause by varying
420   the stratospheric wind shear and/or stratification is associated with relatively weak (strong) phase speed and short (long) wavelength. In contrast to wavelength and phase speed, the impact from wind shear and stratification on the growth rate is less straight forward, with growth rates being strongest when wind shear is uniform and the increase in stratification is large across the tropopause. The strong growth rates are related to a beneficial phase relation between meridional wind and temperature near the tropopause, which is associated with enhanced conversion of basic-state available potential energy to eddy available
425   potential energy. Thus, baroclinic growth is not strongest when the tropopause is sharpest.
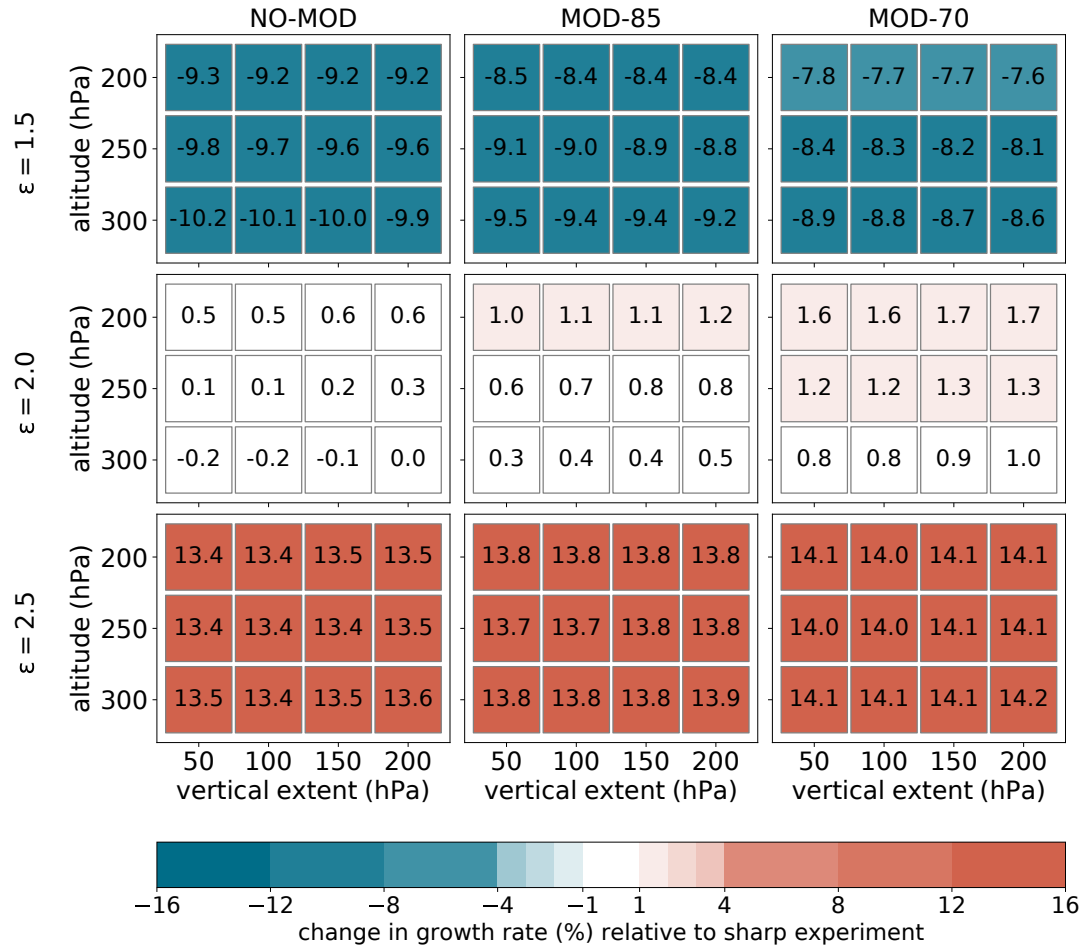
Figure 12. Same as Fig. 8, but including latent heating for three different heating intensity parameters ($\varepsilon = 1.5, 2.0, 2.5$). Note that the colorbar is extended from the one in Fig. 12 but contains the same colours at lower values.

Smoothing the tropopause is associated with a positive effect on baroclinic growth related to a further enhancement of energy conversion through an improved phase relation between meridional wind and temperature, as well as a negative effect related to a weaker maximum gradient of $\partial \overline{q}/\partial y$ in the tropopause region. The positive effect from smoothing dominates when there are no or small changes in wind shear and large changes in stratification across the tropopause, resulting in increased growth rates compared to when the tropopause is sharp. In contrast, the negative effect dominates when there are large changes in

22

wind shear and no or small changes in stratification, yielding weaker growth rates than for a sharp tropopause. For the most realistic configuration, with large changes in both wind shear and stratification across the tropopause, these opposing effects balance each other, resulting in negligible changes in growth rate from smoothing, suggesting that baroclinic growth is not very sensitive to tropopause sharpness.

435   The effect of smoothing for a realistic configuration of wind shear and stratification remains weak when increasing the vertical extent of smoothing and altering the tropopause altitude, with an error growth for exponentially growing quantities of less than 2% in a medium-range forecast of 5 days. In contrast, modifying the wind shear and stratification above the tropopause, resulting in modifications in vertical integral of the PV gradient relative to a sharp control experiment, has a much more pronounced effect on baroclinic growth than the effects related to smoothing and varying tropopause altitude.

440 The associated exponentially growing forecast error of any wave amplitude assuming perfect initial conditions is 17% in a medium-range forecast of 5 days when the stratospheric wind shear divided by stratification is reduced to 70% of its original value, which is a reduction actually occurring in operational numerical weather prediction models (Schäfler et al., 2020). The relatively large sensitivity to the lower stratospheric winds on baroclinic development is in line with Rupp and Birner (2021), who also argued that baroclinic growth may be sensitive to modifications in the horizontal PV gradients.

445   Although the relative impact on baroclinic growth depends on how much the profiles of wind shear and stratification are altered for the different sensitivity experiments, our estimates indicate that it is much more important to maintain the vertical integral of the PV gradient than to accurately represent the abrupt vertical contrasts across the tropopause. Such modifications above the tropopause may represent modelling challenges related to observational errors, vertical resolution, a low model lid, or limitations related to data assimilation techniques, but they can also represent changes in the lower stratospheric winds

450 resulting from downward extensions of a weak polar vortex after a sudden stratopheric warming event.

    As expected from the strong impact of diabatic heating on baroclinic development, including mid-tropospheric latent heating of moderate intensity increases the growth rate. However, including latent heating does not alter the qualitative findings regarding the impact of tropopause structure on baroclinic development. Nevertheless, modifying the heating intensity by 5-25% has a significantly larger impact on the growth rate than the effects of smoothing tropopause structure, varying tropopause altitude,

455 and maintaining the vertical integral of the PV gradient. This highlights the main finding of this study that baroclinic growth is more sensitive to diabatic heating than tropopause structure.

    While this study is the first to quantify the relative effect of tropopause sharpness and latent heating on baroclinic development, it is important to keep in mind the highly idealised character of this study. More realistic simulations with numerical weather prediction models should be performed to test our findings and to further clarify the relative importance of the repre-

460 sentation of the tropopause and diabatic forcing on midlatitude cyclones.

Code availability. The current version of the model code is available on https://github.com/krifla/2dQGnum/tree/v1.0.0. A digital object identifier (DOI) will be provided if this work gets published in WCD.

Author contributions. KFH and TS designed the experiments and KFH carried them out. KFH developed the model code, and KFH and TS analysed the model output. KFH prepared the manuscript with support from TS.

465   *Competing interests.* The authors declare that they have no conflict of interest.

References

470   Asselin, O., Bartello, P., and Straub, D. N.: On quasigeostrophic dynamics near the tropopause, Phys. Fluids, 28, 026 601, https://doi.org/10.1063/1.4941761, 2016.

Balasubramanian, G. and Yau, M.: The life cycle of a simulated marine cyclone: Energetics and PV diagnostics, J. Atmos. Sci., 53, 639–653, https://doi.org/10.1175/1520-0469(1996)053<0639:TLCOAS>2.0.CO;2, 1996.

Baldwin, M. P. and Dunkerton, T. J.: Stratospheric harbingers of anomalous weather regimes, Science, 294, 581–584,
475   https://doi.org/10.1126/science.1063315, 2001.

Beare, R. J., Thorpe, A. J., and White, A. A.: The predictability of extratropical cyclones: Nonlinear sensitivity to localized potential-vorticity perturbations, Quart. J. Roy. Meteor. Soc., 129, 219–237, https://doi.org/10.1256/qj.02.15, 2003.

Birner, T.: Fine-scale structure of the extratropical tropopause region, J. Geophys. Res., 111, https://doi.org/10.1029/2005JD006301, 2006.

Birner, T., Dörnbrack, A., and Schumann, U.: How sharp is the tropopause at midlatitudes?, Geophys. Res. Lett., 29, 45–1,
480   https://doi.org/10.1029/2002GL015142, 2002.

Birner, T., Sankey, D., and Shepherd, T.: The tropopause inversion layer in models and analyses, Geophys. Res. Lett., 33, https://doi.org/10.1029/2006GL026549, 2006.

Blumen, W.: On short-wave baroclinic instability, J. Atmos. Sci., 36, 1925–1933, https://doi.org/10.1175/1520-0469(1979)036<1925:OSWBI>2.0.CO;2, 1979.

485   Bretherton, F. P.: Baroclinic instability and the short wavelength cut-off in terms of potential instability, Quart. J. Roy. Meteor. Soc., 92, 335–345, https://doi.org/10.1002/qj.49709239303, 1966.

Butler, A. H., Arribas, A., Athanassiadou, M., Baehr, J., Calvo, N., Charlton-Perez, A., Déqué, M., Domeisen, D. I., Fröhlich, K., Hendon, H., et al.: The Climate-system Historical Forecast Project: do stratosphere-resolving models make better seasonal climate predictions in boreal winter?, Quarterly Journal of the Royal Meteorological Society, 142, 1413–1427, https://doi.org/10.1002/qj.2743, 2016.

490   Charlton-Perez, A. J., Baldwin, M. P., Birner, T., Black, R. X., Butler, A. H., Calvo, N., Davis, N. A., Gerber, E. P., Gillett, N., Hardiman, S., et al.: On the lack of stratospheric dynamical variability in low-top versions of the CMIP5 models, J. Geophys. Res., 118, 2494–2505, https://doi.org/10.1002/jgrd.50125, 2013.

Charron, M.: The Stratospheric Extension of the Canadian Global Deterministic Medium-Range Weather Forecasting System and Its Impact on Tropospheric Forecasts, Mon. Wea. Rev., 140, 1924–1944, https://doi.org/10.1175/MWR-D-11-00097.1, 2012.

495   Craig, G. and Cho, H.-R.: Cumulus heating and CISK in the extratropical atmosphere. Part I: Polar lows and comma clouds, J. Atmos. Sci., 45, 2622–2640, https://doi.org/10.1175/1520-0469(1988)045<2622:CHACIT>2.0.CO;2, 1988.

de Vries, H. and Opsteegh, T.: Interpretation of discrete and continuum modes in a two-layer Eady model, Tellus, 59, 182–197, https://doi.org/10.1111/j.1600-0870.2006.00219.x, 2007.

de Vries, H., Methven, J., Frame, T. H., and Hoskins, B. J.: Baroclinic waves with parameterized effects of moisture interpreted using Rossby
500   wave components, J. Atmos. Sci., 67, 2766–2784, https://doi.org/10.1175/2010JAS3410.1, 2010.

Dirren, S., Didone, M., and Davies, H. C.: Diagnosis of forecast-analysis differences of a weather prediction system, Geophys. Res. Lett., 30, 2060–2063, https://doi.org/10.1029/2003GL017986, 2003.

Eady, E. T.: Long-waves and cyclone waves, Tellus, 1, 33–52, https://doi.org/10.1111/j.2153-3490.1949.tb01265.x, 1949.

Egger, J.: Tropopause height in baroclinic channel flow, J. Atmos. Sci., 52, 2232–2241, https://doi.org/10.1175/1520-
505   0469(1995)052<2232:THIBCF>2.0.CO;2, 1995.

Emanuel, K. A., Fantini, M., and Thorpe, A. J.: Baroclinic instability in an environment of small stability to slantwise moist convection. Part I: Two-dimensional models, J. Atmos. Sci., 44, 1559–1573, https://doi.org/10.1175/1520-0469(1987)044<1559:BIIAEO>2.0.CO;2, 1987.

Gettelman, A. and Wang, T.: Structural diagnostics of the tropopause inversion layer and its evolution, Journal of Geophysical Research: Atmospheres, 120, 46–62, https://doi.org/10.1002/2014JD021846, 2015.

Gray, S. L., Dunning, C. M., Methven, J., Masato, G., and Chagnon, J. M.: Systematic model forecast error in Rossby wave structure, Geophys. Res. Lett., 41, 2979–2987, https://doi.org/10.1002/2014GL059282.Received, 2014.

Grise, K. M., Thompson, D. W., and Birner, T.: A global survey of static stability in the stratosphere and upper troposphere, J. Climate, 23, 2275–2292, https://doi.org/10.1175/2009JCLI3369.1, 2010.

Hakim, G. J.: Vertical structure of midlatitude analysis and forecast errors, Mon. Wea. Rev., 133, 567–578, https://doi.org/10.1175/MWR-2882.1, 2005.

Hamill, T. M., Snyder, C., and Whitaker, J. S.: Ensemble Forecasts and the Properties of Flow-Dependent Analysis-Error Covariance Singular Vectors, Mon. Wea. Rev., 131, 1741–1758, https://doi.org/10.1175//2559.1, 2003.

Hardiman, S., Butchart, N., Hinton, T., Osprey, S., and Gray, L.: The effect of a well-resolved stratosphere on surface climate: Differences between CMIP5 simulations with high and low top versions of the Met Office climate model, J. Climate, 25, 7083–7099, https://doi.org/10.1175/JCLI-D-11-00579.1, 2012.

Harnik, N. and Lindzen, R. S.: The effect of basic-state potential vorticity gradients on the growth of baroclinic waves and the height of the tropopause, J. Atmos. Sci., 55, 344–360, https://doi.org/10.1175/1520-0469(1998)055<0344:TEOBSP>2.0.CO;2, 1998.

Haualand, K. F. and Spengler, T.: How does latent cooling affect baroclinic development in an idealized framework?, J. Atmos. Sci., 76, 2701–2714, https://doi.org/10.1175/JAS-D-18-0372.1, 2019.

Haualand, K. F. and Spengler, T.: Direct and Indirect Effects of Surface Fluxes on Moist Baroclinic Development in an Idealized Framework, J. Atmos. Sci., 77, 3211–3225, https://doi.org/10.1175/JAS-D-19-0328.1, 2020.

Hoskins, B., McIntyre, M., and Robertson, W.: On the use and significance of isentropic potential vorticity maps, Quart. J. Roy. Meteor. Soc., 111, 877–946, https://doi.org/10.1002/qj.49711147002, 1985.

Houchi, K., Stoffelen, A., Marseille, G., and De Kloe, J.: Comparison of wind and wind shear climatologies derived from high-resolution radiosondes and the ECMWF model, J. Geophys. Res., 115, https://doi.org/10.1029/2009JD013196, 2010.

Juckes, M.: Quasigeostrophic dynamics of the tropopause, J. Atmos. Sci., 51, 2756–2768, https://doi.org/10.1175/1520-0469(1994)051<2756:QDOTT>2.0.CO;2, 1994.

Kawatani, Y., Hamilton, K., Gray, L. J., Osprey, S. M., Watanabe, S., and Yamashita, Y.: The effects of a well-resolved stratosphere on the simulated boreal winter circulation in a climate model, J. Atmos. Sci., 76, 1203–1226, https://doi.org/10.1175/JAS-D-18-0206.1, 2019.

Kidston, J., Scaife, A. A., Hardiman, S. C., Mitchell, D. M., Butchart, N., Baldwin, M. P., and Gray, L. J.: Stratospheric influence on tropospheric jet streams, storm tracks and surface weather, Nature Geoscience, 8, 433–440, https://doi.org/10.1038/NGEO2424, 2015.

Lindzen, R. and Farrell, B.: A simple approximate result for the maximum growth rate of baroclinic instabilities, J. Atmos. Sci., 37, 1648–1654, https://doi.org/10.1175/1520-0469(1980)037<1648:ASARFT>2.0.CO;2, 1980.

Lorenz, E. N.: Available potential energy and the maintenance of the general circulation, Tellus, 7, 157–167, https://doi.org/10.1111/j.2153-3490.1955.tb01148.x, 1955.

Mak, M.: Cyclogenesis in a conditionally unstable moist baroclinic atmosphere, Tellus, 46A, 14–33, https://doi.org/10.3402/tellusa.v46i1.15424, 1994.

Mak, M.: Influence of Surface Sensible Heat Flux on Incipient Marine Cyclogenesis, J. Atmos. Sci., 55, 820–834,
545   https://doi.org/10.1175/1520-0469(1998)055<0820:IOSSHF>2.0.CO;2, 1998.

Manabe, S.: On the contribution of heat released by condensation to the change in pressure pattern, J. Met. Soc. Japan, 34, 308–320,
       https://doi.org/10.2151/jmsj1923.34.6_308, 1956.

Marshall, A. G. and Scaife, A. A.: Improved predictability of stratospheric sudden warming events in an atmospheric general circulation
       model with enhanced stratospheric resolution, J. Geophys. Res., 115, https://doi.org/10, 2010.

550   Martínez-Alvarado, O., Madonna, E., Gray, S. L., and Joos, H.: A route to systematic error in forecasts of Rossby waves, Quarterly Journal
       of the Royal Meteorological Society, 142, 196–210, https://doi.org/10.1002/qj.2645, 2016.

Moore, R. W. and Montgomery, M. T.: Reexamining the dynamics of short-scale, diabatic Rossby waves and their role in midlatitude moist
       cyclogenesis, J. Atmos. Sci., 61, 754–768, https://doi.org/10.1175/1520-0469(2004)061<0754:RTDOSD>2.0.CO;2, 2004.

Müller, J. C.: Baroclinic instability in a two-layer, vertically semi-infinite domain, Tellus, 43, 275–284, https://doi.org/10.1034/j.1600-
555   0870.1991.t01-4-00003.x, 1991.

Osprey, S. M., Gray, L. J., Hardiman, S. C., Butchart, N., and Hinton, T. J.: Stratospheric variability in twentieth-century CMIP5 simulations
       of the Met Office climate model: High top versus low top, J. Climate, 26, 1595–1606, https://doi.org/10.1175/JCLI-D-12-00147.1, 2013.

Pilch Kedzierski, R., Neef, L., and Matthes, K.: Tropopause sharpening by data assimilation, Geophys. Res. Lett., 43, 8298–8305,
       https://doi.org/10.1002/2016GL069936, 2016.

560   Plougonven, R. and Vanneste, J.: Quasi-geostrophic dynamics of a finite-depth tropopause, J. Atmos. Sci., 67, 1–23,
       https://doi.org/10.1175/2010JAS3502.1, 2010.

Rivest, C., Davis, C., and Farrell, B.: Upper-tropospheric synoptic-scale waves. Part I: Maintenance as Eady normal modes., J. Atmos. Sci.,
       49, 2108–2119, https://doi.org/10.1175/1520-0469(1992)049<2108:UTSSWP>2.0.CO;2, 1992.

Robinson, W. A.: On the structure of potential vorticity in baroclinic instability, Tellus, 41, 275–284, https://doi.org/10.1111/j.1600-
565   0870.1989.tb00382.x, 1989.

Rupp, P. and Birner, T.: Tropospheric eddy feedback to different stratospheric conditions in idealised baroclinic life cycles, Weather and
       Climate Dynamics, 2, 111–128, https://doi.org/10.5194/wcd-2-111-2021, 2021.

Saffin, L., Gray, S. L., Methven, J., and Williams, K. D.: Processes Maintaining Tropopause Sharpness in Numerical Models, J. Geophys.
       Res., 122, 9611–9627, https://doi.org/10.1002/2017JD026879, 2017.

570   Schäfler, A., Craig, G., Wernli, H., Arbogast, P., Doyle, J. D., Mctaggart-Cowan, R., Methven, J., Rivière, G., Ament, F., Boettcher, M.,
       Bramberger, M., Cazenave, Q., Cotton, R., Crewell, S., Delanoë, J., DörnbrAck, A., Ehrlich, A., Ewald, F., Fix, A., Grams, C. M., Gray,
       S. L., Grob, H., Groß, S., Hagen, M., Harvey, B., Hirsch, L., JAcob, M., Kölling, T., Konow, H., Lemmerz, C., Lux, O., Magnusson,
       L., Mayer, B., Mech, M., Moore, R., Pelon, J., Quinting, J., Rahm, S., Rapp, M., Rautenhaus, M., Reitebuch, O., Reynolds, C. A.,
       Sodemann, H., Spengler, T., Vaughan, G., Wendisch, M., Wirth, M., Witschas, B., Wolf, K., and Zinner, T.: The north atlantic waveguide
575   and downstream impact experiment, Bull. Amer. Meteor. Soc., 99, 1607–1637, https://doi.org/10.1175/BAMS-D-17-0003.1, 2018.

Schäfler, A., Harvey, B., Methven, J., Doyle, J. D., Rahm, S., Reitebuch, O., Weiler, F., and Witschas, B.: Observation of jet
       stream winds during NAWDEX and characterization of systematic meteorological analysis errors, Mon. Wea. Rev., 148, 2889–2907,
       https://doi.org/10.1175/MWR-D-19-0229.1, 2020.

Snyder, C. and Lindzen, R. S.: Quasi-geostrophic wave-CISK in an unbounded baroclinic shear, J. Atmos. Sci., 48, 76–86,
580   https://doi.org/10.1175/1520-0469(1991)048<0076:QGWCIA>2.0.CO;2, 1991.

27

Wirth, V., Riemer, M., Chang, E. K., and Martius, O.: Rossby wave packets on the midlatitude waveguide—A review, Mon. Wea. Rev., 146, 1965–2001, https://doi.org/10.1175/MWR-D-16-0483.1, 2018.

Wittman, M., Charlton, A., and Polvani, L.: The effect of lower stratospheric shear on baroclinic instability., J. Atmos. Sci., 64, 479–496, https://doi.org/10.1175/JAS3828.1, 2007.

Bibliography

Ahmadi-Givi, F., G. Graig, and R. Plant (2004), The dynamics of a midlatitude cyclone with very strong latent-heat release, *Quart. J. Roy. Meteor. Soc.*, *130*, 295–323. 1.3

Bala, G., K. Caldeira, and R. Nemani (2010), Fast versus slow response in climate change: implications for the global hydrological cycle, *Climate Dyn.*, *35*(2-3), 423–434, doi:10.1007/s00382-009-0583-y. 5

Balasubramanian, G., and M. Yau (1996), The life cycle of a simulated marine cyclone: Energetics and PV diagnostics, *J. Atmos. Sci.*, *53*, 639–653, doi:10.1175/1520-0469(1996)053<0639:TLCOAS>2.0.CO;2. 1.3, 2

Baldwin, M. P., and T. J. Dunkerton (2001), Stratospheric harbingers of anomalous weather regimes, *Science*, *294*, 581–584, doi:10.1126/science.1063315. 1.4

Barth, M. C., and D. B. Parsons (1996), Microphysical processes associated with intense frontal rainbands and the effect of evaporation and melting on frontal dynamics, *J. Atmos. Sci.*, *53*(11), 1569–1586. 2

Beare, R. J., A. J. Thorpe, and A. A. White (2003), The predictability of extratropical cyclones: Nonlinear sensitivity to localized potential-vorticity perturbations, *Quart. J. Roy. Meteor. Soc.*, *129*, 219–237, doi:10.1256/qj.02.15. 1.3

Bengtsson, L., K. I. Hodges, and N. Keenlyside (2009), Will extratropical storms intensify in a warmer climate?, *J. Climate*, *22*(9), 2276–2301, doi:10.1175/2008JCLI2678.1. 5

Birner, T., D. Sankey, and T. Shepherd (2006), The tropopause inversion layer in models and analyses, *Geophys. Res. Lett.*, *33*(14), doi:10.1029/2006GL026549. 1.4, 2

Bjerknes, J. (1919), On the structure of moving cyclones, *Mon. Wea. Rev.*, pp. 95–99. 1.2

Bjerknes, J., and H. Solberg (1922), Life cycle of cyclones and the polar front theory of atmospheric circulation, *Geofys. Publikasjoner*, *3*, 1. 1.2

Boer, G. (1993), Climate change and the regulation of the surface moisture and energy budgets, *Climate Dyn.*, *8*(5), 225–239, doi:10.1007/BF00198617. 5

Boutle, I., R. Beare, S. Belcher, A. Brown, and R. Plant (2010), The moist boundary layer under a mid-latitude weather system, *Bound.-Lay. Meteorol.*, *134*, 367–386, doi:10.1007/s10546-009-9452-9. 1.3, 3.2

Branscome, L. E., W. J. Gutowski Jr, and D. A. Stewart (1989), Effect of surface fluxes on the nonlinear development of baroclinic waves, *J. Atmos. Sci.*, *46*(4), 460–475, doi:10.1175/1520-0469(1989)046<0460:EOSFOT>2.0.CO;2. 1.3

Bretherton, F. P. (1966), Baroclinic instability and the short wavelength cut-off in terms of potential instability, *Quart. J. Roy. Meteor. Soc.*, *92*, 335–345, doi:10.1002/qj.49709239303. 1.2

Browning, K. A. (1990), Organization of clouds and precipitation in extratropical cyclones, in *Extratropical Cyclones: Erik Palmén Memorial Volume*, edited by C. W. Newton and E. O. Holopainen, pp. 129–153, Amer. Meteor. Soc. 1.3, 2

Bui, H., and T. Spengler (2021), On the influence of sea surface temperature distributions on the development of extratropical cyclones, *J. Atmos. Sci.* Advance online publication. doi:10.1175/JAS-D-20-0137.1. 1.3, 5

Butler, A. H., D. W. Thompson, and R. Heikes (2010), The steady-state atmospheric circulation response to climate change–like thermal forcings in a simple general circulation model, *J. Climate*, *23*(13), 3474–3496, doi:10.1175/2010JCLI3228.1. 5

Carrera, M. L., J. R. Gyakum, and D.-L. Zhang (1999), A numerical case study of secondary marine cyclogenesis sensitivity to initial error and varying physical processes, *Mon. Wea. Rev.*, *127*(5), 641–660, doi:10.1175/1520-0493(1999)127<0641:ANCSOS>2.0.CO;2. 1.3, 2

Catto, J. L., L. C. Shaffrey, and K. I. Hodges (2011), Northern hemisphere extratropical cyclones in a warming climate in the higem high-resolution climate model, *J. Climate*, *24*(20), 5336–5352, doi:10.1175/2011JCLI4181.1. 5

Catto, J. L., D. Ackerley, J. F. Booth, A. J. Champion, B. A. Colle, S. Pfahl, J. G. Pinto, J. F. Quinting, and C. Seiler (2019), The future of midlatitude cyclones, *Curr. Clim. Change Rep.*, *5*(4), 407–420, doi:10.1007/s40641-019-00149-4. 5

Chang, E., S. Lee, and K. Swanson (2002), Storm track dynamics, *J. Climate*, *15*(16), 2163–2183, doi:10.1175/1520-0442(2002)015<02163:STD>2.0.CO;2. 1.1

Charney, J. G. (1947), The dynamics of long waves in a baroclinic westerly current, *J. Meteor.*, *4*, 135–162. 1.2

Clough, S., and R. Franks (1991), The evaporation of frontal and other stratiform precipitation, *Quart. J. Roy. Meteor. Soc.*, *117*, 1057–1080. 2

Collins, M., R. Knutti, J. Arblaster, J.-L. Dufresne, T. Fichefet, P. Friedlingstein, X. Gao, W. J. Gutowski, T. Johns, G. Krinner, et al. (2013), Long-term climate change: projections, commitments and irreversibility, in *Climate Change 2013-The Physical Science Basis: Contribution of Working Group I to the Fifth Assessment Report of the Intergovernmental Panel on Climate Change*, pp. 1029–1136, Cambridge University Press. 5

Craig, G., and H.-R. Cho (1988), Cumulus heating and CISK in the extratropical atmosphere. Part I: Polar lows and comma clouds, *J. Atmos. Sci.*, *45*, 2622–2640, doi:10.1175/1520-0469(1988)045<2622:CHACIT>2.0.CO;2. 1.3, 2

Crezee, B., H. Joos, and H. Wernli (2017), The microphysical building blocks of low-level potential vorticity anomalies in an idealized extratropical cyclone, *J. Atmos. Sci.*, *74*(5), 1403–1416. 1.3, 2

Dacre, H. F., O. Martinez-Alvarado, and C. O. Mbengue (2019), Linking atmospheric rivers and warm conveyor belt airflows, *J. Hydrometeorol.*, *20*(6), 1183–1196, doi: 10.1175/JHM-D-18-0175.1. 1.3

Davies, H. C., and C. H. Bishop (1994), Eady edge waves and rapid development, *J. Atmos. Sci.*, *51*(13), 1930–1946. 1.2, 3.1

Davis, C., and K. Emanuel (1991), Potential vorticity diagnostics of cyclogenesis, *J. Atmos. Sci.*, *119*, 1929–1953. 1.3

Davis, C., M. T. Stoelinga, and Y.-H. Kuo (1993), The integrated effect of condensation in numerical simulations of extratropical cyclogenesis, *Mon. Wea. Rev.*, *121*, 2309–2330. 1.3

de Vries, H., J. Methven, T. H. Frame, and B. J. Hoskins (2010), Baroclinic waves with parameterized effects of moisture interpreted using Rossby wave components, *J. Atmos. Sci.*, *67*(9), 2766–2784, doi:10.1175/2010JAS3410.1. 1.2, 1.3

Dirren, S., M. Didone, and H. C. Davies (2003), Diagnosis of forecast-analysis differences of a weather prediction system, *Geophys. Res. Lett.*, *30*, 2060–2063, doi: 10.1029/2003GL017986. 2

Eady, E. T. (1949), Long-waves and cyclone waves, *Tellus*, *1*(3), 33–52, doi:10.1111/j. 2153-3490.1949.tb01265.x. 1.2, 1.2, 3.1

Emanuel, K. A., M. Fantini, and A. J. Thorpe (1987), Baroclinic instability in an environment of small stability to slantwise moist convection. Part I: Two-dimensional models, *J. Atmos. Sci.*, *44*, 1559–1573, doi:10.1175/1520-0469(1987)044<1559: BIIAEO>2.0.CO;2. 1.3

Fläschner, D., T. Mauritsen, and B. Stevens (2016), Understanding the intermodel spread in global-mean hydrological sensitivity, *J. Climate*, *29*(2), 801–817, doi: 10.1175/JCLI-D-15-0351.1. 5

Geng, Q., and M. Sugi (2003), Possible change of extratropical cyclone activity due to enhanced greenhouse gases and sulfate aerosols study with a high-resolution AGCM, *J. Climate*, *16*, 2262–2274. 5

Gray, S. L., C. M. Dunning, J. Methven, G. Masato, and J. M. Chagnon (2014), Systematic model forecast error in Rossby wave structure, *Geophys. Res. Lett.*, *41*(8), 2979–2987, doi:10.1002/2014GL059282.Received. 1.4, 2

Gyakum, J. R., and R. E. Danielson (2000), Analysis of meteorological precursors to ordinary and explosive cyclogenesis in the western North Pacific, *Mon. Wea. Rev.*, *128*(3), 851–863, doi:10.1175/1520-0493(2000)128<0851:AOMPTO>2.0.CO;2. 2

Hakim, G. J. (2005), Vertical structure of midlatitude analysis and forecast errors, *Mon. Wea. Rev.*, *133*(3), 567–578, doi:10.1175/MWR-2882.1. 1.4, 2

Hamill, T. M., C. Snyder, and J. S. Whitaker (2003), Ensemble forecasts and the properties of flow-dependent analysis-error covariance singular vectors, *Mon. Wea. Rev.*, *131*(February), 1741–1758, doi:10.1175//2559.1. 2

Hartmann, D. L. (1994), *Global physical climatology*, vol. 56, 138 pp., Academic Press. 1.1

Held, I. M. (1993), Large-scale dynamics and global warming, *Bull. Amer. Meteor. Soc.*, *74*(2), 228–242, doi:10.1175/1520-0477(1993)074<0228:LSDAGW>2.0.CO;2. 5

Hirata, H., R. Kawamura, M. Nonaka, and K. Tsuboki (2019), Significant impact of heat supply from the Gulf Stream on a "superbomb" cyclone in January 2018, *Geophys. Res. Lett.*, *46*, doi:10.1029/2019GL082995. 2

Hoskins, B., M. McIntyre, and W. Robertson (1985), On the use and significance of isentropic potential vorticity maps, *Quart. J. Roy. Meteor. Soc.*, *111*, 877–946, doi: 10.1002/qj.49711147002. 1.2

Huang, H.-C., and K. A. Emanuel (1991), The effects of evaporation on frontal circulations, *J. Atmos. Sci.*, *48*(4), 619–628. 2

Jiang, W., and W. J. Gutowski (2000), Moist baroclinic instability in the presence of surface-atmosphere coupling, *J. Atmos. Sci.*, *57*(17), 2923–2935, doi:10.1175/ 1520-0469(2000)057<2923:MBIITP>2.0.CO;2. 2

Joos, H., and H. Wernli (2012), Influence of microphysical processes on the potential vorticity development in a warm conveyor belt: a case-study with the limited-area model COSMO, *Quart. J. Roy. Meteor. Soc.*, *138*(663), 407–418. 1.3, 2

Kuo, Y.-H., and R. J. Reed (1988), Numerical simulation of an explosively deepening cyclone in the eastern Pacific, *Mon. Wea. Rev.*, *116*(10), 2081–2105, doi:10.1175/ 1520-0493(1988)116<2081:NSOAED>2.0.CO;2. 2

Kuo, Y.-H., R. J. Reed, and S. Low-Nam (1991a), Effects of surface energy fluxes during the early development and rapid intensification stages of seven explosive cyclones in the western Atlantic, *Mon. Wea. Rev.*, *119*, 457–476, doi:10.1175/ 1520-0493(1991)119<0457:EOSEFD>2.0.CO;2. 2

Kuo, Y.-H., M. Shapiro, and E. G. Donall (1991b), The interaction between baroclinic and diabatic processes in a numerical simulation of a rapidly intensifying extratropical marine cyclone, *Mon. Wea. Rev.*, *119*, 368–384, doi:10.1175/1520-0493(1991) 119<0368:TIBBAD>2.0.CO;2. 2

Langland, R., R. Elsberry, and R. Errico (1995), Evaluation of physical processes in an idealized extratropical cyclone using adjoint techniques, *Quart. J. Roy. Meteor. Soc.*, *121*, 1349–1386, doi:10.1002/qj.49712152608. 2

Large, W., and S. Yeager (2012), On the observed trends and changes in global sea surface temperature and air–sea heat fluxes (1984–2006), *J. Climate*, *25*(18), 6123– 6135, doi:10.1175/JCLI-D-11-00148.1. 5

Lin, S. C., and P. J. Smith (1979), Diabatic heating and generation of available potential energy in a tornado-producing extratropical cyclone, *Mon. Wea. Rev.*, *107*(9), 1169–1183, doi:10.1175/1520-0493(1979)107<1169:dhagoa>2.0.co;2. 1.3

Lorenz, E. N. (1955), Available potential energy and the maintenance of the general circulation, *Tellus*, *7*, 157–167, doi:10.1111/j.2153-3490.1955.tb01148.x. 1.1, 3.5

Mak, M. (1994), Cyclogenesis in a conditionally unstable moist baroclinic atmosphere, *Tellus*, *46A*, 14–33, doi:10.3402/tellusa.v46i1.15424. 3.2

Mak, M. (1998), Influence of surface sensible heat flux on incipient marine cyclogenesis, *J. Atmos. Sci.*, *55*, 820–834, doi:10.1175/1520-0469(1998)055<0820:IOSSHF>2.0.CO;2. 3.2

Manabe, S. (1956), On the contribution of heat released by condensation to the change in pressure pattern, *J. Met. Soc. Japan*, *34*(6), 308–320, doi:10.2151/jmsj1923.34.6_308. 1.3

Martínez-Alvarado, O., F. Weidle, and S. L. Gray (2010), Sting jets in simulations of a real cyclone by two mesoscale models, *Mon. Wea. Rev.*, *138*, 4054–4075. 2

Martínez-Alvarado, O., E. Madonna, S. L. Gray, and H. Joos (2016), A route to systematic error in forecasts of Rossby waves, *Quart. J. Roy. Meteor. Soc.*, *142*(694), 196–210, doi:10.1002/qj.2645. 1.3

Moore, R. W., and M. T. Montgomery (2004), Reexamining the dynamics of short-scale, diabatic Rossby waves and their role in midlatitude moist cyclogenesis, *J. Atmos. Sci.*, *61*, 754–768, doi:10.1175/1520-0469(2004)061<0754:RTDOSD>2.0.CO;2. 1.3

Mullen, S. L., and D. P. Baumhefner (1988), Sensitivity of numerical simulations of explosive oceanic cyclogenesis to changes in physical parameterizations, *Mon. Wea. Rev.*, *116*(11), 2289–2329, doi:10.1175/1520-0493(1988)116<2289:SONSOE>2.0.CO;2. 2

Nuss, W. A., and R. A. Anthes (1987), A numerical investigation of low-level processes in rapid cyclogenesis, *Mon. Wea. Rev.*, *115*, 2728–2743, doi:10.1175/1520-0493(1987)115<2728:ANIOLL>2.0.CO;2. 2

Parker, D. J., and A. J. Thorpe (1995), Conditional convective heating in a baroclinic atmosphere: a model of convective frontogenesis, *J. Atmos. Sci.*, *52*, 1699–1711. 2

Pfahl, S., E. Madonna, M. Boettcher, H. Joos, and H. Wernli (2014), Warm conveyor belts in the ERA-Interim dataset (1979-2010). Part II: moisture origin and relevance for precipitation, *J. Climate*, *27*, doi:10.1175/JCLI-D-13-00223.1. 1.3

Räisänen, J. (2003), CO2-induced changes in atmospheric angular momentum in CMIP2 experiments, *J. Climate*, *16*(1), 132–143, doi:10.1175/1520-0442(2003)016<0132:CICIAA>2.0.CO;2. 5

Robertson, F., and P. Smith (1983), The impact of model moist processes on the energetics of extratropical cyclones, *Mon. Wea. Rev.*, *111*(4), 723–744. 1.3

Rupp, P., and T. Birner (2021), Tropospheric eddy feedback to different stratospheric conditions in idealised baroclinic life cycles, *Weather Clim. Dynam.*, *2*(1), 111–128, doi:10.5194/wcd-2-111-2021. 5

Saffin, L., S. L. Gray, J. Methven, and K. D. Williams (2017), Processes maintaining tropopause sharpness in numerical models, *J. Geophys. Res.*, *122*(18), 9611–9627, doi:10.1002/2017JD026879. 2

Schäfler, A., G. Craig, H. Wernli, P. Arbogast, J. D. Doyle, R. Mctaggart-Cowan, J. Methven, G. Rivière, F. Ament, M. Boettcher, M. Bramberger, Q. Cazenave, R. Cotton, S. Crewell, J. Delanoë, A. DörnbrAck, A. Ehrlich, F. Ewald, A. Fix, C. M. Grams, S. L. Gray, H. Grob, S. Groß, M. Hagen, B. Harvey, L. Hirsch, M. JAcob, T. Kölling, H. Konow, C. Lemmerz, O. Lux, L. Magnusson, B. Mayer, M. Mech, R. Moore, J. Pelon, J. Quinting, S. Rahm, M. Rapp, M. Rautenhaus, O. Reitebuch, C. A. Reynolds, H. Sodemann, T. Spengler, G. Vaughan, M. Wendisch, M. Wirth, B. Witschas, K. Wolf, and T. Zinner (2018), The North Atlantic Waveguide and Downstream Impact Experiment, *Bull. Amer. Meteor. Soc.*, *99*(8), 1607–1637, doi: 10.1175/BAMS-D-17-0003.1. 1.4

Schäfler, A., B. Harvey, J. Methven, J. D. Doyle, S. Rahm, O. Reitebuch, F. Weiler, and B. Witschas (2020), Observation of jet stream winds during NAWDEX and characterization of systematic meteorological analysis errors, *Mon. Wea. Rev.*, *148*(7), 2889–2907, doi:10.1175/MWR-D-19-0229.1. 1.4, 2

Schultz, D. M., and G. Vaughan (2011), Occluded fronts and the occlusion process: A fresh look at conventional wisdom, *Bull. Amer. Meteor. Soc.*, *92*(4), 443–466, doi: 10.1175/2010BAMS3057.1. 1.2

Schultz, D. M., L. F. Bosart, B. A. Colle, H. C. Davies, C. Dearden, D. Keyser, O. Martius, P. J. Roebber, W. J. Steenburgh, H. Volkert, et al. (2019), Extratropical cyclones: a century of research on meteorology's centerpiece, *Meteorol. Monogr.*, *59*, 16–1, doi:10.1175/amsmonographs-d-18-0015.1. 1.2

Shapiro, M., and D. Keyser (1990), Fronts, jet streams and the tropopause, in *Extratropical cyclones: the Erik Palmen memorial volume*, edited by C. Newton and E. Holopainen, chap. 10, pp. 167–191, American Meteorological Society, Boston, MA. 1.2

Smith, P. J. (1980), The energetics of extratropical cyclones, *Rev. Geophys.*, *18*(2), 378–386. 1.3

Snyder, C., and R. S. Lindzen (1991), Quasi-geostrophic wave-CISK in an unbounded baroclinic shear, *J. Atmos. Sci.*, *48*, 76–86, doi:10.1175/1520-0469(1991)048<0076: QGWCIA>2.0.CO;2. 1.3

Stoelinga, M. T. (1996), A potential vorticity based study of the role of diabatic heating and friction in a numerically simulated baroclinic cyclone, *Mon. Wea. Rev.*, pp. 849–874. 1.3

Uccellini, L. W., R. A. Petersen, K. F. Brill, P. J. Kocin, and J. J. Tuccillo (1987), Synergistic interactions between an upper-level jet streak and diabatic processes that influence the development of a low-level jet and a secondary coastal cyclone, *Mon. Wea. Rev.*, *115*, 2227–2261, doi:10.1175/1520-0493(1987)115<2227:SIBAUL>2.0. CO;2. 2

Vincent, D. G., G. B. Pant, and H. J. Edmon Jr (1977), Generation of available potential energy of an extratropical cyclone system, *Mon. Wea. Rev.*, *105*(10), 1252–1265. 1.3

Zhang, D.-L., E. Radeva, and J. Gyakum (1999), A family of frontal cyclones over the western Atlantic Ocean. Part II: Parameter studies, *Mon. Wea. Rev.*, *127*(8), 1745–1760, doi:10.1175/1520-0493(1999)127<1725:AFOFCO>2.0.CO;2. 1.3

Zhang, Y., and P. H. Stone (2011), Baroclinic adjustment in an atmosphere–ocean thermally coupled model: The role of the boundary layer processes, *J. Atmos. Sci.*, *68*(11), 2710–2730, doi:10.1175/JAS-D-11-078.1. 1.3

uib.no